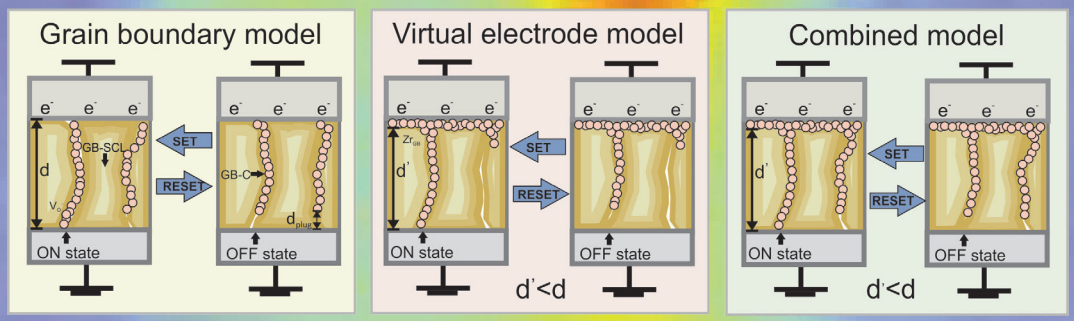

Resistive switching in ZrO_2 based metal-oxide-metal structures

Irina Kärkkänen

Member of the Helmholtz Association

JÜLICH
FORSCHUNGSZENTRUM

Schriften des Forschungszentrums Jülich
Reihe Information / Information Band / Volume 37

Forschungszentrum Jülich GmbH
Peter Grünberg Institute (PGI)
Elektronische Materialien (PGI-7)

Resistive switching in ZrO_2 based metal-oxide-metal structures

Irina Kärkkänen

Schriften des Forschungszentrums Jülich
Reihe Information / Information Band / Volume 37

ISSN 1866-1777 ISBN 978-3-89336-971-3

Bibliographic information published by the Deutsche Nationalbibliothek.
The Deutsche Nationalbibliothek lists this publication in the Deutsche Nationalbibliografie; detailed bibliographic data are available in the Internet at http://dnb.d-nb.de.

Publisher and Distributor: Forschungszentrum Jülich GmbH
Zentralbibliothek
52425 Jülich
Tel: +49 2461 61-5368
Fax: +49 2461 61-6103
Email: zb-publikation@fz-juelich.de
www.fz-juelich.de/zb

Cover Design: Grafische Medien, Forschungszentrum Jülich GmbH

Printer: Grafische Medien, Forschungszentrum Jülich GmbH

Schriften des Forschungszentrums Jülich
Reihe Information / Information, Band / Volume 37

D 82 (Diss., RWTH Aachen University, 2014)

ISSN 1866-1777
ISBN 978-3-89336-971-3

The complete volume is freely available on the Internet on the Jülicher Open Access Server (JUWEL) at www.fz-juelich.de/zb/juwel

Dedicated to my family

with love and deepest gratitude

Acknowledgments

I would like to express my deepest gratitude to many people without whom this work would not be possible.

I am deeply grateful to Prof. Rainer Waser who has given me the greatest opportunity to be a part of his institute for these three years. I thank him for the fruitful discussions throughout the work, for his invaluable comments and suggestions that have given me the opportunity to come up with important scientific results. Furthermore, I thank Prof. Georg Roth for agreeing to be a co-referent for my thesis.

I am eternally obliged to my supervisor Dr. Susanne Hoffmann-Eifert, whose patience, tolerance, encouragement, and resolute dedication have rescued me from peril more times than I can recall. I thank her for organization of this wonderful project I was involved in. I am greatly indebted to Dr. Andrey Shkabko, who always encouraged me in this work, for his fruitful critics and greatest involvement to the most of my research activities. I thank my colleagues in Research Center Jülich who always provided me with their help and support. I thank Stephan Masberg for his continous technical help in my research work as well his countenance and support in my learning of German language. I owe my thanks to Nabeel Aslam for fruitful discussions and help, and Marcel Reiners for his patience while giving me first knowledge in ALD. I thank Dr. Paul Meuffels, Dr. Vikas Rana, Dr. Uwe Breuer, Rene Borowski, Mirka Grates, Marcel Gerst and many other people supporting me throughout my work in Jülich.

I thank my colleagues in Helsinki University for giving me the opportunity to use their equipment and, what is most valuable, for sharing with me their knowledge in atomic layer deposition and films characterization. I am very greatfull for their continuous help and support. I thank Prof. Markku Leskelä, Prof. Mikko Ritala, Dr. Jaakko Niinistö, Mikko Heikkilä, Dr. Markku Vehkamäki. I would also like to thank my colleagues from Tartu University, Dr. Kaupo Kukli and Dr. Aile Tamm.

I thank my family for their love and support. My special thanks to Ilya who always motivated me, for his empathy and help.

Finally, I would like to thank Europenean Community's Seventh Framework Programme (FP7/2007-2013) under grant agreement ENHANCE-238409. Thank to ENHANCE project I have got, besides a very strong training in material science and technology, a lot of friends and scientific contacts that are invaluable for my future career.

Abstract

There is an increasing interest in resistive switching (RS) random-access memories (RRAM) for future electronics. A popular class of materials nowadays investigated for redox based resistive switches is transition metal oxides. A great challenge for the RRAM production is to develop a well-performing RS device compatible with a highly scalable CMOS technology. Among the group IV metal oxides, ZrO_2 is of interest for RRAM because of its chemical similarity to HfO_2 (exploited for high-k gate and RRAM applications) and because it is a fast ion conducting material. The goal of this work is a deeper understanding of the influence of the (i) metal-oxide-metal (MOM) layer stacks configuration, (ii) the oxide films microstructure, (iii) and their defect structure on the appearance of different switching modes, i.e. unipolar (UP) and bipolar (BP).

The thesis is based on the work which was supported by a European Marie Curie action and performed at the Research Center Jülich in collaboration with the Finnish ALD Center of Excellence in Helsinki. The first part deals with the fabrication of ZrO_2 thin films by an industrial compatible atomic layer deposition (ALD) process, the chemical, structural and morphological characterization of the films, the growth of ZrO_2/TiO_2 bilayers, the integration of the layers into metal-oxide-metal (MOM) devices and the electrical characterization with focus on the RS behavior. In the second part the effect of the device structure, in particular the thickness of the electrochemical active electrode (EAE) and the ZrO_2 film morphology, on the RS switching polarity of $Pt/ZrO_2/(EAE)$ cells is discussed.

ZrO_2 films and ZrO_2/TiO_2 bilayers were grown by ALD and were carefully structurally and electrically characterized. The variation of the ALD oxygen sources, O_3 or H_2O, influenced the morphology, structure, and at some extent the RS properties of the ZrO_2 films. The ZrO_2 films grown from $Zr[N(CH_3)C_2H_5]_4$ (TEMA-Zr) at 240 °C were polycrystalline with a mixture of cubic/tetragonal phases. ALD/H_2O-ZrO_2 films exhibited a random oriented polycrystalline structure, whereas the ALD/O_3-ZrO_2 films consisted of preferrably oriented cubic shaped grains. The ozone based ALD ZrO_2 process resulted in devices with a higher yield and reproducibility in contrast to water based one. $Pt/ZrO_2/Ti/Pt$ structures with a Ti top electrode (TE) thickness of 5 to 20 nm showed unipolar type RS behavior, while by increasing the Ti TE thickness a gradual change of switching polarity from unipolar to bipolar with a completely bipolar type RS behavior for a Ti TE thickness of 40 nm is found. The RS behavior of the ZrO_2/TiO_2 bilayer structures revealed a dependence on the stacking sequence of the layers. The switching in $Pt/ZrO_2/TiO_2/Ti/Pt$ devices was unipolar, comparable to $Pt/ZrO_2/Ti/Pt$ cells. In contrast, bilayers with the reverse structure, $Pt/TiO_2/ZrO_2/Ti/Pt$, showed non-switching behavior. The effect of the cells stack structure on the polarity of the RS behavior was studied in detail for 20 nm thick ZrO_2 films grown by an ozone based ALD process and integrated into $Pt/ZrO_2/Ti/Pt$ cells while the thickness of the electrochemically active electrode (Ti) was varied from 0 nm to 40 nm. Cells with a thin EAE (< 20 nm Ti)

exhibited a UP-type RS behavior, while cells with thick EAE (> 20 nm Ti) showed BP switching characteristics at a lower current compliance as the UP switching cells. A detailed structural analysis of the ozone grown ZrO_2 films revealed a polycrystalline structure of columnar shaped grains with a meta-stable cubic-tetragonal ZrO_2 phase. The phase stabilization was attributed to an incorporation of a certain amount (percentage regime) of process related impurities.

In the second part of the thesis an empirical model for the polarity dependence of the RS in the ALD ZrO_2 based devices as a function of the EAE thickness was suggested. The model assumed a columnar shaped microstructure and certain impurity content for the ZrO_2 films. In addition, the results of current-voltage behavior, temperature dependency of the resistance states and impedance spectroscopy (IS) measurements of different devices in different RS states were considered. Impedance spectroscopy measurements of UP and BP type switching devices with the same ZrO_2 films but with different EAE thicknesses were carried out for the states prior to electroforming (pristine), after RS into the ON-state and after RS into the OFF-state. The different devices in their pristine states exhibited nearly identical IS characteristics while the ON and OFF states of the UP and BP devices revealed pronounced differences. This result indicated that the effect of the EAE thickness on the switching polarity was primarily generated during the electroforming process. In the model, the UP switching in ZrO_2 based devices with thin EAE was described as a result of a non-complete local reduction of the grain boundary cores, which might gave rise to a hard thermal breakdown and the formation of metallic like conduction paths. On the contrary, the suggested idea for BP switching of ZrO_2 based devices with thick EAE based on the formation of local semiconducting oxygen depleted ZrO_{2-x} filament-like regions along certain positions, probably preferably at grain boundary cores. These filaments might be formed and ruptured by a thermal assisted oxygen vacancy drift. The combination of the structural analysis with measurements of the temperature dependences of the resistance states and the impedance spectroscopic characterization led to the idea of a micro-structural grain boundary model which could describe the difference in unipolar and bipolar type RS in $Pt/ZrO_{2-x}/(EAE)$ devices as a function of the thickness of the electrochemically active electrode. Furthermore, the proposed ‘grain boundary model’ was compared to the ‘virtual electrode model’. The careful comparison showed that both scenarios might explain the impedance spectroscopy results for the BP RS ZrO_2-based devices, while a combination of the two might be the most reasonable scenario in the description of BP switching in the studied ZrO_2 based devices.

Kurzfassung

Es gibt ein zunehmendes Interesse an resistiv schaltenden (RS) nicht-flüchtigen Datenspeichern (RRAM) für zukünftige Elektronikanwendungen. Eine für redox-basierte resistiv schaltende Speicherelemente intensiv untersuchte Materialklasse stellt die Gruppe der Übergangsmetalloxide dar. Die einzelnen Speicherzellen bestehen im Wesentlichen aus zwei metallisch leitenden Elektroden, die durch die funktionale Oxidschicht getrennt sind. Große Herausforderungen für die Fertigung hochintegrierter RRAM-Speicher bestehen darin, eine geeignete Architektur für den Aufbau der RS Elemente zu entwickeln und diese mit einem hoch skalierbaren Herstellungsverfahren, welches kompatibel zur Metall-Oxid-Halbleitertechnologie ist, zu kombinieren. Aus der Gruppe der IV-Metalloxyde ist ZrO_2 für die aktive Schicht in ReRAM von Interesse, weil das Material eine starke chemische Ähnlichkeit zu HfO_2 ausweist, welches schon in RRAM Zellen Anwendung findet, und weil es darüber hinaus als dotiertes Material als schneller Sauerstoffionenleiter bekannt ist. Das Ziel dieser Doktorarbeit ist es, ein tieferes Verständnis zu den Einflüssen (i) der Metall-Oxyd-Metall (MOM) Bauteilkonfiguration, (ii) der Mikrostruktur der Oxydschichten, und (iii) ihrer Defektstruktur auf das Auftreten der unterschiedlichen Schaltpolaritäten, einerseits unipolar (UP) und andererseits bipolar (BP), zu gewinnen.

Die Arbeit wurde im Rahmen eines von der Europäischen Union geförderten Marie-Curie Projektes ‚Enhance' am Forschungszentrum Jülich und am finnischen ALD-Exzellenzzentrum in Helsinki durchgeführt. Das erste Teil der Arbeiten umfasste die Herstellung von ZrO_2 Dünnschichten mittels industriell kompatibler Atomlagenabscheidung aus der Gasphase (ALD), die chemische, strukturelle und morphologische Charakterisierung der Filme, die Abscheidung von ZrO_2/TiO_2 Doppelschichten, sowie die Integration der Schichten in Metall-Oxyd-Metall (MOM) Strukturen und die elektrische Charakterisierung der MOM Bauteile mit Fokus auf den RS-Eigenschaften. Im zweiten Teil wurde der Effekt des Aufbaus von $Pt/ZrO_2/(EAE)$ Zellen, insbesondere die Einflüsse der Dicke der elektrochemisch aktiven Elektrode (EAE) und der Morphologie der ZrO_2 Schichten, auf die Polarität der RS – Schaltkurven untersucht und diskutiert.

ZrO_2 Filme und ZrO_2/TiO_2 Doppelschichten wurden mittels ALD gewachsen und sorgfältig im Hinblick auf ihre strukturellen und elektrischen Eigenschaften untersucht. Dabei zeigte die Variation der ALD Sauerstoffquelle, Ozon (O_3) oder Wasserdampf (H_2O), einen deutlichen Einfluss auf die Morphologien, Strukturen und mittelbar auf die RS Eigenschaften der ZrO_2 Filme. Die aus $Zr[N(CH_3)C_2H_5]_4$ (TEMA-Zr) bei 240 °C gewachsenen ZrO_2 Filme wiesen eine polykristalline Struktur mit einer Mischung aus kubischer und tetragonaler Phase auf. In den ALD/H_2O-ZrO_2 Filmen waren die Kristallite zufällig orientiert, während die ALD/O_3-ZrO_2 Schichten aus bevorzugt orientierten, kubisch geformten Körnern bestanden. Dabei wiesen die nach dem Ozon-basierten ALD Verfahren hergestellten ZrO_2 Schichten eine höhere Ausbeute und Reproduzierbarkeit von MOM Zellen aus als die mittels H_2O-basierter ALD hergestellten Filme. Für die weiteren Untersuchungen wurde daher der TEMA-Zr/O_3 Prozess

verwendet. Pt/ZrO_2/Ti/Pt Strukturen, mit einer Titanelektrode (EAE) der Dicke von 5 bis 20 nm, zeigten ein unipolares resistives Schaltverhalten. Die RS Verhalten der ZrO_2/TiO_2 Doppelschichtstrukturen zeigte eine Abhängigkeit von der Stapelfolge der Schichten. Für die Pt/ZrO_2/TiO_2/Ti/Pt Zellen wurde ein unipolares Schaltverhalten beobachtet, vergleichbar zu den Pt/ZrO_2/Ti/Pt Zellen. Im Gegensatz dazu zeigten Doppelschichten mit umgekehrter Struktur, Pt/TiO_2/ZrO_2/Ti/Pt, kein resistives Schalten.

Der Einfluss der Dicke der elektrochemisch aktiven Elektrode (EAE) auf die RS Polarität in Pt/ZrO_2/Ti/Pt Zellen wurde im Detail für 20 nm dicke ZrO_2 Filme untersucht. Die EAE-Dicke wurde von 0 nm bis 40 nm Titan variiert. Zellen mit einer dünnen EAE (< 20 nm Ti), zeigten ein unipolares (UP) RS Verhalten, während Zellen mit dickeren EAE (> 20 nm Ti) bipolare (BP) Schalteigenschaften zeigten, bei einem niedrigeren Begrenzungsstrom als die UP Schaltzellen. Transmissionselektronenmikroskopie an einem mit Ozon gewachsen ZrO_2 Film ziegte deutlich eine polykristalline Struktur mit säulenförmigen Körnern aus einer metastabilen kubisch/tetragonalen ZrO_2 Phase. Die Phasenstabilisierung wurde auf den Einbau einer geringen (%-Bereich) Menge verfahrensbedingter Verunreinigungen zurückgeführt. Detaillierte Untersuchungen zum Einfluss der EAE Dicke wurde an zwei Zellen mit identischer 14 nm dicker ZrO_2 Schicht und unterschiedlicher Topelektrode aus (5 nm Ti/30 nm Pt) einerseits und 30 nm TiN andererseits durchgeführt. Elektroformieren führte zu unipolarem Schalten im ersten und zu bipolarem Schalten im zweiten Fall.

Zusätzlich zu den Schaltkurven wurden die Temperaturabhängigkeiten der Ströme durch die Zellen im ON und in OFF Zustand bestimmt und es wurden Zellen beider Schaltpolaritäten im Ausgangszustand, im ON und im OFF Zustand mittels Impedanzspektroskopie charakterisiert. Dabei konnte gezeigt werden, dass die Zellen mit unterschiedlich dicken EAE im unformierten Zustand nahezu identische Impedanzcharakteristiken auswiesen, während sich nach dem Elektroformieren deutliche Unterschiede jeweils zwischen den ON und OFF Zuständen der unipolar- und bipolar- schaltenden Zellen ergaben. Dieses Ergebnis wurde derart interpretiert, dass der Effekt der EAE Dicke auf der Schaltpolarität hauptsächlich während des Elektroformierens erzeugt wurde. Auf Basis aller morphologischen, strukturellen und elektrischen Ergebnisse wurde ein empirisches Modell vorgeschlagen, welches die Ausbildung einer Schaltpolarität in den ALD ZrO_2 basierten RS Zellen in Abhängigkeit der Dicke der elektrochemisch aktiven Elektrode (EAE) beschreibt. Im Modell wird das UP Schalten der ZrO_2 Zellen mit dünnen EAE als Ergebnis einer möglicherweise unvollständigen lokalen Reduzierung des Materials an den Korngrenzen beschrieben. Dieses kann in Folge eines harten thermischen Durchbruchs zur Ausbildung von metallisch leitenden Strompfaden führen. Demgegenüber basiert die für das BP Schalten ZrO_2 basierter Zellen mit dicker EAE vorgeschlagene Idee auf der Bildung lokal halbleitender ZrO_{2-x} Strompfade, bevorzugt an den Korngrenzen oder alternativ entlang schwach isolierender Stellen im Film. Beim Schließen und Aufbrechen der leitfähigen Filamente spielt die thermisch unterstützte Drift von Sauerstoffleerstellen eine wichtige Rolle. Das vorgeschlagene "Korngrenzenmodell" beschreibt vollständig die experimentellen Beobachtungen. Als alternative Beschreibung für das Auftreten von unipolarem und bipolarem RS in Pt/ZrO_{2-x}/(EAE) Zellen mit unterschiedlicher Dicke der EAE wird darüber

hinaus das Modell der "virtuellen Elektrode" diskutiert. Der Vergleich zeigt, dass beide Modelle die experimentellen Beobachtungen, insbesondere die Ergebnisse der Impedanzspektroskopie für die BP RS ZrO_2 basierten Zellen, schlüssig erklären können. Da gleichzeitig jedes der Modelle die Schichtstruktur in einer komplementär stark vereinfachten Weise beschreibt ist für eine spätere Verfeinerung der Beschreibung auch eine Kombination beider Modelle denkbar.

Contents

Index of acronyms and symbols

$V_o^{\cdot\cdot}$ – oxygen vacancy

AFM – atomic force microscopy

ALD – atomic layer deposition

B – bulk

BE – bottom electrode

BP – bipolar

BPS – bipolar switching

CF – conducting filament

CMOS – complementary metal–oxide–semiconductor

CS– complementary switching

CVD – chemical vapor deposition

EAE – electrochemically active electrode

ECM – electrochemical mechanism

EF – electroforming

EOT – equivalent oxide thickness

GB – grain boundary

GB-C – grain boundary core

GBM – grain boundary model

GB-SCL – grain boundary space charge layer

GIXRD – grazing incident x-ray diffraction

GPC – growth per cycle

HRS – high resistance state

HT-GIXRD – high temperature grazing incident x-ray diffraction

HTP – high temperature (crystalline) phases

IS – impedance spectroscopy

LRS – low resistance state

MOM – metal-oxide-metal structure

OGF – ozone grown films

PEALD – plasma enhanced atomic layer deposition

PVD – physical vapor deposition

rf – radio frequency

RMS – root mean square

RRAM – resistive random access memory

RS – resistive switching

RT – room temperature

SEM – scanning electron microscopy

SIMS – secondary ion mass spectrometry

TCM – thermo-chemical mechanism

TCR – temperature coefficient of resistance

TD – temperature dependence

TE – top electrode

TMO - transition metal oxide

UP – unipolar

UPS – unipolar switching

VCM–valence change mechanism

VE – virtual electrode

VEM – virtual electrode model

WGF - water grown films

XPS – x-ray photoelectron spectroscopy

XRR – x-ray reflectivity

1. Introduction

Results of extensive research in the field of resistive switching (RS) materials indicate that the RS effect can revolutionize the non-volatile memory market [1]. Reversible changes of the resistance in metal-oxide-metal (MOM) structures, due to application of electrical stimuli, that is voltage or current, build a new memory concept, which might replace FLASH memory in the future. Basic requirements for scalability, endurance, low cost, low power consumption, and fast operation might be combined in one passive device. Many world-leading companies - like Samsung, Hynix, Toshiba, IBM, HP, and others – are involved in research of resistive random access memories (RRAM) [2-6]. In year 2013 Panasonic brought the first 8bit MN101LR series microcomputer with mounted RRAM on it.

The variety of the RS materials that were investigated and reported in the scientific literature is constantly growing. Most of these materials are binary and ternary metal oxides, like TiO_2 [7], HfO_2 [8], Ta_2O_5 [9], ZrO_2 [10], Nb_2O_5 [11], NiO [12], $SrTiO_3$ [13], Al_2O_3 [14], SiO_2 [15], etc, which are insulators in their stoichiometric form. The most easily producible materials that fulfill all the requirements mentioned above have the best prospects to be used for device fabrication in the industry.

However, good operation of the RS devices does not merely depend on the oxide materials themselves, but rather the structure of the whole metal-oxide-metal (MOM) device is of great importance; for example, the type of the used electrodes and their thickness play an important role for determination of the device operation. By choosing different electrode materials one can vary the switching mechanism in the devices, i.e., a valence change mechanism in case of inert electrodes (Pt, Au), or an electrochemical metallization effect in case of chemically soluble electrodes (Cu, Ag) [16]. By varying the

thickness of the electrodes, one can for example adjust the resistive switching modes, like unipolar (UP) or bipolar (BP) switching [17-21].

Taking into account the energy consumption, the UP switching (UPS) devices are unlikely to become a preferred candidate in mass production because the consumed power is significantly higher than in BP devices [23]. Regardless of the more complex integration scheme of the BP switching (BPS) cells, they are more interesting for future memory technology because in general the current levels are much lower compared to UP devices.

In addition to the selection of the MOM stack configuration, the oxide deposition method is a big issue, as the production costs have to be constantly minimized, while the output has to be kept at maximum. Most of the physical vapor deposition methods (PVD) are often very well exploited on to the laboratory scale but they are not entirely applicable for large scale production in the industry. On the contrary, chemical vapor deposition methods are more often utilized in the semiconductor industry. Among them, atomic layer deposition (ALD) is of great interest as it has many advantages due to its outstanding compatibility with the semiconductor industry production processes. The main positive qualities of ALD are: good conformal growth of the films on large area 2D and severe 3D structures, excellent control of the film thickness, good control of doping or substitution by other materials, and unique scalability.

The issues described above, i.e., the oxide deposition method, oxide material and electrode selection, are all very crucial for the fabrication of a well performing RS device. Consequently, the current tasks of RRAM researcher, is to understand and comprehensively describe the processes that take place in the materials during the switching process [in 54, Chapter 30, Fig. 7]. This can greatly contribute to the successful RRAM device fabrication and operation.

In this work I aimed to investigate the RS in atomic layer deposited ZrO_2 based MOM cells. The reasons to choose zirconia for this investigation were: (i) easy production using ALD, (ii) Zr closeness by the properties to the other IV^{th} group elements in the periodic table (Ti, Hf), which oxides (TiO_2 and HfO_2) are very well investigated for RS application, and (iii) the lack of comprehensive analysis of ZrO_2 RS properties. Additional trigger was (iv) a famous work of IBM group from Bednorz et al [24], who reported about RS in Cr-doped $SrZrO_3$. Zirconia is a chemically stable CMOS (complementary metal–oxide–semiconductor) devices

compatible material and in a form of yttria-stabilized-zirconia (YSZ) a fast oxygen ion conductor. The ALD processes for deposition of zirconia are well established for commercially available precursors. However, RS properties of ALD grown ZrO_2 based devices are still incompletely studied and a comprehensive description of the RS mechanism in case of UP and BP switching that can be found in this material [21, 25] still remains an open topic.

1.1 State-of-the-art

To the best of my knowledge, the first report on RS in $Zr/ZrO_2/Au$ structures was published in the year 1970 by Park and Basavaih from IBM [26]. The authors showed that 100-200 nm thick zirconia films switched unipolar with the resistance ratio up to 10^4. The SET current level was around 1 mA, and RESET around 6 mA. Using an optical microscope it was shown that after the switching craters appeared on the top electrode. Moreover, from the electron microscope analyses of the hollow regions the authors concluded that oxygen deficient regions around the spot were formed, and the switching was through conductive filaments that extended through the whole stack. The RESET was suggested to happen due to the high electric field, either peeling off the top electrode or destroying the filament itself.

RS in ZrO_2 was reintroduced by a report on the ZrO_2 based RRAM devices in the year 2005 [27]. In this study, the authors investigated RS of non-stoichiometric oxide prepared by rf-sputtering. A Pt/ZrOx/p –Si configuration was used for investigation of RS. The non-stoichiometric films had a monoclinic-tetragonal phase mixture as confirmed by XRD analyses. Authors claimed that the ZrO_x layer was split into three different layers of ZrO_2, starting from the device top: (i) stoichoimetric insulating layer, (ii) medium insulating layer, and (iii) highly conductive non-stoichiometric layer in the bottom. The proposed switching model was based on trapping/de-trapping electronic processes, involving positively charged zirconium ions in the medium layer.

In the paper of Lin et al. [28] differences in the RS behavior of $Pt/ZrO_2/(TE)$ cells with different top electrodes were firstly reported. The authors noted that Ti being in contact with zirconium oxide resulted the best RS behavior in comparison with Al and Pt. They reported good uniformity and stability of switching parameters in case of Ti electrode. The presented number of write/erase cycles was about 10^4. The authors proposed that Ti could

act as an oxygen gettering material, which leads to a redistribution of oxygen vacancies in zirconium oxide. The interesting fact is that using Pt or Al electrodes in Pt/ZrO_2/(TE) cells the UP switching was observed, while the Pt/ZrO_2/Ti structures were switching BP.

Wu et al. [29] studied Al/ZrO_2/Al structures, which exhibited a UPS behavior. The films were prepared by rf-sputtering, and were claimed to be stoichiometric according to x-ray photoelectron spectroscopy (XPS) results. However, both the oxygen XPS spectrum and the absolute concentration of oxygen in the films were not presented. It is also not clear whether the films were amorphous or crystalline that could also serve as an indication of the film purity. Authors claimed that in such "pure" films, which they obtained, there was no excess of Zr or O vacancies and the conducting filaments, responsible for the obtained UP switching, might form due to the penetration of Al into the films.

Starting from the year 2007 several studies reported significant improvement in the RS of ZrO_2 based RRAM by using Ti, either as an electrode or as a dopant. When the Pt/ZrO_2/Ti structures were used, the reported RS was in most cases BP [30-33]. The BP behavior was explained by the redox reactions occurring at the Ti/ZrO_2 interface, and by formation of oxygen vacancies containing filaments. On the contrary, the UP switching behavior was always found in the devices with Pt, Ni, Ag, W electrodes in combination with the second Pt electrode [28, 30-32].

Lin et al. [32] made an attempt to differentiate the UP and BP switching in Pt/ZrO_2/(TE: Al, Pt, Ti) devices. The authors suggested that after the high-voltage EF step different kinds of defects, such as $V_O^{\cdot\cdot}$, $Zr_i^{\cdot\cdot\cdot\cdot}$, e^-, $h^{\cdot}$, should be formed. Special attention was on $V_O^{\cdot\cdot}$, which were claimed to be responsible for conductive filaments' (CF) formation. The difference in the switching behavior was explained by the alternating location of the formation or rupture of the CF in zirconia films. In case of the UP switching devices with the Al or Pt as TE the CF were formed and ruptured stochastically at different places inside the film and therefore no stable switching could be obtained. In case of BP switching of the Pt/ZrO_2/Ti stack the CF formation/rupture was confined at the ZrO_2/Ti interface, due to the redox reactions taking place at this region, thus leading to the stable RS characteristics.

In another paper of Sun et al. [25] the coexistence of the UPS and BPS in Pt/ZrO_2/TiN devices was reported. The appearance of the UPS and BPS depended on the applied current compliance. At the I_{cc} starting from 1 mA up to 10 mA the BP switching was obtained. For I_{cc}

>10 mA the switching was UP. Unfortunately, the thickness of the TiN TE was not mentioned. First of all, authors made an assumption that TiN TE act as an oxygen reservoir, same as for the Ti TE. Second, due to the higher I_{cc} the injected oxygen vacancies were clustering and forming stronger filaments. These filaments were harder to set (bring to LRS), as a larger voltage was needed, and the hard-breakdown often destroyed the device. However, the model had a deficiency, i.e. it did not describe the system in a proper way in a sense of defect chemical properties of the material. The authors failed to describe what happens in the zirconium oxide if a cluster of $V_O^{\cdot\cdot}$ is formed, that is, whether there is a physical "cavity" forming along the CF or the system is reduced up to metallic Zr.

A paper reporting on the RS effects in the Pt/ZrO_2/Ti, where the thickness of the Ti TE was varied, was published in 2009 by Wang et al. [17]. It turned out that in the earlier proposed well-switching ZrO_2 based devices with the Ti electrode the switching characteristics were not always BP. At the thicknesses of Ti TE lower than approximately 30 nm the switching had a UP character, and it turned to BP only at higher Ti TE thicknesses. In addition to the switching polarity differences, also the EF voltage had a minimum at the transfer region from UP to BP. The authors explained this phenomenon by the formation of the TiO_x/ZrO_{2-x} layer which reduced the dielectric strength in the effective ZrO_2 layer with the increase of the Ti TE thickness. The BP switching was also explained by the formation of $V_O^{\cdot\cdot}$ filaments, due to the reduction of zirconia. However, the decent explanation of the appearance of UP switching was not given. In addition, similarly to the previously discussed papers, the rupture of the CF was always claimed to be at the TE, which is an electrochemically active one (EAE) and has a lower work function. It is nowadays a general consensus that the filament rupture happens at the Schottky type active electrode, which is, in case of this paper, a bottom Pt electrode [10].

Another approach for explaining the UP switching in Al/ZrO_2/Al devices was proposed by Zhou et al. [34]. They developed a trap/filament combined switching model. According to this notion, the CF are composed from filled traps on the grain boundaries (GB). The authors assume that after EF various defects gather along the GB, which act as traps for the electrons. Further, after application of the SET voltage all trap sites become filled by electrons bringing the system into the ON state. In the OFF state the electrons should be released from the traps by absorbing the thermal or optical energy. Nevertheless, the article

of Zhou et al., to the best of my knowledge, is the first one reporting the RS in ZrO_2 in the sense of reactions taking place on the grain boundaries, i.e. describing more realistic structure of the RS ZrO_2 based devices. Unfortunately, the authors failed to explain what kind of traps are working in the described way in the system as well as to bring any experimental evidence.

A recent publication reporting on stable UPS in 80 nm thick ZrO_2, sandwiched between Pt BE and 100 nm Ti TE, is from Zhang et. al. [35]. Similarly to the article from Sun et.al. [25], Zhang described the UP switching behavior as a formation of a strong oxygen vacancy containing CF. Despite the reasonable equivalent schemes proposed for the conduction in the devices in their ON and OFF states, the physical model of the clustered $V_O^{\cdot\cdot}$ in CF does not answer the reality, as in the previous case. The clustering of the oxygen vacancies in undefined places in the film (presented as a uniform media) does not seem to be a favorable process for chemically stable ZrO_2.

Only two recent studies report the RS properties of ALD grown ZrO_2. The first article about RS in TiN/(ALD) ZrO_2/Au devices was published by Salauen et al. [36]. In this study the 10-20 nm thick ZrO_2 films were grown at 250 ^oC using $(C_2H_5)Zr[N(CH_3)_2)]_3$ and oxygen plasma. The as-deposited 10 nm films were amorphous and started to crystallize in N_2 atmosphere from 400 °C, whereas the 20 nm films were already as-deposited crystalline with a cubic-tertagonal structure. The BP switching was obtained for all samples and no significant differences of the RS from the crystalline state were reported. The data on the endurance and retention of the ALD grown devices was not presented, whereas the rapid degradation of the device performance was mentioned.

Recent work from Kim et.al [37] reports on the RS in ALD grown ZrO_2 based Pt/ZrO_2/TiN stacks. Here, the authors showed the coexistence of the UP and BP switching in the devices depending on the voltage polarity during EF. Unfortunately, it was not clear from the text, with which polarity for EF resulted which mode was obtained. The authors succeeded to show the formation of the TiO_xN_y interface layer between zirconia and TiN electrode by TEM for a 650 °C annealed sample.

In addition to the RS in pure ZrO_2 based devices, some papers describe the switching in doped zirconia. For example, RS was obtained in the devices with embedded metallic nano-particles like for example Au [38, 39], Mo [40], Cu [41], Co [42] or Ag [43]. Guan et al. in [39]

reported on the BP RS of the doped zirconia system n^+ Si/ ZrO_2: Au/ TE, where "Au" are embedded gold nano-particles. It is interesting to notice, that in this article in the devices with pure ZrO_2 layer, which was as-deposited amorphous, practically no RS was observed. The proposed possible mechanism of RS is trapping and de-trapping of electrons on Au nano-particles, thus exhibiting a pure electronic character.

It is assumed that using combinations of two or more different oxide layers, the performance of the RS devices can be improved [44]. The RS in bilayers with zirconia was not extensively investigated. Lee et al. [45]presented the RS in ZrO_2/HfO_2 structures. The devices showed high resistance ratio, high switching speed, good endurance and retention up to 10^5 cycles at 85 °C. The devices were switching BP, and the RS mechanism was addressed to the redox reactions at the ZrO_{2-x}/HfO_{2-x} interface, where hafnia was playing a role of the oxygen reservoir.

Summarizing the literature review, the stable RS can be obtained in ZrO_2 based devices. Both switching polarities, UP and BP, were found depending on the device configuration and switching conditions. BP resistive switching in ZrO_2 based devices is very commonly explained by the redox reactions with the EAE, most often for the case of Ti or TiN. In some papers the coexistence of the UP and BP switching, which is dependent from the operational conditions, like compliance current or applied voltage, is reported. Nevertheless, the switching mechanism in zirconia still remains quite unclear and debatable as it was not sufficiently related to morphology and defect states of the ZrO_2 films.

1.2 Scope of this work

Two main objectives were pursued in this work. First of all, the fabrication of the ZrO_2 based devices with the optimal RS properties, where the ZrO_2 was grown by a well-established ALD process. Obviously, ALD is a very promising technique for deposition of the thin films with RS properties. One of the main advantages of ALD over PVD is a large scale production possibility under industrial conditions. ZrO_2 is a CMOS devices compatible material, as it is very chemically stable. Unlike HfO_2, the properties of which are very close to

zirconia, the latter is rather pushed aside in the RS application studies, especially the ALD grown one. Therefore, the first questions, which were addressed in this work, were:

(i) Is it possible to grow ZrO_2 by ALD which would give good RS properties when integrated into RRAM?

(ii) Would it be possible to affect the stoichiometry of the zirconia by modification of ALD process parameters?

(iii) What are the optimal ALD parameters for growing ZrO_2 films, showing the best switching properties when integrated into RS device?

In addition to the structural and electrical properties of the deposited films, the overall RS device configuration affects the RS behavior. Thus, the next question was formulated:

(iv) What would be the best RS device configuration, e.g. the thickness of the electrode material?

The second part of this work was devoted to a closer investigation of the RS properties of ZrO_2 based devices. In particular, I aimed to differentiate the two switching modes, unipolar and bipolar, which are obtained in the devices with either different electrode materials or electrode thickness. As it was revealed from the literature review in the previous section, the switching mechanism in zirconia still remains debatable, in particular the coexistence of the two switching modes, UP and BP. The existing ZrO_2 RS models are often very general and do not describe the realistic structure of the oxide. Hence, the following questions were to answer:

(v) What is the ALD grown ZrO_2 films' nanostructure?

(vi) How could the RS properties of the ALD grown ZrO_2 films be explained based on the realistic representation of the oxide films' nanostructure?

(vii) What is the switching mechanism of ZrO_2 based devices and how does this differ from the device configuration?

(viii) How can the UP and BP switching in the zirconia cells be differentiated?

In accordance to the above stated research questions the practical work was divided into four parts. The first part was the deposition of the zirconia thin films using ALD. The second part was the comprehensive structural analyses of the films using different spectroscopic and microscopic techniques. The third part concerned the investigation of the electrical and resistive switching properties of ZrO_2 based devices. Finally, the fourth part was devoted to the elaboration of the semi-empirical RS model, differentiating the UP and BP switching modes, consistent with the experimental results.

The manuscript is divided into eight chapters. In the following a short description of their content is given. In the second chapter the theoretical background of the principles of the resistive switching, like differentiation of the switching modes, electroforming effect, and widely accepted RS mechanisms are given. The aim of the second chapter is to present a general overview of the RS phenomena. In addition, concise information about the ZrO_2 physical and chemical properties is given.

In the third chapter the description of the experimental part of this work is presented. The ALD of the films as well as analytical techniques and the device fabrication are discussed.

The fourth chapter presents a detailed structural and morphological analyses of the ZrO_2 thin films. Techniques as grazing incident x-ray diffraction (GIXRD), x-ray photoelectron spectroscopy (XPS), and secondary ion mass spectrometry (SIMS) were used to characterize the films nano-structure. The atomic force microscopy (AFM), scanning electron microscopy (SEM), and transmission electron microscopy (TEM) were implemented to study the films' morphology. In addition, dielectric properties of the ZrO_2 films are discussed.

The fifth chapter focuses on the RS of the ZrO_2 based devices. The RS effect of the films grown with different metallic precursors, oxygen sources, and device configurations, is presented. Next, the temperature dependences of the resistances in the ON and OFF states of the Pt/ZrO_2/(EAE) devices are discussed. Finally, the RS in the Pt/ZrO_2/ TiO_2/(EAE) bilayers stacks is considered.

In the sixths chapter impedance spectroscopy (IS) measurements of the zirconia films are presented and discussed. The IS was done for pristine, ON, and OFF states of the corresponding Pt/ZrO_2/Ti/Pt (UP) and Pt/ZrO_2/TiN (BP) devices.

In the seventh chapter the semi-empirical switching model which describes the difference in UP and BP type RS in Pt/ZrO_2 /(EAE) devices as a function of the thickness of the electrochemically active electrode is proposed. The model is supported by the comparison with the experimental results.

The last, eighth, chapter presents the general conclusions, which are given in accordance to the raised research questions.

2. Fundamentals

2.1. Principles of resistive switching

The resistive switching (RS) is a phenomenon of the material (oxide) resistance change under applied electrical stimuli, like current or voltage, resulting in a hysteresis of the *I-V* curves. The simplest structure of the RS device is a MOM stack. The switching oxide material in the as-deposited state is in most cases an insulator. Before the RRAM cell can be switched in general an electroforming procedure has to be performed, which changes the cells' initial resistance. When the resistance of the RS device in the pristine state was sufficiently high after electroforming the cell is usually brought to the low resistance state (LRS), i.e. ON state. Although, there are cases, when the material is initially leaky and after electroforming switches to a high resistance state (HRS), which is also called an OFF state. Then after application of voltage/current the material is switched from the HRS to the low resistance state (LRS), which is also called an ON state. The transition from the HRS to the LRS is called SET, and from the LRS to the HRS – RESET. The resistance in the HRS is denoted as R_{off}, in the LRS as $R_{on.}$

The main feature of the RS devices, which allows using them in non-volatile memories is that once the cell has been switched to some resistance state, it remains in this state until a new stimulus will be applied. The switching process is reversible, i.e. the device can be switched between LRS and HRS a certain number of cycles before it breaks. To ensure a high efficiency of the working RRAM, the endurance of the device must reach up to 10^7 cycles or more, in order to become compatible with other memory types. In addition, the resistance values of the ON and OFF states (at 85 °C) have to be stable up to 10 years or more, to

guarantee a good retention of the device [16]. Further important parameter of RRAM is the R_{off}/ R_{on} or RS ratio. The R_{off}/ R_{on} is expected to be at least higher than 10 in order to be compatible with a FLASH memory. As conventional memory devices work at pulsing regime, the read V_{rd} and write V_{wr} voltages (read I_{rd} and write I_{wr} currents), as well as the pulse lengths have to fulfill certain requirements. For example, the V_{rd} has to be lower than V_{wr}, in order to retain the resistance state of the device. The read current I_{rd} cannot be smaller than approx. 1 μA, due to the optimal operational requirements of the electrical circuits. It is also preferable to hold the read and write (t_{rd} and t_{wr}) times in nanoseconds regime, as the shorter the read and write times are, the faster the device operation will be.

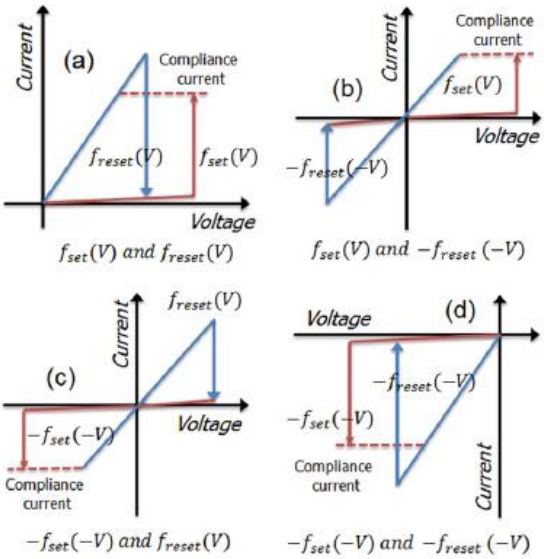

Figure 2.1: Possible combinations of SET and RESET I–V curves. For the UPS, all four combinations are observed, whereas for the BPS only (b) and (c) curves are possible. Copyright IOP Publishing LTD [46].

Two typical RS modes are distinguished in RRAM: UP and BP switching. In case of UPS the SET and RESET can occur at the same voltage polarity, whereas in BP mode the polarity should be always changed to switch the device from OFF to ON state and back. Figure 2.1 presents the typical *I-V* curves for UPS (a,d) and BPS (b,c) [46]. In case of the UPS the applied power to the device in the SET and RESET half-cycles is usually higher than in the BPS cells, which may cause a breakdown in the UPS films, and, therefore, has to be controlled by the

compliance current (I_{cc}). For the BPS cells the compliance current can be applied in the SET process, and for the RESET process the I_{cc} is usually not applied.

The BPS I-V characteristics are distinguished as either “counter-eigthwise” (Figure 2.1 (b)) or “eigthwise” (Figure 2.1 (c)) in relation to the cell layer stack. The origin of these two types of behaviors was explained in the paper of R. Münstermann et al. [47], where authors showed that the “counter-eigthwise” I-V curve of Fe-doped $SrTiO_3$ is a consequence of a filamentary switching, which is a formation of confined conductive filaments (CF) consisting of charged species, e.g. oxygen vacancies. Because the CF can be inhomogeneously distributed in the oxide, the filamentary switching had no dependence on the electrode pad size. On the contrary, the appearance of the “eigthwise” switching I-V curve is explained as a homogeneous metal/oxide interface switching that depends on the electrode pad area. Upon application of the negative voltage to the TE, the oxygen vacancies are pulled up accumulating at the oxide/TE interface. The lower part of the oxide film will be at some point completely depleted and the overall resistance increases (HRS). Then the reversed voltage ‘moves’ the vacancies back to the BE, by that restoring the LRS. When talking about “eitghwise” and “counter-eigthwise” I-V switching curves one should keep in mind the type of the grounded bottom electrode (BE). In the described case, the BE is a so called active one, which has a higher work function in comparison to the TE. Accordingly, the BE forms the Schottky barrier with the film, and the switching is assumed to happen near the BE.

Recently, another resistive switching type was described in the literature, which was called a complementary resistive switching (CRS). Originally, it was proposed for complex circuits to avoid sneak-path problems [48]. Later it was shown that this type of RS can be distinguished as a separate switching mode, which was explained as a “middle state” between BP and UP switching [49]. The difference between these modes is that in case of CRS the SET and RESET occur at the same polarity, and there is no need in current compliance for RESET process (Figure 2.2 (b)) [133].

In some cases a so-called abnormal switching was observed [50, 51]. In the unbiased state the cell is always in LRS. Applying the voltage of any polarity at its certain value the RESET occurs and the cell over-goes to HRS. Upon sweeping the voltage over zero, the cell returns to the LRS. This type of behavior is not comprehensively understood, and believed to

be connected with some type of interfaces. The abnormal RS cannot be used for a non-volatile memory, because the resistance state is volatile.

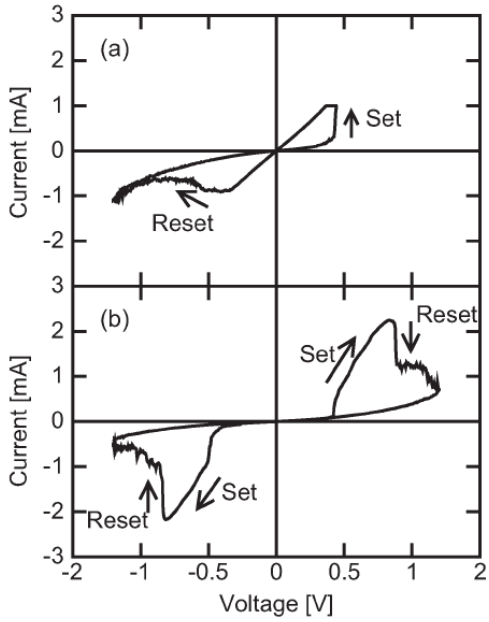

Figure 2.2: Measured I–V characteristics for (a) bipolar switching and (b) CS in a HfO_x-based RRAM device with an oxide thickness t_{ox} = 5 nm. In bipolar switching, the current during positive SET is limited by a current compliance (I_{CC} = 1 mA in the figure), and RESET is operated in the negative polarity. In CS, the current during set transition is not limited, and the positive-voltage sweep induces set followed by reset. The initial reset state with high resistance is recovered by a similar sweep under negative polarity [133], copyright IEEE Electron Devices Society.

In the RRAM concept, the low and high resistance states can be denoted as “1” and “0”, respectively, i.e. presenting a one bit storage cell. In some cases, a multilevel switching is possible, depending on the material and applied current compliance. Based on such multilevel switching, a high density, multi-bit storage can be implemented [52].

2.1.1 Electroforming

In order to switch a RS cell often a pretreatment procedure has to be conducted. This operation is called “electroforming” (EF) or “forming” [134]. A comprehensive overview about electroforming was written by Jeong et al. [46]. Initially, i.e. before EF, the RS cells are in the pristine state. In order to electroform the cell the electrical stress (current or voltage) has to be applied, which causes a change in the cells’ resistance. However, during electroforming the applied electric field can cause a dielectric breakdown, which would deteriorate the device. This risk can be eliminated by applying a proper current compliance I_{CC}. The electroformation of the cells is often characterized as a soft-breakdown process. Usually, in order to form the cell the EF voltages (V_{ef}), applied to the device, are higher, in comparison to the subsequent SET and RESET voltages (V_{set} and V_{reset}). Some systems are formed at the comparable V_{ef} and V_{set} or V_{reset} parameters. In this case the devices are called forming-free. Forming-free cells are very attractive for the RRAM production, as the absence of the initially induced soft-breakdown ensures a longer life-time of the corresponding cells.

Both types of EF are reported: forming to the ON state (to LRS) and forming to the OFF state (to HRS). Here, I concentrate on the description of the EF of the RS device to the LRS, in which the as-deposited oxide film is highly insulating, means that by inducing a soft-breakdown the conducting paths (CF) are presumably formed in the oxide. One of the explanations of the EF mechanism, described by Jeong [46], is the so called anodic reactions and ion or ionic defect migration. Upon electroforming oxygen vacancies might be created at the anode according to the following oxidation reaction:

$$O_O^x \rightarrow V_{\ddot{O}} + 2e^- + 1/2O_2(gas) \quad (2.1),$$

where $O_2(gas)$ is the oxygen gas, which might be either released to the atmosphere, forming craters/bubbles on the electrode, or, if the anode material is oxygen-reactive, cause the formation of a second metal phase at the interface between the oxide and the metallic anode. In this work I used stacks with electrochemically active electrodes (EAE) on top. The TE is called an electrochemically active electrode, due to its ability to participate in

electrochemical oxygen exchange reactions. For positive voltage applied to the TE the oxidation reaction (2.1) might take place on the EAE. Subsequently, the oxygen vacancies drift towards the cathode forming the CF. When the CF touches or almost touches the negatively biased BE, the system is formed to the ON state.

The possible scenario for the EF of the cell into the HRS is following. After the positive voltage is applied to the TE the vacancies are drifting towards the negatively charged BE or the cathode. If any oxygen ion transfer from the BE region to the $V_{\ddot{O}}$ enriched film is inhibited, when oxygen vacancies will accumulate near the cathode that will make this region *n*-conductive. Because of the increased electronic conductivity, the electric field becomes lower and the mobility of $V_{\ddot{O}}$ also decreases. The "piling up" of $V_{\ddot{O}}$ near the cathode leads to a forming of the $V_{\ddot{O}}$ rich virtual cathode and an insulating $V_{\ddot{O}}$ depleted region close to the anode. The more vacancies pile up in front of the cathode, the more the so called "virtual cathode" propagates towards the anode. When this "virtual cathode" has build-up and nearly touches the anode, this state has a stable character, and it is assumed that the cell is formed to the OFF state. Further, the "virtual cathode" comes to contact with the anode and the system is switched to the ON state [16].

Sometimes the investigated devices are very leaky in the pristine state, due to the fabrication process conditions or some other reasons. Hence, the forming has to be performed to the OFF state first. This is relevant, if the resistance state of the pristine state is not identical to the ON state. Otherwise, the device would be called a forming-free. The EF for the leaky device would practically mean that already existing conductive paths have to be ruptured or re-formed before subsequent RS. Specifically, for the EF to HRS the BE is biased positively, that will "push" oxygen vacancies towards the TE, and the conductive paths will be ruptured.

These explanations of the EF effect are quite general, and not always explicitly describe the ongoing processes in the certain materials. For example, in some oxides the electroforming occurs due to the change of the local oxygen-to-metal ratio under applied electric field. As a result, the sub-phases can built-up and propagate from one electrode to another, like in TiO_2, where the CF contain a Magneli phase (Ti_4O_7) [53]. Due to the different concentration of the free charge carriers in the different sub-phases the resistance around

the CF region changes. The phase transition requires a certain amount of the thermal energy, which is provided during electroforming.

The described EF mechanisms display the EF of the BPS cells. The EF of the UPS cells is more accurately explained by thermally activated processes. When the increasing current results in a drastic increase of the temperature in the film, the thermoelectric breakdown takes place. The high temperature facilitates redox reactions occurring at some weak places in the oxide, what in turn results in the formation of CF [54]. The SET and RESET voltages in the UPS devices are usually lower than the V_{ef}, as the CF are believed to be only locally ruptured in the consequent RS cycles, and not totally dissolved that would require more energy.

2.1.2 Switching mechanisms

The resistive switching mechanisms are still a matter of debates, as most of the time the experimental methods remain more or less indirect. However, some of the existing explanations are widely accepted by the researchers' community. There are several mechanisms that were explicitly classified by Waser et al. [16] shown in Figure 2.3. The most commonly discussed mechanisms in the literature are: electrochemical metallization (ECM), valence change mechanism (VCM), and thermochemical mechanism (TCM). The VCM and TCM are addressed to the RS in ZrO_2 based devices with Pt, Ti, and TiN electrodes, depending on the obtained switching mode.

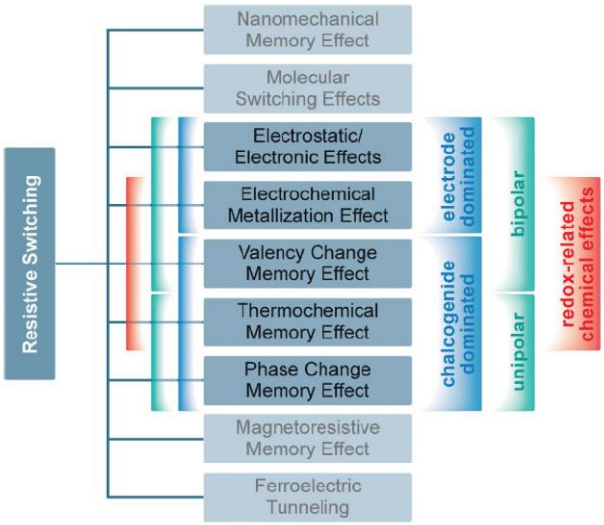

Figure 2.3: Classification of the resistive switching effects which are considered for non-volatile memory applications [16], Copyright © 2009, John Wiley and Sons.

Electrochemical Metallization Effect

The electrochemical metallization effect is explicitly described by I. Valov and co-workers in [55]. The ECM device is also sometimes called a programmable metallization cell, an atomic switch, or a conductive bridging RAM (CBRAM) [56]. The basic principle of the ECM is an electrochemical dissolution of a chemically active electrode (Cu or Ag) in a non-symmetric MOM cell. The counter electrode is usually inert (Pt, Ir). The oxide material serves as an electrolyte. Positively charged metal ions are released from the anode and dissolved in the electrolyte. The ions move towards the cathode, and after taking up the electron, a metallic filament of the anode metal is formed on the cathode proceeding towards the anode. When the CF is formed the cell switches to the ON state. By changing the polarity the metal ions are released from the filament and drift towards the negatively charged EAE and deposit on its surface. As a result, the filament is broken and the cell switches to the OFF state. For the operation of the ECM cell an electroforming step and a current compliance are needed.

Valence Change Memory Effect

VCM type RS is found in nearly all transition metal oxide based RRAM. The advantages of the VCM mechanism are: soft or sometimes no electroforming [57], very high endurance and retention time, fast read-write performance, etc. The switching mode of the RS devices, where VCM dominates, is bipolar. The oxygen vacancies in the transition metal oxides (TMO) play a central role in the VCM. It is assumed that in every insulating film at room temperature due to configurational entropy there is always some amount of non-stoichiometry present that leads to a certain initial oxygen vacancy concentration in the film. There are also other reasons for the presence of $V_{\ddot{O}}$ in TMO, e.g. impurities or doping. The concentration of oxygen vacancies affect the valence state of the adjacent transition metal cations that may result in a change of the electronic conductivity [16]. When the cations are reduced by the presence of $V_{\ddot{O}}$ (charge neutrality condition), the electronic conductivity is increased due to the increased population of the electrons in the *d*-band (conduction band) of the metal ions. When in the ON state the CF consisting of $V_{\ddot{O}}$ is formed, the conduction of the cell increases, due to the released electrons into the conduction band. Subsequently, by changing the polarity of the applied voltage, a part of the reduced metal ions re-oxidizes due to the change of the $V_{\ddot{O}}$ concentration, which are 'pulled' towards the negatively charged electrode. The re-oxidation of the TMO results in the decrease of the conductivity, which brings the cell into the OFF state.

Thermochemical Memory Effect

The TCM is frequently observed in transition metal oxides (TMO). The switching mode of the RS devices, where TCM dominates, is unipolar. Similar to the VCM, the TCM in TMO is also explained by the change of the valence state of the transition metal ions (cations), only that this change is temperature-induced. When no stable lower oxide phases exist for the TMO, e.g. NiO, the temperature-induced reduction of its cations results in a formation of the metallic CF. The corresponding linear *I-V* curves as well as metallic-type temperature dependences (TD) of the resistances in the ON state serve as an indicator of a metallic or

near-metallic conduction. The temperature coefficients of resistances (TCR), obtained from the resistance TD in the ON states, are usually lower than the TCR of the corresponding pure metals. This can be explained by the presence of defects and impurities in the metallically conductive phase. The RESET process is usually described by rupture of the CF due to the Joule heating of the cell under applied, sufficiently high, voltage (current).

2.2 Structural and electrical properties of ZrO_2

"Diamond simulant", zirconia, or zirconium dioxide is a popular precious stone used in jewelry. Zirconium dioxide is a high hardness, high tensile strength, and a corrosion resistant material. Never found in nature in pure form, it is extracted from zirconates (ZrO_2-SiO_2, $ZrSiO_4$) and baddelyites (ZrO_2) [58]. Both minerals contain a lot of impurities, which have to be chemically extracted. Baddelyite, for example, contains 96.5%-98.0% of pure zirconia.

Zirconia is a very important material for many various applications, as e.g. in fuel cells [59], dental treatment [58], or semiconductor industry. Zirconia is chemically inert and therefore is suitable for CMOS device technology. ZrO_2 is very thermodynamically stable material, as can be concluded from the Ellingham diagram [60]. This becomes obvious from the comparison of the differences in Gibbs free energy values G of the metal and the corresponding oxide. The Gibbs free energy gain upon oxidation of Zr into ZrO_2 is about 20% higher (ΔG= -1092 kJ·mol^{-1}), than e.g. for the Ti → TiO_2 oxidation process (ΔG= -852 kJ·mol^{-1}). In pure form, zirconium dioxide is an insulator. Several crystalline structures of ZrO_2 are observed, where the most common are monoclinic, cubic, and tetragonal phases. At high pressures it can be found in orthorhombic phase [61]. Zirconia in its pure form and at a normal pressure is monoclinic (*m*) up to 1170 °C, tetragonal (*t*) between 1170 °C and 2370 °C, cubic (*c*) between 2370 °C and 2706 °C, and molten above 2706 °C [62]. The three main polymorphs of zirconia are shown in Figure 2.4. The distribution of the crystalline phases in zirconia depending on pressure and temperature is schematically presented in Figure 2.5 [135].

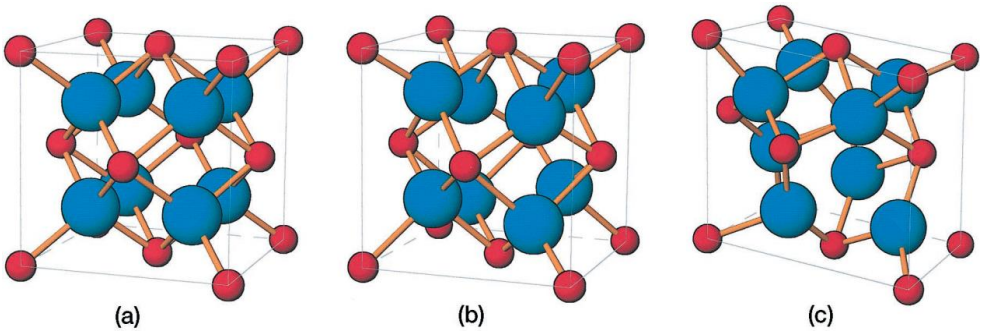

Figure 2.4: Three polymorphs of ZrO_2: a) cubic (*c*), b) tetragonal (*t*), and c) monoclinic (*m*) Copyright © 2004, John Wiley and Sons [66].

The electronic structure of ZrO_2 can be roughly described as a valence band consisting of the filled O 2p orbitals, and a conduction band with the empty Zr 4d orbitals [63]. The electrical properties of the ZrO_2 depend on the crystalline phase. The predicted band gaps for pure cubic, tetragonal, and monoclinic zirconia are 5.55, 6.40, and 5.42 eV, respectively [62]. The dielectric properties of ZrO_2 also vary with the crystalline phase. Dielectric constants for monoclinic, cubic, and tetragonal phases are 19.7, 36.8, and 46.6, respectively [64, 65].

One of the properties of ZrO_2, as a polymorphic material, is the phase transformation at elevated temperatures [58, 67]. This phenomenon is the reason not to use pure zirconia in many applications. Severe microstructural damages are induced in the ZrO_2 as a consequence of a crystals' volume change during heating or cooling. Due to the different lattice constants of the corresponding crystalline phases, e.g. in case of the $t \rightarrow m$ phase transition, the volume of the crystal changes up to 3-5%, which results in cracks and flaws in the material. The special treatment of ZrO_2, called crystalline phase stabilization, is used to overcome a non-plastic deformation of the crystalline phases during cooling processes [68]. The most common stabilization agent is yttrium oxide. Yttria (Y_2O_3) stabilized zirconia (YSZ) has a cubic structure, which is stable at the whole range of temperatures, including room temperature (RT). Zirconia can be also stabilized by doping with MgO, CaO, or Ce_2O_3. When the stable cubic phase is obtained at RT, zirconia is called fully-stabilized. The tetragonal phase of the doped ZrO_2 or a mixture of the *t-c* phases is regarded as a partial stabilization.

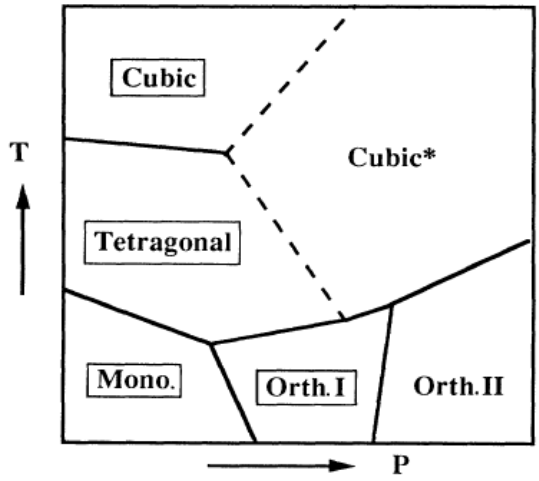

Figure 2.5: Schematic pressure P – temperature T diagram for pure ZrO2. The atmospheric pressure can be taken at the beginning of the P-axis [135]. Copyright © 1993 by the American Physical Society.

The temperatures for the phase transformation of the pure ZrO_2 are rather high (1170 °C – 2370 °C). However, by increasing the number of impurities, it is possible to shift the phase transformation near the RT [69]. The high temperature phases (HTP) (*c, t*) are often found in nano-crystalline films, deposited at relatively low temperatures [70-72]. This type of HTP crystallization is called a meta-stable one.

On the one hand, the meta-stable phase is usually an indicator of impurity containing films, that is a partial stabilization [67] or full-stabilization effect, e.g. YSZ [73]. The meta-stable cubic phase at RT in nitrogen doped zirconia was reported e.g. by Wang et al [74]. With increasing the temperature the *t* - phase evolved starting from 500 °C, as a result of the *c-t* phase transition. Starting from the 850 °C the nitrogen was totally removed from the films, and the stable monoclinic phase was formed.

On the other hand, it was shown that low temperature stabilization of the tetragonal phase can also appear in impurity-free ZrO_2 [75, 76]. As it was reported by Shukla and Seal in [77], in nano-crystalline zirconia powder with the grain size ≤ 10 nm the stabilization of the high temperature *t*- phase was observed at RT. The grain size of 10 nm was determined as a critical size for the phase stabilization. When the grains were smaller than the critical size, the large surface area of the grains and excess of energy caused the meta-stable phase

crystallization. When the grains were bigger than the critical size, ZrO_2 crystallized to the stable monoclinic phase.

Namavar et al. [78] presented the stabilization of the cubic phase in the zirconia thin films without any dopants. The explanations for this phenomenon were given as either due to the grain size effect, similar to the case of the tetragonal meta-stable phase crystallization, or due to the usage of ion-beam assisted deposition method that provided the films with a certain amount of oxygen vacancies which served as stabilizer. Tsuchiya et al. [79] reported the *c-t* transformation, which happened in 'pure' zirconia, at 400 °C. However, the authors did not present any impurity verification that might be connected to the usage of e-beam evaporation process.

The main ionic defects in zirconia, proposed in the literature, are oxygen interstitials, oxygen vacancies, and oxygen-zirconium defect complexes $(V_{Zr}V_O)^{\cdot\cdot}$ [80]. As the formation of oxygen interstitials is geometrically unlikely process, oxygen vacancies are considered to be the most dominant donor-type ionic defects. The oxygen vacancies can be either formed due to the exchange reactions in reducing atmosphere at high temperatures, or their concentration can be significantly increased by stabilization of ZrO_2 using aliovalent cations, such as e.g. divalent (Mg^{2+}) or trivalent (Y^{3+}) [63].

The ionic defects are inhomogeneously distributed in the polycrystalline zirconia, which consists of grains interconnected through grain boundaries (GB) [81]. In the acceptor doped ZrO_2 (like e.g. YSZ), a high concentration of oxygen vacancies ($V_{\ddot{O}}$) is mostly found on the grain boundary cores (GB-C), forming there positively charged regions. The positive charge is electrically compensated by the formation of a negatively charged space charge layer (SCL), adjacent to the GB-C. The SCL consists of the segregated aliovalent dopants or acceptor-like impurities. Physically, the SCL belongs to the bulk, but electrically it is a part of an "electrical GB configuration" which is a GB-C and two adjacent SCL. The GB-C surrounding SCL is in practice a double Schottky barrier, which limits the current flow through the material. Zirconia is a mixed ionic-electronic conductor. In a bulk material, due to the double Schottky barrier, the ionic conductivity through the grains is typically higher than across the GB. The situation is changed in nano-crystalline films, where due to the decrease of the grain size, the Schottky barrier height decreases, resulting in an increase of the concentration of $V_{\ddot{O}}$ in

a SCL [82]. This gives an increase of the overall GB ionic conductivity, whereas the bulk conductivity still remains higher. In respect to the RS devices, the higher ionic conductivity of the grains and the lower of the GB can be observed only in the pristine state at high temperatures, where the overall resistance of the film is still highly insulating for the resistive switching. The electrical conductivity of the crystalline zirconia thin films with a columnar structure is found to be higher across the grain boundaries in the transport direction [82, 83].

3. Experimental

3.1 Atomic layer deposition

Finding an appropriate method for oxide growth is one of the challenges for future RRAM production. The important tasks in resistive switching application are achieving an efficient downscaling of the devices as well as the ability to grow conformal films over large areas with three dimensional structures. ALD is a promising technique that fulfills the above mentioned requirements. One of the biggest advantages of ALD is that it is already industrially utilized and is suitable for large scale fabrication of thin films in a controllable way [84]. In addition, conventional ALD can be used for coating three dimensional structures [85] and area-selective ALD for deposition of lateral nano-patterns [86]. Its compatibility to semiconductor device processing and its flexibility makes this technique attractive for the deposition of resistive switching films with optimized morphological and structural properties, which enable stable resistive switching operation.

ALD is a chemical vapor deposition method, where minimum two reacting precursors are required for deposition of thin films [87]. Commonly, for binary metal oxides one metal reactant and one oxygen source are used. Water, ozone, or oxygen plasma are the most utilized oxygen sources, where the first two reactants are used for a thermal ALD and the oxygen plasma is utilized in plasma enhanced ALD (PEALD). The metal containing precursors are discussed in the next section.

The main principle of ALD is a chemisorption of the precursor molecules on the reaction sites on the surface. In order to avoid reactions between the precursors in the gas phase, the precursors are isolated from each other in the way that they are sequentially injected into

the chamber (Figure 3.1). After each precursor injection pulse the ALD reactor is purged by the inert gas, argon or nitrogen, in order to clean the reactor from any residuals and byproducts. The first introduced precursor chemisorbs on the surface until a saturation condition is reached, i.e. all available chemisorptions sites are filled. The residuals of the first precursor are purged away by the carrier gas and the second precursor is introduced. Further, an excess material and byproducts are again purged to the exhaust. The process shown in Figure 3.1 (a-d) is repeated a certain number of cycles. As the ALD is a self-limiting process, i.e. under the saturation conditions the growth is limited to below one mono-layer, the films can be deposited in a very controllable manner.

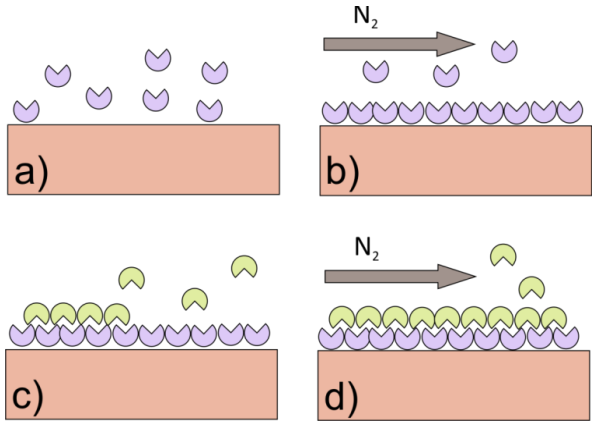

Figure 3.1: Schematic of the four ALD steps: a) injection of the first precursor; b) saturation and purge; c) injection of the second precursor; d) saturation and purge.

3.1.1. Precursors

Two main classes of metal reactants are distinguished for the deposition of metal oxide films: inorganic and metal-organic [87]. The main requirements for all precursors are their high volatility, high vapor pressure, and absence of any decomposition at the deposition temperatures. In this work only the metal-organic precursors were used, as they are less toxic than the inorganic ones, e.g. halides, and leave lesser impurities in the films.

The precursors, which were mainly used in this work for deposition of ZrO_2 and TiO_2, are tetrakis-(ethylmethylamido) zirconium (TEMA-Zr) $Zr[N(CH_3)C_2H_5]_4$ and titanium isopropoxide

(TTIP) $Ti[OCH(CH3)_2]_4$, respectively (Figure 3.2 (a, c)). Ozone and water were utilized as the oxygen sources. In addition to the TEMA-Zr precursor, also the new compound bis-(ethylmethylamido)-bis-(*N*,*N*-diisopropyl-2-ethylmethylamidoguanidinato)-zirconium(IV) [guan = guanidinate, $(PrN)_2CN(CH_2)_5$] $(EtMeN)_2Zr(guan\text{-}NEtMe_2)_2$ or shortly guan-Zr, synthesized at the Ruhr-University Bochum in the Department of Inorganic Chemistry, was tested in combination with ozone (Figure 3.2 (b)) [88].

TEMA-Zr is one of the most frequently used metal-organic precursors for ALD of ZrO_2 [37, 64, 89-90]. TEMA-Zr belongs to the group of the alkyl amides precursors, i.e. it contains a direct metal-nitrogen bond [91], due to which the lower carbon contamination of the film during deposition is expected, in comparison to the other metal-organic precursors [90]. In addition, TEMA-Zr has a high reactivity and vapor pressure as well as non-corrosive byproducts. The ALD growth window of TEMA-Zr depends slightly on the used oxygen source [90, 92], and in general the deposition temperatures are between 200 °C and 300 °C. At higher temperatures TEMA-Zr decomposes, resulting in a poor uniformity [90]. A very important feature of TEMA-Zr is a high reactivity to oxygen and water. Handling of this precursor requires a usage of a glovebox.

The growth rate (GPC = growth per cycle) of the alkyl amides increases at deposition temperatures below and above the ALD window. This behavior has been attributed to an increase of the OH-group concentration on the surface (deposition temperatures below the ALD window) and thermal decomposition (deposition temperatures above the ALD window), respectively [93]. The similar GPC behavior was found in this study for ZrO_2 films grown on Si/SiO_2 substrates (Figure 3.3). ZrO_2 thin films grown from TEMA-Zr had the lowest growth rate at moderate temperature (@ 240 °C) for the two used oxygen sources: ozone and water. Therefore, in this work the deposition at 240 °C was considered as the most suitable for further fabrication of RS devices. As one can see from Figure 3.3, the growth rate of ZrO_2 films grown with water vapor was slightly lower (0.7 Å/cycle @ 240 °C) as compared to ozone (0.87 Å/cycle @ 240 °C). This may be explained by the lower reactivity of water, in comparison to ozone.

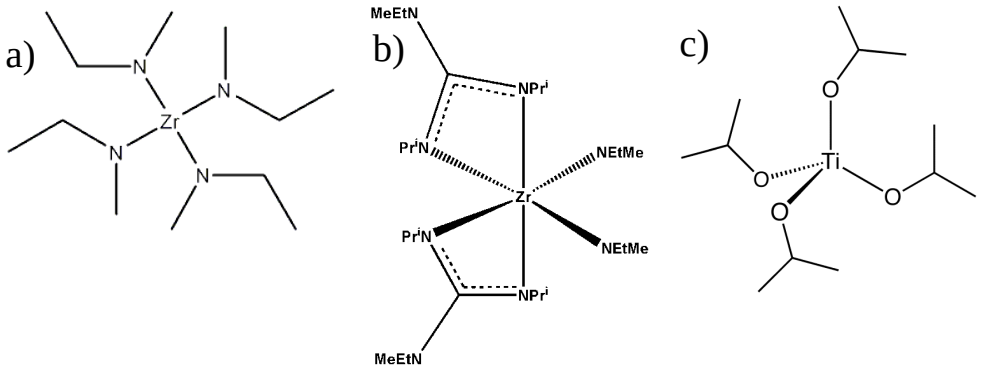

Figure 3.2: Precursors used in this work for the deposition of ZrO_2: a) TEMA-Zr; b) guan-Zr, and for the deposition of TiO_2: c) TTIP.

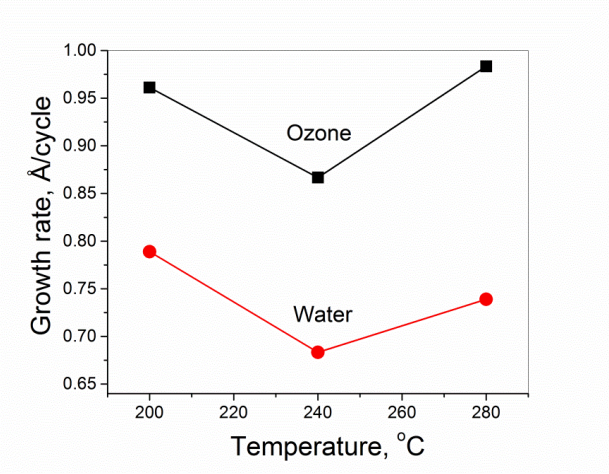

Figure 3.3: Dependence of the growth rate on the deposition temperature of the ZrO_2 thin films, grown with TEMA-Zr and ozone (black), or water (red).

Another reason for choosing TEMA-Zr precursor for this investigation was that its ALD window overlaps with the ALD window of the TTIP precursor [94], chosen for the TiO_2 growth. This is important for the growth of the ZrO_2/TiO_2 bilayers. TTIP is a low-cost and a commonly used precursor for deposition of TiO_2 films [95]. The GPC obtained for the TiO_2, grown at 240 °C on Si/SiO_2 substrates, was 0.02 nm/cycle.

The ZrO_2 films grown from guan-Zr precursor at 300 °C had a GPC approx. 0.08 nm/cycle. A comprehensive description of the guan-Zr ALD process, as well as the saturation curves are given in the work of Blanquart et al. [88].

3.1.2. ALD setup and experimental procedure in University of Helsinki

ZrO_2 and ZrO_2/TiO_2 bilayers were deposited by means of thermal ALD using water or ozone as oxygen sources. All films were grown in a hot-wall horizontal flow-type ALD reactor (F-120 by ASM Microchemistry Ltd, Figure 3.4) at a pressure of about 7±3 mbar. The nitrogen N_2 (> 99.999%), generated from air by a Nitrox UHPN 3000 N2-generator, was used as a carrier and purging gas. Ozone was generated from O_2 (99.999%) by a Wedeco ozomatic modular HC Lab-generator. The flow concentration of O_3 was estimated to be ca 100 g/cm^3.

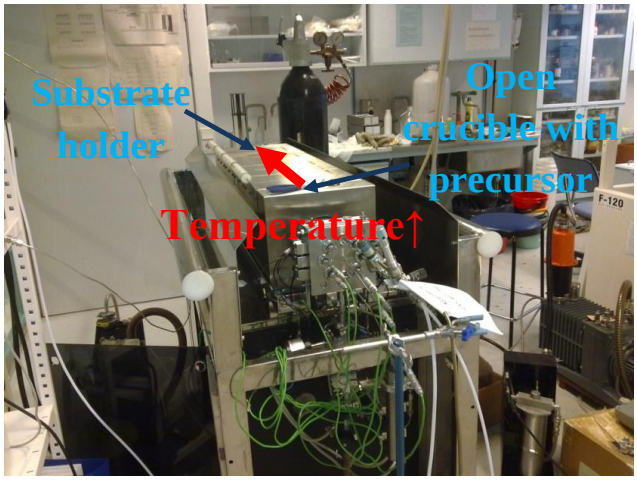

Figure 3.4. All films were grown using the ASM microchemistry hot-wall ALD reactor (F-120) in the University of Helsinki, Finland.

The operation of the hot-wall ASM ALD reactor is based on a gradient heating of the reactor walls, starting from lower temperatures for vaporization of the precursor from an open crucible, ending with the desired deposition temperature at the substrate holder (Figure 3.4). The holder allows to fix vertically two 5 x 5 cm^2 substrates with a gap of 2 mm in

between. The films were deposited on Si/ SiO_2 (500 nm) (Si/SiO_2) and for the planar structures (Section 3.5) on Si/ SiO_2 (500 nm)/ TiO_2 (10 nm)/ Pt (100 nm) (Si/Pt) substrates. The 5 x 5 cm^2 substrates were divided into 2 pieces of 2.5 x 5 cm^2 each and mounted onto the one side on the substrate holder. On the other side of the holder, in some deposition runs, the cross-bar structures were placed using a special mask-holder. The Si/ SiO_2 (500 nm)/ TiO_2 (5 nm)/ Pt (30 nm) (Si/Pt) substrates which were used for the cross-bar microstructures, are presented in Section 3.5. The Si/SiO_2 substrates were used for basic characterization of the films using AFM and XRR analyses. The Si/Pt substrates were used for SEM, TEM, XPS, GIXRD, and electrical characterization.

The substrates were pre-cleaned ultrasonically in isopropanol and blown dry with nitrogen. The deposition temperatures for TEMA-Zr varied between 200 °C – 280 °C, and the used deposition temperature for TTIP was 240 °C, for guan-Zr a temperature of 300 °C was chosen.

The precursors, $Zr(NEtMe)_4$ (TEMA-Zr, Sigma-Aldrich) and $Ti(O^iPr)_4$ (TTIP, Sigma-Aldrich), were evaporated from open crucibles kept inside the reactor at 62 °C and 40 °C, respectively. The evaporation temperature of guanidinate was 100 °C. Water vapor or ozone were used as the oxygen sources. The pulsing sequence (metal source – purge – oxygen source – purge) for ZrO_2 and TiO_2 samples was 1-2-1-2 sec.

3.2 Structural characterization

3.2.1 X-ray diffraction and high temperature X-ray diffraction (GIXRD, HT-GIXRD)

Structural properties of the thin films were analyzed by grazing incident X-ray diffraction (GIXRD) on a PANalytical X'Pert Pro MPD diffractometer with parallel beam optics and constant incident angle of 1°. The HT-GIXRD measurements were done in an Anton-Paar HTK1200N oven in air. The sample was heated up to 865 °C and cooled back, with the measurement intervals of 30 °C.

3.2.2 X-ray reflectivity (XRR)

The XRR scans were carried out on a Bruker D8 Advance diffractometer. The thicknesses of the films grown on Si/SiO_2 substrates were determined by fitting of the XRR scans using Leptos 7 software from Bruker. The values are given with a standard error of ± 0.5 nm.

3.2.3 X-ray photoelectron spectroscopy (XPS)

The XPS analysis was performed using a PHI5000 Versa Probe. The data were quantified using PHI MultiPak 9.3 and measured from the sample depth after moderate (30 sec) Ar+-sputtering (0.25 kV). The electron pass energy of 23.5 eV and take off angle of 80° were used. All peaks were normalized to the standard C 1s peak at 284.6 eV.

3.2.4 Secondary ion mass spectroscopy (SIMS)

The SIMS measurements were performed on a commercial time-of flight mass spectrometer ToF-SIMS IV from IONTOF GmbH, Münster, Germany. The instrument was equipped with a pulsed primary Bi cluster (Bi_n^+) ion source running at 25 keV. Cs^+ ions were used for sputtering at 1 keV.

3.3 Morphological characterization

The morphological analyses were performed by means of atomic force microscopy (AFM, SIS Ultra Objective) and scanning electron microscopy (SEM, Hitachi SU8000). The TEM cross-section sample was prepared using a FEI Quanta 3D 200i FIB-SEM instrument, and the 200 kV FEI Tecnai F20 Field Emission Gun TEM.

3.4 Electrical characterization

3.4.1 Measurements of dielectric properties

Capacitance measurements at RT were performed using a Hewlett Packard 4284A Precision LCR Meter applying 10 kHz signals with an amplitude of 100 mV. Effective dielectric constants were calculated assuming a parallel plate capacitor model as an average from at least 10 devices.

3.4.2 Resistive switching measurements

Resistive switching characterization was carried out with a programmed Keithley 2611 System Source Meter. A two-probe configuration was used for *I-V* measurements. The voltage was applied to the top electrode, while the bottom electrode was grounded.

3.4.3 Impedance spectroscopy

The impedance spectroscopy (IS) measurements were performed using Solartron SI1260 impedance analyzer in combination with a preamplifier. The scanning frequency was varied from 1 MHz to 1 Hz. The measurements were conducted at room temperature under a shielded cover. A two-probe configuration, as for the I-V measurements, was used for the IS studies with the active signal applied to the top electrode, while the bottom electrode was grounded. The switching of the cells, which were used for obtaining IS spectra, was done separately using the source meter.

3.5 Device fabrication

Figure 3.5 presents two typical device structures, which were used for the study of the oxide films RS properties. The left sketch (Figure 3.5 (a)) presents the planar device with the larger pad sizes (Ø 100-200 µm), in comparison to the micro-cross-bar devices where the cell sizes were from 1 μm^2 to $16 \cdot 10^4$ μm^2 (Figure 3.5 (b)). For the clarity also the top-view SEM micrographs of the planar and cross-bar device structures are shown in Figure 3.6.

For the fabrication of the Pt/ZrO_2/Ti/Pt planar structures the films grown from TEMA-Zr on the Si/Pt substrates were used. The top electrodes of 0, 5, 20, 40, 90 nm Ti and respectively 100, 30, 30, 10, 10 nm Pt on top, were deposited through a shadow mask by means of electron beam evaporation. Pt bottom electrodes were opened by etching of the oxide on the edge of the sample, using reactive ion beam etching (RIBE 300, Oxford Instruments).

The planar structures were also used for the fabrication of ZrO_2/TiO_2 bilayer devices. Bilayer structures of Pt/ZrO_2/TiO_2/(EAE) and Pt/TiO_2/ZrO_2/(EAE) with top electrodes of 5 nm Ti/ 30 nm Pt or 40 nm Ti/ 10 nm Pt were prepared.

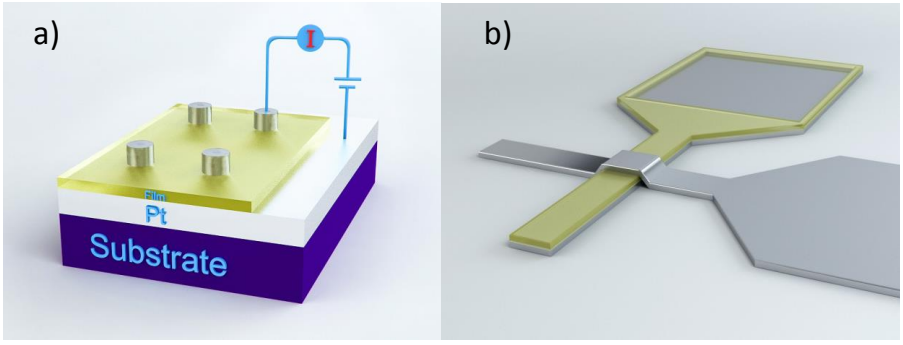

Figure 3.5: Sketches of the RS device structures, used in this work: a) the planar structure of the MOM device, the diameter of the top electrode pads was 100 and 200 µm, the "film" denotes the oxide layer under investigation [21]; b) the cross-bar cell, the cell sizes varied from 1 μm^2 to $16 \cdot 10^4$ μm^2.

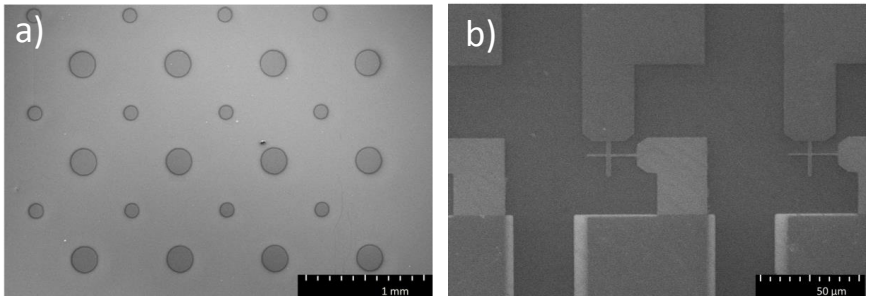

Figure 3.6: The SEM micrographs of a) the planar device structure and b) the cross-bar structure of RS cells.

The cross-bar Pt/ZrO_2/Ti/Pt and Pt/ZrO_2/TiN microstructures were fabricated on the Si/Pt substrates. The bottom electrodes were patterned and structured by conventional photolithography and reactive ion beam etching, respectively. The ALD ZrO_2 films were deposited onto the structured substrates. After ALD of ZrO_2 films, either Ti (5nm)/ Pt (30nm) or TiN (30-40 nm) layers were deposited by sputtering and patterned by conventional photolithography and structured by lift-off process. For electrical contacts the bottom electrode pads were opened using photolithography and reactive ion beam etching.

4. Structural and morphological characterization of the thin films

The knowledge about the films nanostructure, defect concentration, stoichiometry, etc., is of fundamental importance for building a realistic model of the RS device, which can be further used for the understanding of the RS mechanism. In this section the GIXRD data obtained from the ZrO_2 films and ZrO_2/TiO_2 bilayers are presented. The XPS analyses provide the information about the impurity concentration in the most investigated films in this work, grown from TEMA-Zr and O_3. The SIMS analyses enable to compare the oxides stoichiometry, grown using different oxygen sources. Next, the morphological studies by AFM, SEM, and TEM serve as an inherent support for the structural analyses. In addition, dielectric properties of the films are discussed.

4.1. Structural properties

4.1.1 Film structure analyzed by GIXRD and HT-GIXRD

Systematic structural investigations of ZrO_2 films were carried out by means of GIXRD analysis and rocking curve measurements. The crystallinity of the as-deposited ZrO_2 films on the Si/SiO_2 substrates was first controlled by GIXRD analyses. The GIXRD spectra of the films of the thickness series (TEMA-Zr/O_3 or H_2O, grown at 240 °C) is shown in Figure 4.1. The thinnest ZrO_2 films (11-16 nm) grown with ozone on the Si/SiO_2 were amorphous, whereas the water grown ones showed a mixture of cubic and tetragonal phases. The 18 nm ALD/O_3-

ZrO_2 films exhibited a mixture of cubic/tetragonal phases. The thicker water grown films were randomly oriented, similar to the case of the films on the Si/Pt substrates. The increased background on the left side of the plot is addressed to the influence of the Si/SiO_2 substrate.

The GIXRD analyses of the ZrO_2 films grown from guan-Zr with ozone or water on Si/SiO_x substrates, where the SiO_x is the natural oxide, were reported by Blanquart et al. in [101]. The deposition temperatures were between 250 °C and 300 °C. The as-deposited films grown from both oxidants exhibited crystalline cubic structure. The HT-GIXRD measurements showed that the cubic phase was stable up to the highest temperature examined (865 °C).

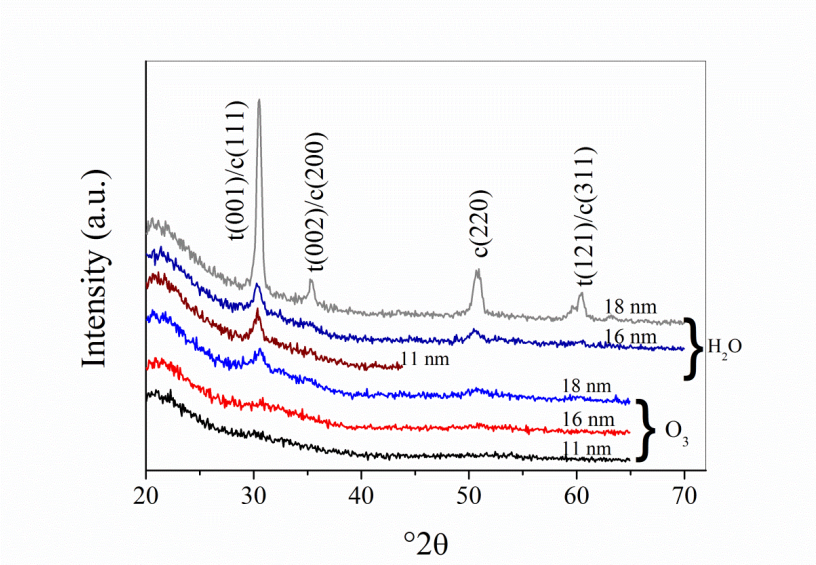

Figure 4.1: The GIXRD scans of the thickness series of ZrO_2 thin films grown at 240 °C on Si/SiO_2 substrates using the ALD TEMA-Zr process with water or ozone as oxygen source. Reference peak positions for cubic and tetragonal ZrO_2 referring to ICDD ref № (27-997) [97] and ICDD ref № (66-783) [98], respectively, are given.

Figure 4.2 (a) presents GIXRD scans of ZrO_2 thin films with different thicknesses that were grown on Pt electrodes at 240 °C using the ALD TEMA-Zr process with water or ozone

as the oxygen source. All ZrO_2 films consisted of a mixture of cubic and tetragonal phases, while no reflections of the monoclinic phase were detected.

Comparable results were reported by Kim and Hwang [70] for ALD ZrO_2 films grown on TiN from TEMA-Zr and O_3. On the contrary, Lamperti [96] found a mixture of cubic and tetragonal phases in ZrO_2 films grown on Si substrate from $(MeCp)_2ZeMe(OMe)$ and ozone, whereas for the use of water as oxygen source also the monoclinic ZrO_2 phase was detected.

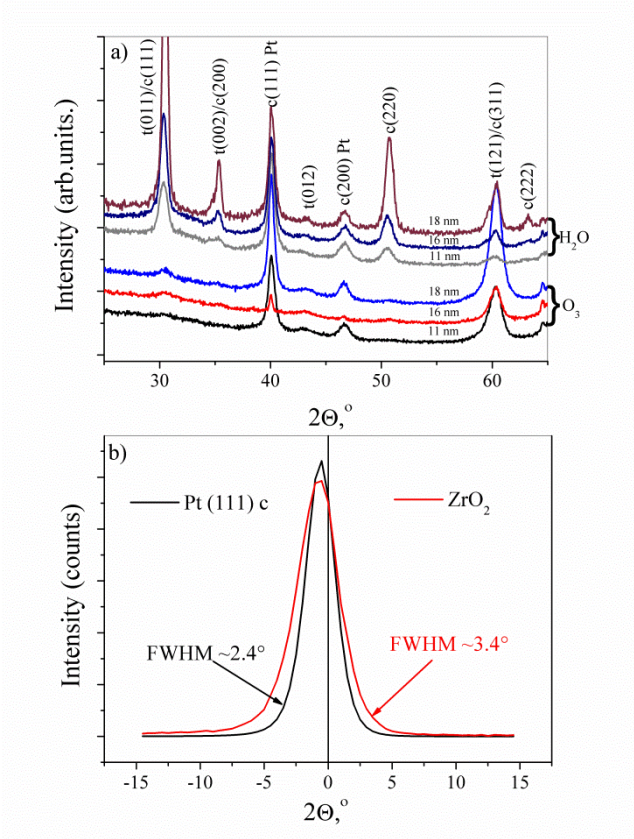

Figure 4.2: (a) GIXRD scans of the thickness series of ZrO_2 thin films grown at 240 °C on Si/Pt substrates using the ALD TEMA-Zr process with water or ozone as oxygen sources. Reference peak positions for cubic and tetragonal ZrO_2 referring to ICDD ref № (27-997) [97] and ICDD ref № (66-783) [98] are given, respectively. (b) Rocking curves performed at 39.8° 2Θ for the (111) textured Pt layer of the Si/Pt substrate and at 30.7° 2Θ for the ZrO_2 film grown on Si/Pt with the ALD TEMA-Zr/O_3 process. The "c" stays for the cubic phase of ZrO_2, and "t" for tetragonal phase [21].

In general, the GIXRD results for the films grown on the Si/Pt and Si/SiO_2 from TEMA-Zr are comparable, except that the crystallization of the films on Pt substrates is higher than on the SiO_2, where the thinner films are practically amorphous.

For the TEMA-Zr ALD process a clear difference in texture between the ZrO_2 films grown on Si/Pt (111) depending on the applied oxygen source were observed. The ALD/H_2O-ZrO_2 films exhibited a randomly oriented polycrystalline structure, whereas the ALD/O_3-ZrO_2 films showed a preferred orientation. Interesting to notice, that, especially for the thickest (18 nm) ALD/H_2O-ZrO_2 sample, double peaks at the 2Θ positions around 34° and 60° were detected. This finding provided further evidence for the presence of the tetragonal phase, however it did not rule out the presence of the cubic one. Further, the GIXRD scans of the ALD/O_3-ZrO_2 films, grown on Si/Pt substrates, show one dominant reflection around 60.2°. This indicates a strong preferential orientation of the grains parallel to the substrate normal direction.

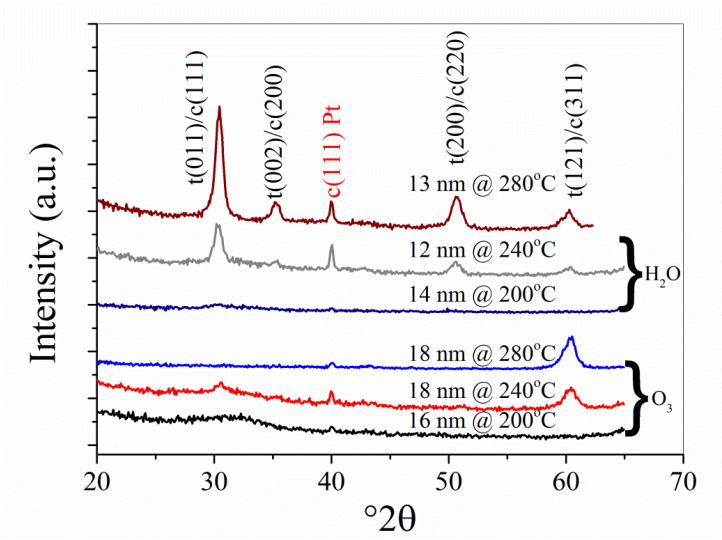

Figure 4.3. GIXRD scans of the ZrO_2 thin films grown at 200 °C, 240 °C, 280 °C on Si/Pt substrates using the ALD TEMA-Zr process with water or ozone as oxygen source. Reference peak positions for cubic and tetragonal ZrO_2 referring to ICDD ref № (27-997) [97] and ICDD ref № (66-783) [98], respectively, are given.

For verification, two additional rocking curves were measured separately for the Pt (111) reflection of the bare Si/Pt substrate at 2Θ of 39.8°, and for the 30.7° reflection of the 16 nm ALD/O_3-ZrO_2 film. From the results depicted in Figure 4.2 (b) the full width half maxima (FWHM) values of about 2.4° and 3.4° were calculated for the Pt (111) and the corresponding ZrO_2 peaks, respectively. The quite similar shift of both rocking curves from the surface normal (ω = 0°) indicates that the ZrO_2 grains grow preferentially over the Pt grains of the Si/Pt substrate. However, as the lattice constants of cubic (111) and tetragonal (011) phases are so close to each other, the distinguishing of these two ZrO_2 phases based on the rocking curve is impossible.

Figure 4.3 presents the GIXRD data of the of ZrO_2 thin films grown at different temperatures (200-280 °C) on Si/Pt substrates using the ALD TEMA-Zr process with water or ozone as the oxygen source. The films grown at 200 °C exhibited an amorphous structure, while the films grown with ozone or water at 280 °C showed similar crystallization behavior as for the films grown at 240 °C (Figure 4.2 (a)), but with slightly higher degree of crystallization.

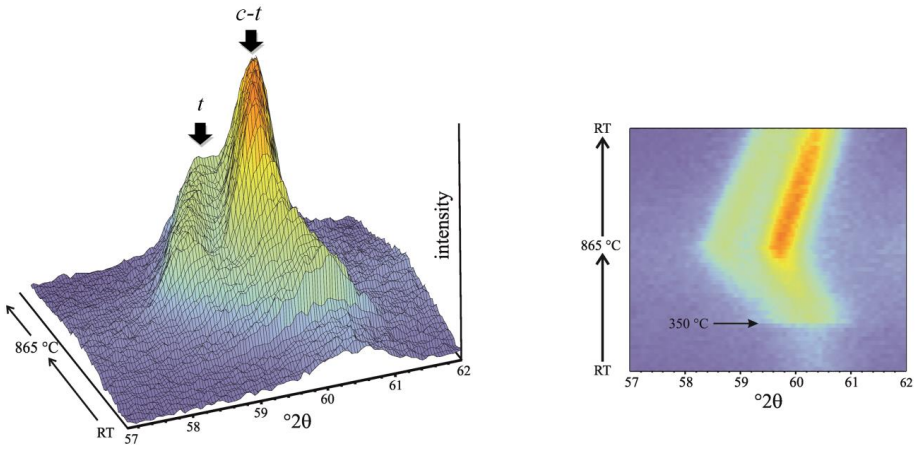

Figure 4.4: HT-GIXRD pattern of a 14 nm ZrO_2 film on a Si/Pt substrate. Double peak of tetragonal phase is clearly observed during cooling and the peaks end positions match closely to the reference values for the tetragonal ZrO_2 [98]. The separation of the doublet reflections suggests an asymmetric thermal expansion common to tetragonal ZrO_2.

For closer investigation of the ZrO_2 film crystallization, a HT-GIXRD measurement of the 14 nm, TEMA-Zr/O_3 film grown at 240 °C was performed (Figure 4.4). The sample was heated up to 865 °C and cooled back to RT. The poorly crystalline as-deposited film crystallized abruptly at 350 °C and continued to further crystallize up to 865 °C and even during the cooling process. Considering the double peak, shown in Figure 4.4, one cannot totally exclude the presence of the cubic phase in the sample, as the tetragonal peak at 2θ = 60.198°overlaps with the cubic reflection at 60.123°. However, the asymmetric shape of the reflection is in favor of the tetragonal phase. The tetragonal doublet (59.28° and 60.19°) is clearly observed above 700 °C. The separation of the doublet reflections suggests an asymmetric thermal expansion common to tetragonal ZrO_2 [99]. The fact that the positions of the reflections at the same temperatures during heating and cooling do not match, might be interpreted in a way that there is either stress or strain in the tetragonal phase right after the crystallization or there could even be a transformation from cubic to tetragonal phase. For comparison of the sample's crystallization degree before and after annealing, the full range GIXRD scans of the ZrO_2 sample in the as-deposited and annealed state are presented in Figure 4.5.

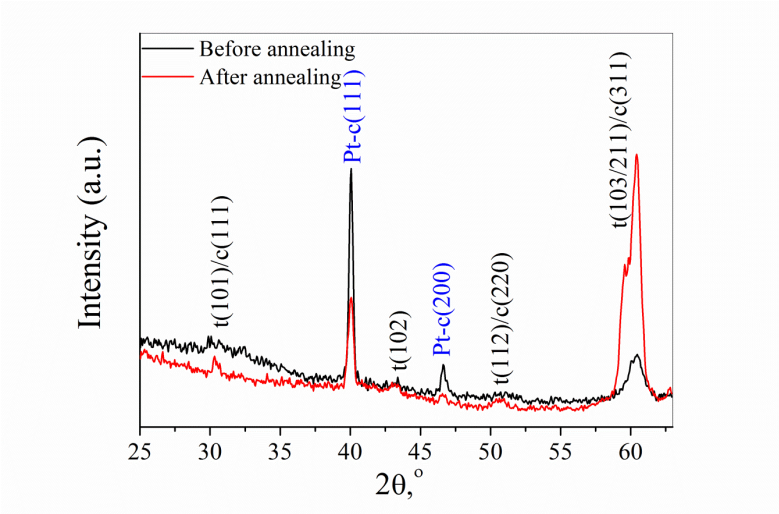

Figure 4.5: GIXRD data taken from the 14 nm ZrO_2 film on Pt substrate at room temperature before and after annealing up to 865 °C. The crystallographic data are taken from ICSD ref. № 53998 [100], № 66787 [98]. The "c" stays for the cubic phase of ZrO_2, and "t" for tetragonal one.

The investigated crystallization behavior of ZrO_2 polycrystalline films can be interesting for the discussion of the RS properties. During EF or switching the local temperature around the conductive filament in the film is increasing and the polycrystalline zirconia might undergo a local phase transformation. This could result in some minor structural changes as well as a creation of some additional channels for conduction or switching. Although these changes in the nanostructure would be extremely small and difficult to identify, the presence of the metastable c-t phase at RT shows that the realistic structure of the films cannot be ignored in the elaboration of the RS models. Specifically, the common presentation in the literature of the RS device with the ZrO_2 film layer depicted as a homogeneous medium with randomly distributed oxygen vacancies is not explicit [25, 35].

4.1.2 ZrO_2/TiO_2 bilayers on Si/Pt substrates

The GIXRD patterns of the different ZrO_2/TiO_2 bilayer structures are compiled in Figure 4.6. All bilayers were grown at 240 °C on the Pt electrodes from either the ozone or water based TEMA-Zr and TTIP-Ti ALD processes. The sequence and thickness of the respective TiO_2 and ZrO_2 layers were varied while keeping the total thickness of the oxide layer at about 16 to 18 nm. All reflections observed in the GIXRD scans can be identified as either anatase phase of TiO_2 or cubic/tetragonal phase of ZrO_2. Bilayers grown from the ALD/O_3 processes (black lines) showed more preferential orientation as compared to the films deposited with the ALD/H_2O processes (red lines). In addition, the bilayers presented some interesting differences with respect to the crystallization behavior. The ALD/O_3-ZrO_2 films which were grown directly on the (111) Pt electrode showed a preferred orientation of the grains (consistent to the observations for the single ZrO_2 films, see Figure 4.2 (a)). In contrast, the ALD/O_3-ZrO_2 films which were grown on a previously deposited TiO_2 layer, exhibited an amorphous structure when they were 4 nm in thickness and a randomly oriented polycrystalline structure when they were 13 nm thick.

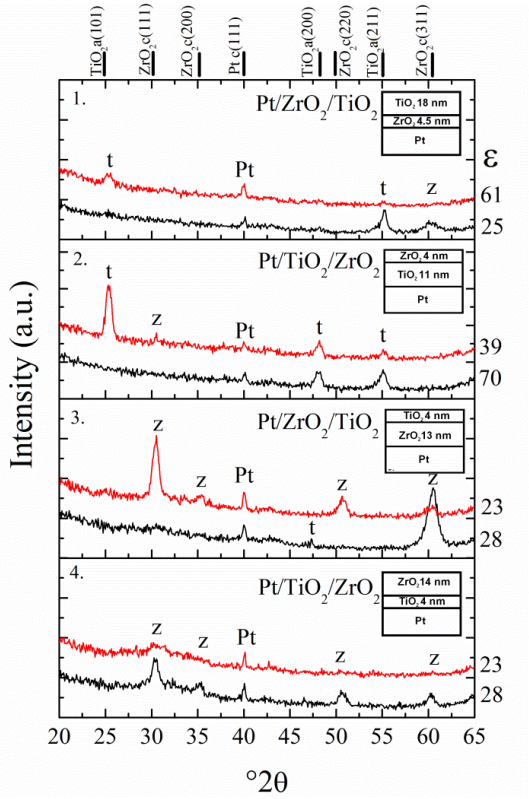

Figure 4.6: The GIXRD scans of ZrO_2/TiO_2 bilayer structures 1 to 4, where z = ZrO_2, t = TiO_2. The red curves represent the water processed films while the black lines belong to the ozone processed layers. On the right hand side of the graphs effective permittivity values (ε) of the Pt/bilayer/Pt capacitors are presented [21].

The ALD/H_2O-ZrO_2 films showed only very weak reflections independent of the underlying layer. No reflection could be addressed to the TiO_2 films with thickness below 5 nm. In contrast, 15 nm thick TiO_2 films deposited with ozone exhibited a randomly oriented anatase structure when grown on Pt (111) and a preferred orientation when grown on a textured ZrO_2 layer. The TiO_2 layers deposited with water showed a randomly oriented polycrystalline anatase-type structure independent of the underlying layer. The crystallization behaviour and the appearance of a certain texture in the bilayer structures therefore depended on: (i) the sequence in which the ALD TiO_2 and ZrO_2 films were deposited on the Si/Pt substrate, (ii) the thickness of the respective layers, and (iii) the oxygen source applied in the ALD processes.

4.1.3 Films thickness by XRR

For determination of the films thickness the XRR technique was used. The measurements were carried out on the films grown on the Si/SiO_2 substrates, because these substrates are much smoother than the Si/Pt ones, and by using the Si/SiO_2 the substrate roughness effects appearing on the spectra could be eliminated. The characteristic XRR spectra and the fitting curves of the ~16 nm ZrO_2 films grown from TEMA-Zr with ozone and water are presented in Figure 4.7. The standard density of zirconium dioxide used for the fitting was 5.68 g/cm^3.

The XRR spectra of the ozone grown bilayer structures are shown in Figure 4.8. The standard density of titanium dioxide used for the fitting was 4.23 g/cm^3. The thickness and roughness fitting values are given in Table 4-1.

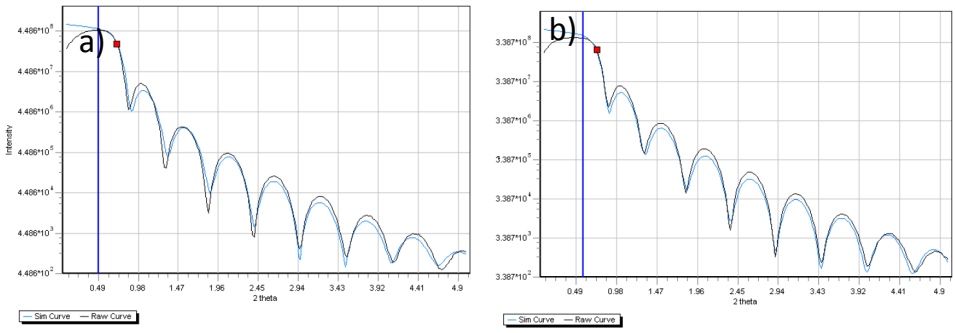

Figure 4.7: The XRR spectra of a) 15.35 nm thick O_3, and b) 15.63 nm thick H_2O grown ZrO_2 films on Si/SiO_2.

Sample	Thickness, nm		Roughness, nm	
	ZrO_2	TiO_2	ZrO_2	TiO_2
a	4.65 (±0.33)	17.97 (±0.43)	0.36(±0.31)	1.64 (±0.30)
b	4.33 (±0.10)	11.39 (±0.09)	0.58 (±0.10)	0.47(0.2)
c	13.24 (±0.11)	3.93 (± 0.12)	0.36 (0.29)	0.38 (±0.13)
d	14.07 (±0.19)	4.20 (±0.12)	0.55 (± 0.13)	0.42 (±0.19)

Table 4-1. The fitted XRR parameters for different ZrO_2/TiO_2 bilayers. The bilayer structures are depicted in Figure 4.8.

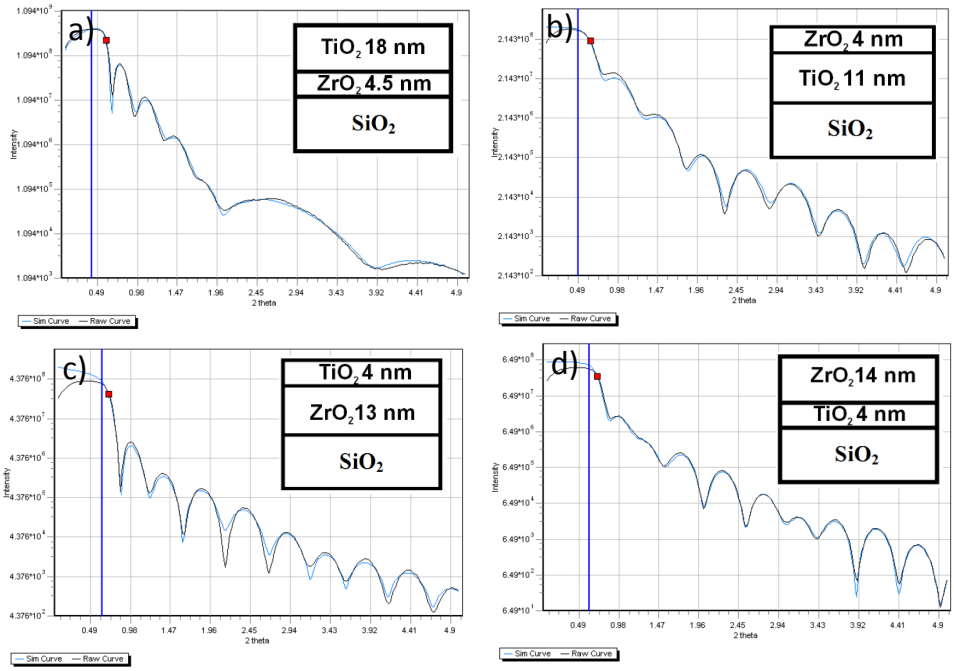

Figure 4.8: The XRR spectra of ZrO_2/TiO_2 bilayers grown from TEMA-Zr/TTIP/O_3 on Si/SiO_2 substrate. The respective structures are presented in the insets; the exact numbers for the thicknesses are given in Table 4-1.

4.1.4 Impurity analyses by means of XPS

The amount of ALD process related (residual) impurities in the ZrO_2 (TEMA-Zr/O_2, @ 240 °C) films was analyzed using XPS. Considering the choice of the ALD precursor ($Zr(NEtMe)_4$), any residues which might remain in the film should give rise to carbon or nitrogen related impurities. Figure 4.9 presents the XPS spectra taken from the film depth after moderate sputtering. The XPS results indicate that the zirconia films exhibit the O/Zr ratio close to 2 (1.91) indicating a nearly stoichiometric composition. The ZrO_2 phase is further confirmed by the shape of the detailed Zr 3d doublet shown in Figure 4.9 (b). The $3d_{5/2}$ and $3d_{3/2}$ peaks at 181.7 eV and 184.08 eV, respectively, can be identified with the nearly stoichiometric ZrO_2 phase, while additional peaks from a non-stoichiometric phase were not detected [102]. This observation is in good agreement with the chemistry of the

ALD process where ozone was used as the oxygen source. The mean impurity contents with respect to the amounts of the residual C- and N- rich impurities are listed in Table 4-2. The concentration of carbon was about 3.7 % and nitrogen 0.5 %. The detailed spectra of the O 1s, C 1s, and N 1s signals given in the Figure 4.9 (a), (c), and (d), respectively, show the appearance of doublet peaks, which are further discussed. The main O 1s peak at 529.58 eV originates from stoichiometric ZrO_2 [103]. However, a second peak at 530.81 eV, marked as O_1 in Figure 4.9, can be interpreted ambiguously. The C 1s spectrum (Figure 4.9 (c)) exhibits two peaks: one at 284.6 eV, which is the reference peak attributed to physisorbed carbon at the surface, and an additional peak at 288.63 eV, marked as C_1, which is related to carbonyl groups C=O [104]. The appearance of the O_1 can partially be explained by the presence of the residual C=O groups in the films. Baniecki et al. [105] demonstrated for $SrTiO_3$ that its exposure to CO_2 induces the shift of the O_1 peak to +1.9 eV, away from the oxide related oxygen O 1s peak, while the C_1 from C 1s spectra appears at 288 eV. The total energy difference between O_1 and C_1 is $\Delta E_b(O_1 - C_1) = 242.1 \pm 0.2\ eV$, where E_b is the binding energy. From the XPS of the ZrO_2 films, performed in this work, we obtained $\Delta E_b(\mathrm{O_1} - \mathrm{C_1}) = 242.18\ \mathrm{eV}$. From the calculated concentration values of the different species, listed in Table 4-2, it is evident that the amount of carbonyl residual groups is lower than 1 % (C_1), which means that the O_1 signal contains not only the oxygen in the carbonyl groups, as the O_1 signal is 5.81% higher than of the C_1 signal. Hence, the 5.81% should be addressed to some other oxygen containing species. It is known from the literature that the O_1 peak can be also related to OH groups [103, 106]. These groups are generally regarded as surface ones, but the XPS data presented in Figure 4.9 were obtained from the inner area of the films after sputtering. Consequently, one can assume that approximately 5-6 % of hydroxy-ions present in the as-deposited ALD ZrO_2 film.

The N 1s spectrum shown in Figure 4.9 (d) contains two components, one peak at 401.8 eV related to a covalent $\mathrm{N_2}$, and an additional peak at 398.83 eV which can be attributed to nitrogen ionic species, as for example $\mathrm{N_2^{2-}}$ with a binding energy of 398.5 eV [107]. As the measurement was done from the film's depth, one has to consider the possibility of residual ionic nitrogen species in the films, which might segregate at the grain boundaries [81].

It is worth to mention, that survey scans (not presented here) did not show any traces of other impurities. From the XPS analyses of the ozone grown zirconia film it can be concluded that the meta-stable cubic-tetragonal phase is probably addressed to the incorporation of a reasonable amount of ALD process related impurities, mainly hydroxyl-groups.

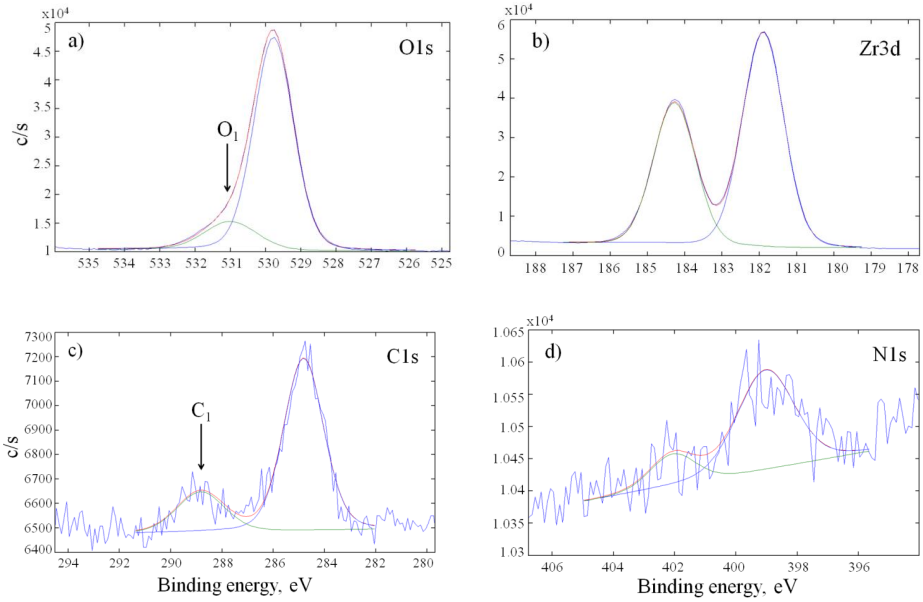

Figure 4.9: XPS spectra of TEMA-Zr/O_3 ZrO_2 film, grown at 240 °C on Si/Pt, (a) O 1s, (b) Zr 3d, (c) C 1s, (d) N 1s.

Element	Absolute concentration, %	Peak position, eV	Corresponding to:	References
Zr 3d	30.7	181.7	Zr $3d^{5/2}$	[103]
Zr 3d		184.08	Zr $3d^{3/2}$	[103]
O 1s	58.5	529.58	Oxide oxygen	[103]
O 1s O_1	6.56	530.81	Hydroxide/Carbonyl	[103, 105-106]
C 1s	2.95	284.6	Surface carbon/reference peak	[107]
C 1s C_1	0.75	288.63	Carbonyl groups C=O	[105],[104]
N 1s	0.55	401.86	Covalent N_2	[107]
N 1s		398.83	Ionic species	[107]

Table 4-2: The XPS data of an ALD ZrO_2 film grown from TEMA-Zr and O_3 at 240 °C.

4.1.5 SIMS analyses of the ZrO_2 films

The SIMS depth profile analysis was utilized for studying the spatial distribution of different species across the sample. In this work, the SIMS was done primarily in order to address one of the questions raised in this work: whether it was possible to vary the stoichiometry of the zirconia films by using different oxygen sources during ALD. The SIMS analyses were carried out on the 16 nm thick ZrO_2 grown from TEMA-Zr/O_3, and the 12 nm thick ZrO_2 films grown from TEMA-Zr/H_2O at the deposition temperatures of 240 °C. The SIMS depth profile of the negatively polarized ZrO^- and ZrO_2^- ions in the ZrO_2 films grown with ozone or water is shown in Figure 4.10. As the two samples were measured at the same operation conditions, the signal intensity is comparable for both ionic species. Hence, from Figure 4.10 one can see that the signals of both species, ZrO^- and ZrO_2^- , are similar to each other, independent on the utilized oxygen source. The ZrO_2/ZrO signal ratio for the ozone grown film was 1.48 (±0.05) and for the water grown film 1.54 (±0.07). This signal ratio shows that in the error range the stochiometry of the two samples is comparable. Therefore, it was concluded that the straightforward variation of the films stoichiometry by using different oxygen sources in ALD process is not possible for pure ZrO_2.

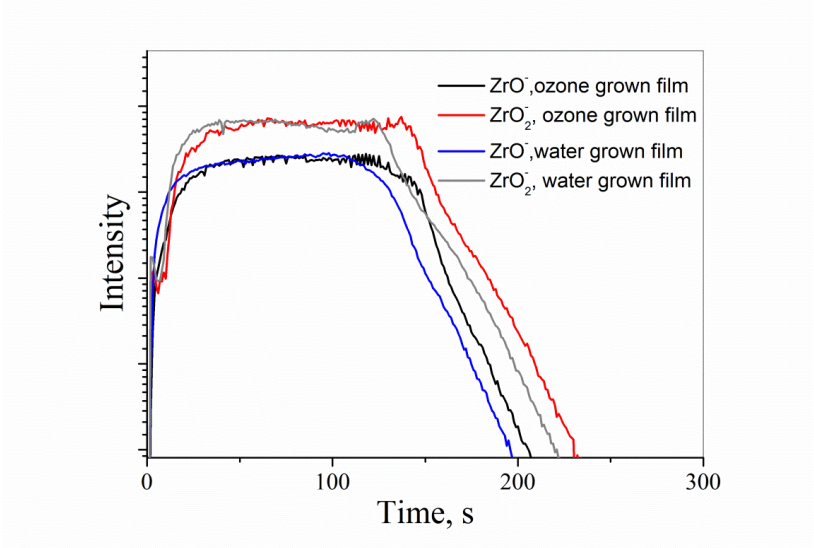

Figure 4.10: SIMS depth profile of the ZrO^- and ZrO_2^- signals in the ozone or water grown ZrO_2 films.

It is interesting to notice that in Lamperti et. al. [11] ZrO_2 films grown at 300 °C by ALD using metal-organic precursor $(MeCp)_2ZrMe(OMe)$ and either water or ozone as oxidants had a different ZrO_2/ZrO signal ratio, which was higher up to 12% for the OGF.

4.2. Morphological characterization of ZrO_2 films

4.2.1. AFM for ZrO_2 films on Si/SiO_2

The morphology is an essential factor in respect to the electrical properties of the oxide films, for example in nano-crystalline HfO_2 films it was found that the regions with the highest conductivity were located at the grain boundaries [108]. Moreover, the conducting filaments were formed at the grain boundaries, where the RS also took place (see Chapter 2). In this study, the morphological properties of the ZrO_2 films were studied by means of AFM, SEM, and TEM analyses.

Firstly, the films grown from TEMA-Zr/O_3 (OGF) and TEMA-Zr/H_2O (WGF) at 240 °C were characterized by means of AFM. The measurements were performed on the films deposited on the Si/SiO_2 substrates which have a very smooth surface, in comparison to the Si/Pt substrates. The AFM images of the 14 nm thick OGF ZrO_2 and 11 nm WGF ZrO_2 is shown in Figure 4.11 (a,c) and (b,d), respectively. The obvious difference in the films morphology was the higher roughness of the WGF. The obtained roughness and grain parameters are given in Table 4-3.

Sample	RMS, nm	Main grain size, nm	Main grain area, nm^2
OGF	0.35	5.8	39
WGF	1.19	7.7	69

Table 4-3. AFM analyses of the ZrO_2 films morphology.

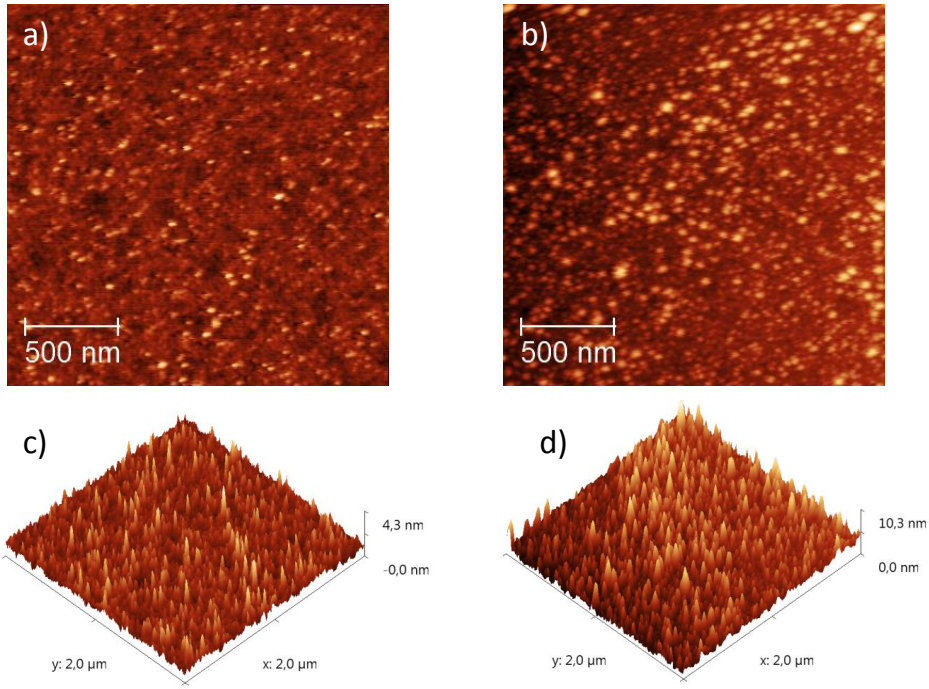

Figure 4.11: The AFM images of the 14 nm thick OGF ZrO_2 (a,c) and 11 nm WGF ZrO_2 (b,d).

The high smoothness of the OGF is in good agreement with the GIXRD analyses, where it was shown that the OGF were amorphous (Figure 4.1). The WGF grown on SiO_2/Si substrates were rather polycrystalline that is also reflected in a higher roughness and grain size (see Table 4-3).

4.2.2. SEM and TEM for ZrO_2 films on Pt/Si

In order to study the ZrO_2 films morphology grown on Si/Pt substrates the SEM analyses was used, as the high roughness of the Pt substrates is no longer appropriate for AFM. The SEM micrographs of the ozone and water grown ZrO_2 films on the Si/Pt substrates are presented in Figure 4.12. Both types of the samples exhibited a grainy structure. However, the OGF contained predominantly cubic shape grains, with a lateral diameter of about 20 nm (Figure 4.12 (a)). On the contrary, WGF (Figure 4.12 (b)) had randomly oriented grains of all

shapes and sizes, which implied a lot of grain boundaries with various orientations and triple points. It was presumed from the presented SEM images that OGF have more homogeneous nanostructure than WGF. This is consistent with the GIXRD result (Figure 4.2 (a)), where the OGF had higher degree of crystalline orientation. A SEM cross-section view of the 14 nm ZrO_2 on Si/Pt substrate is shown in Figure 4.13 (a). The film revealed columnar structure with the crystallite size being in the range of approximately 14-20 nm.

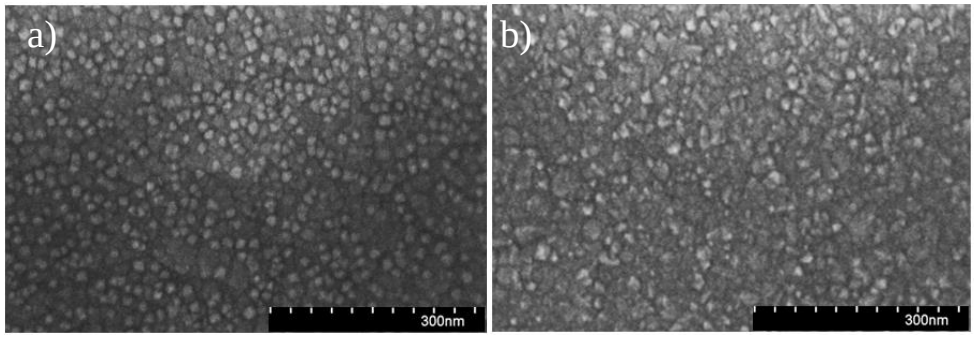

Figure 4.12: (a) SEM planar view of ALD/O_3 grown ZrO_2 (18 nm) and (b) ALD/H_2O grown ZrO_2 (18 nm) [21].

Finally, the TEM cross-sectional imaging was done that is shown in Figure 4.13 (b). Three adjacent grains with different lattice orientations are distinguished. The grain boundary regions between the grains are marked by arrows that are oriented within a certain angle to the film's surface normal. Thus, the grain-structure of the ZrO_2 film can be described as columnar, polycrystalline, and with random in-plane orientation of the grains. No grain boundaries other than those extending through the film are seen in the image or elsewhere in the TEM samples investigated. The grain boundaries are likely to be the most disordered regions in the ZrO_2, and can most readily accommodate vacancies and impurities in the as-deposited films.

As it was discussed in the Section 2.2, pure ZrO_2 is monoclinic at RT and the appearance of *c-t* crystalline state at low deposition temperatures is regarded as meta-stable [71, 72]. The two possible reasons for the meta-stable phase crystallization are: a crystallite size effect and an incorporation of impurities or dopants. Accordingly, on the basis of the investigated ZrO_2 films' structure, morphology, and chemical composition the following conclusion concerning the crystallization of the ALD grown zirconia films into the meta-

stable *c-t* phase was done. The origin of the meta-stable *c-t* structure of the ZrO_2 ALD thin films investigated in this work was addressed primarily to the incorporation of ALD process originating (residual) impurities. The size effect was disregarded from the consideration, because (i) the grain size of the ZrO_2 films grown on Si/Pt substrates was found to be greater than the proposed critical grain size, i.e. 10 nm, and (ii) no monoclinic phase was found after annealing (up to 865 °C) of the ZrO_2 films [77].

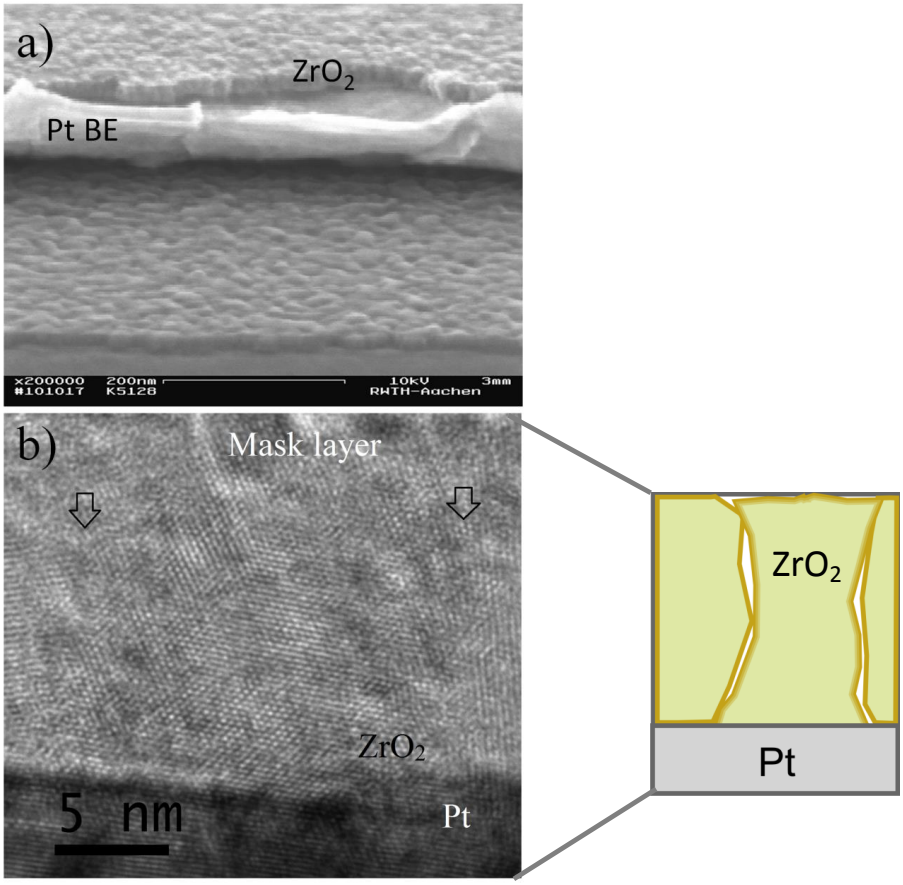

Figure 4.13: (a) SEM micrograph of the Si/Pt/ZrO_2 cross-section. (b) The TEM cross-sectional image of as-deposited ZrO_2 layer on the Si/Pt substrate. The ZrO_2 film is columnar, nano-crystalline, and with random in-plane orientation of the grains.

4.3. Dielectric properties of the ZrO_2 films and the ZrO_2/TiO_2 bilayers

The crystalline quality of the ZrO_2 thin films directly affects the dielectric permittivity values of the respective Pt/ZrO_2/(EAE) capacitor structures. Therefore, the dielectric properties of Pt/ZrO_2/Ti (5 nm)/Pt (30 nm) structures, with the ZrO_2 films grown from water or ozone based processes, were studied.

For zirconium dioxide three different structural modifications are usually considered and their respective dielectric permittivity values are given as $\varepsilon \sim 29$ for the monoclinic phase, $\varepsilon \sim 37$ for the cubic phase and the highest value of about $\varepsilon \sim 47$ for the tetragonal phase [64]. In general, the effective ε-value of the thin films is influenced by the constituting phases, including amorphous phase, texture, strain and electrode interface effects. Lamperti et al. [96] reported effective ε-values of about 30 in ALD ZrO_2 films which exhibit a cubic/tetragonal mixed phase after post-annealing at 800 °C. The ε-value for the anatase phase of TiO_2 is about 40, and for rutile TiO_2 it is about 90 to 110 [109].

Figure 4.14 shows effective permittivity values from the Pt/ZrO_2/Ti/Pt capacitor structures for the films with different thicknesses grown at 240 °C from TEMA-Zr, and the inset shows the ε-values for 18 nm thick ZrO_2 films grown at different temperatures. Films grown by the ALD/H_2O process exhibited slightly higher ε-values, and the increase of the ε-value with increasing film thickness and deposition temperature was more pronounced than for the films grown by the ALD/O_3 process. This feature was addressed to the difference in morphology and crystalline structure described above where the appearance of the tetragonal phase in the ALD/H_2O ZrO_2 samples was more distinct. The overall effective k-values (20-36) were lower than reported ones for the bulk, which could be explained by the presence of some amorphous phase or defects. As could be expected, the raise of the films' thickness and deposition temperature increased the crystallinity of the ZrO_2 films (see Figure 4.2 (a), Figure 4.3), which in its turn increased the dielectric permittivity.

The equivalent oxide thickness ($EOT = t_{high-\varepsilon}(\varepsilon_{SiO_2}/\varepsilon_{high-\varepsilon})$) value can be calculated from the obtained ε-values. The $t_{high-\varepsilon}$ is the thickness of the zirconia layer, ε_{SiO_2} is the dielectric permittivity of silicon of 3.9, and the $\varepsilon_{high-\varepsilon}$ is the effective permittivity of the

zirconia films. The EOT of about 2.8 nm was found for ~16 nm ZrO_2 film grown by ALD/O_3 at 240 °C with the $\varepsilon_{high-\varepsilon} = 21$. The obtained EOT value is in good agreement to the value reported for ozone grown ZrO_2 films from guan-Zr/O_3 [101].

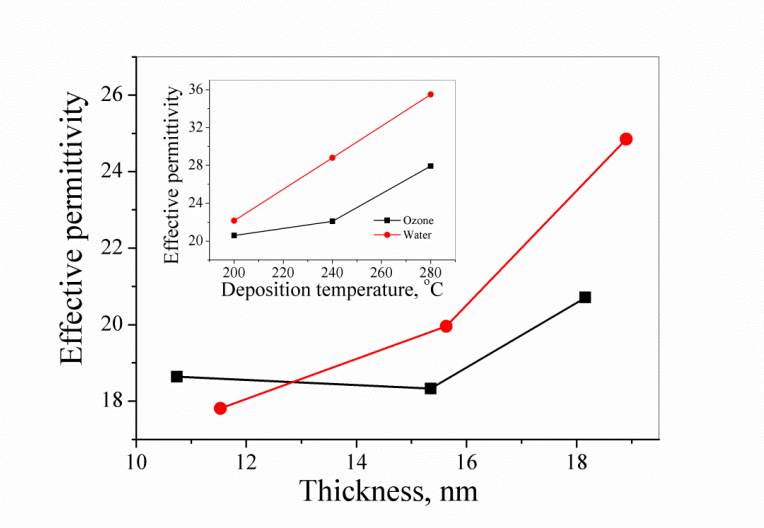

Figure 4.14: The effective dielectric permittivity of capacitor structures with 18 nm thick ALD ZrO_2 films grown at different temperatures; (inset) and with different thicknesses grown at 240 °C [21].

The dielectric properties of the ZrO_2/TiO_2 bilayer structures correlate with the thicknesses and crystalline structure of the constituting layers. The effective permittivity values determined for the corresponding metal-oxide bilayer-metal structures are given in a column on the right side of Figure 4.6. Summarizing the results from GIXRD scans and capacitor measurements it can be concluded that in bilayer capacitors with an effective permittivity below 30, reflections from the cubic/tetragonal ZrO_2 phase can be clearly identified. While the bilayer stack with a higher amount of anatase TiO_2 phase (stack 2 in Figure 4.6) and only small amount of crystallized ZrO_2 had an effective permittivity of about 40. Furthermore, the two samples with the highest permittivity values of about 60 and 70 showed no reflections from any crystalline ZrO_2 phase, and only the peaks of the crystalline TiO_2 anatase phase appeared. Thus, the permittivity values of the MOM capacitors concur well with the structural information of the constituting films obtained from GIXRD analyses.

5. Resistive switching of the ZrO_2 films

5.1. The effect of the oxygen source on the RS performances of $Pt/ZrO_2/Ti/Pt$ devices

To compare the RS behaviour of the devices based on the ALD ZrO_2 films grown with different oxygen sources, the respective devices with three different ZrO_2 thicknesses (11-18 nm) were investigated. Current-voltage measurements were performed on TEMA-Zr ALD/H_2O (WGF) and ALD/O_3 (OGF) ZrO_2 films integrated into MOM planar structures, with Pt BE and Ti (5 nm)/ Pt (30 nm) TE.

The *I-V* curves of the Pt/ZrO_2 (11 nm)/Ti/ Pt stacks grown with either ozone or water are shown in Figure 5.1. Figure 5.1 (a) presents the electroforming curve and subsequent resistive switching cycles for the device with OGF. The device required a low electroforming (EF) voltage of V_{ef} = 0.7 V, and was formed to the high resistance state (HRS). The electroforming step to initiate the resistive switching in the sample with WGF required higher V_{ef} of about 2.8 V (Figure 5.1 (b)), and the sample was formed to the low resistance state (LRS). Although the electroforming voltages for the cells with WGF were larger, the RS occurred at quite comparable set and reset voltages as for the OGF cells.

All devices with 11-18 nm thick ZrO_2 layers integrated into the $Pt/ZrO_2/Ti$(5 nm)/Pt(30 nm) structures, grown from both oxidants, exhibited a unipolar-type RS behaviour. This observation is consistent with earlier studies that showed UP switching, e.g. in the 40 nm thick sputtered ZrO_2 films with the Ti/Pt top electrodes for the Ti thickness of less than approx. 20 nm [17].

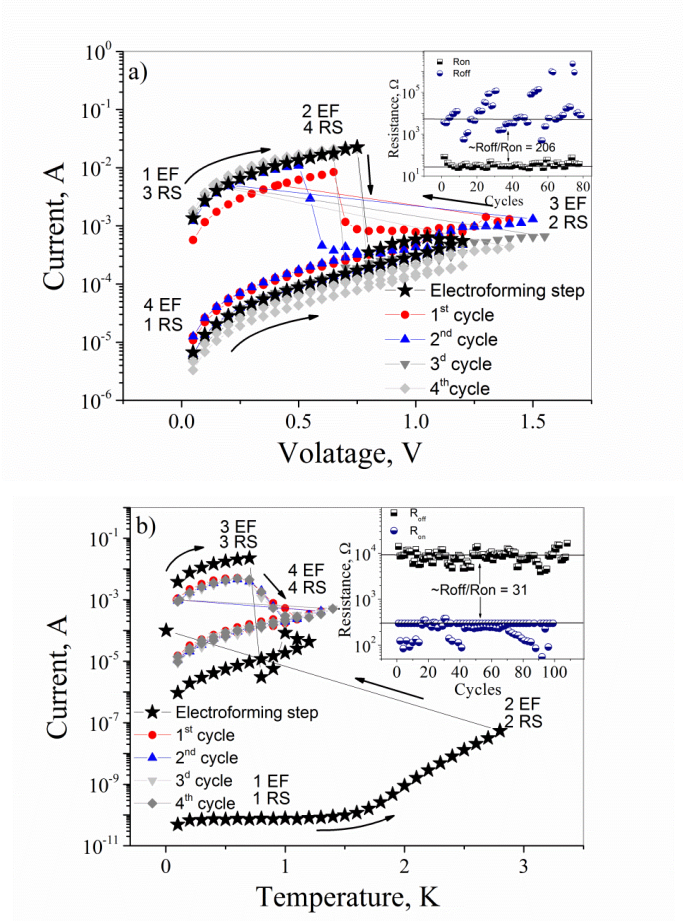

Figure 5.1: Characteristic *I-V* curves showing the electroforming cycle and consequent unipolar type resistive switching of the thin ZrO_2 (11 nm) based planar RRAM cells with the structure of Pt/ZrO_2/Ti (5 nm)/Pt (30 nm) and the pad diameter of 200 µm: (a) ZrO_2 grown with ozone, (b) ZrO_2 grown with water, (insets) the respective resistance values of R_{off} and R_{on} taken at 0.3 V as a function of cycle numbers. The "EF" stays for the electroforming cycle and the "RS" for consequent switching cycles; the numbers show the sequence of the process flow during the EF or RS cycling. The SET current compliance was (a) 2 mA, (b) 1 mA, and for reset both were 100 mA [21].

In general, the electroforming voltage found for the OGF ZrO_2 based devices was lower (1-2V) than for the WGF (2.5-5 V). The EF voltage of the thinner (11 nm) ozone grown ZrO_2 based device was mostly in the range of following V_{set} voltages, see Figure 5.2. Therefore, it might be considered as a forming-free process. The devices with OGF ZrO_2 were mostly formed to the

high resistance state (HRS) in comparison to the cells based on WGF ZrO_2 that were formed to the low resistance state (LRS). One exception was the 18 nm OGF based samples, which exhibited a large variation in the electroforming voltages V_{ef} of different devices. This fact could be explained as the following. In case when the OGF based devices had a relatively low V_{ef}, they were formed to the HRS, and in case of the higher V_{ef} the devices were formed to the LRS. Hence, the occurrence of these two different types of electroforming of the OGF based cells resulted in a large distribution of the V_{ef} values.

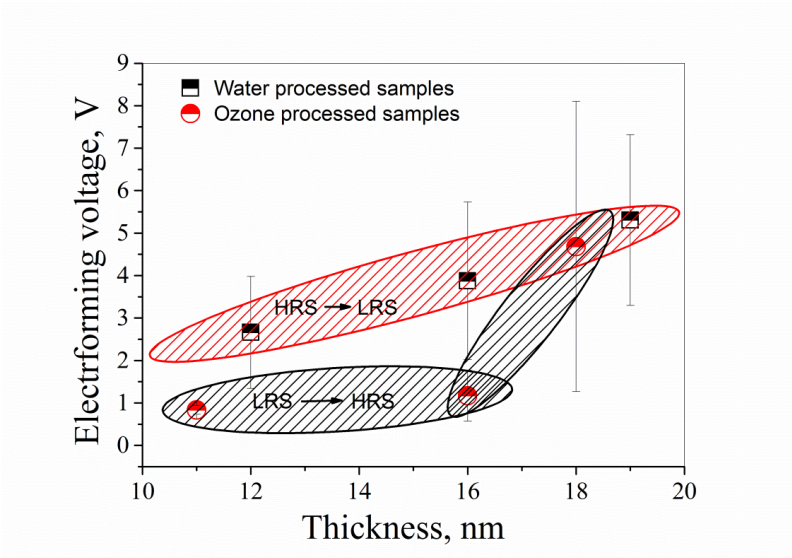

Figure 5.2: Distribution of the electroforming voltages of the TEMA-Zr OGF and WGF based planar Pt/ZrO_2/Ti/Pt devices depending on the ZrO_2 films' thickness. The red area shows the forming to LRS, and the black area shows the forming to HRS.

As a matter of fact, the RS endurance of the devices formed with lower voltages was higher in comparison with those samples which needed higher voltages for electroforming (V_{ef}). The R_{off}/R_{on} ratios for the RS devices with the ZrO_2 films < 16 nm, grown with either water or ozone, were in the range of 30 - $1 \cdot 10^3$. WGF > 16 nm had significantly higher R_{off}/R_{on} ratios that increased up to 10^5-10^6. However, the general trend was that the yield of the films, i.e. the number of working cells on the sample, which were grown with water, was lower. This effect, at one hand, could be addressed to the significant amount of grain boundaries and their random orientation, which leaded to a greater number of ionic defects in the structure

(Figure 4.12). This could result in a stronger rupture of conducting filaments at many different places, as well as made their reconstruction more difficult. On the other hand, the higher V_{ef} for the devices with WGF resulted in a harder breakdown that deteriorated the switching stability and endurance.

Despite the fact that the switching characteristics (V_{set}, V_{reset}) of the devices with OGF and WGF did not differ significantly, the experiments showed that for the RS application the ZrO_2 films grown with ozone with the thicknesses lower than approximately 16 nm were more preferable. Even if obtained R_{off}/R_{on} ratios for the thicker WGF based devices were higher, the electrical stability, endurance, and yield were lower than for corresponding OGF ones. Therefore, in the further studies ZrO_2 films grown with an ozone based ALD process at 240 °C were utilized.

5.2. Effect of Ti layer thickness on the resistive switching properties of Pt/ZrO_2(20 nm)/Ti /Pt devices

The experiments described in the previous section showed that the Pt/(TEMA-Zr) ZrO_2/Ti/Pt devices with Ti top electrode (TE) thickness of 5 nm exhibit unipolar-type resistive switching characteristics, irrespective of the ZrO_2 layer thickness and the oxygen source used for ALD growth. On the one hand, unipolar type RS behaviour is characteristic for thermo-chemically induced processes (TCM). On the other hand, ZrO_2 is also known as a material which shows valence change (VCM) - type RS behaviour and can be operated under bipolar switching conditions [10, 28, 40]. The VCM-type bipolar RS in general consumes less power for a switching event, and therefore might be more attractive with respect to future memory technologies. The VCM is related to a certain amount of oxygen deficiency in the TS oxide layer. Consequently, an approach was performed to increase the amount of oxygen deficiency in the ALD ZrO_{2-x} films by means of the device fabrication.

In this section the effect of the thickness of the EAE top electrode on the RS properties of the 20 nm thick TEMA-Zr/O_3 grown ZrO_2 (@ 240 °C) films is presented. The resistive switching of the ZrO_2 films integrated into the Pt/ZrO_2/Ti/Pt planar devices with the different Ti

electrode thicknesses was investigated, starting from 0 nm of Ti (100 nm Pt TE) up to 90 nm of Ti as the top electrode, where the thin layers of Pt (10-30 nm) were used as a coverage.

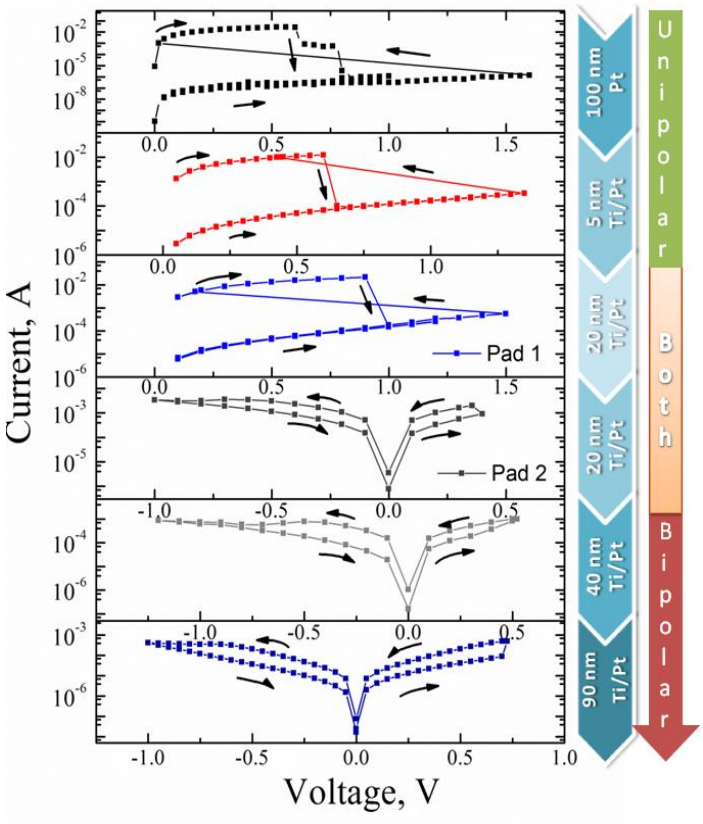

Figure 5.3: Resistive switching of TEMA-Zr ALD/O_3 grown 20 nm ZrO_2 films integrated into the Pt/ZrO_2/Ti/Pt planar device structures with the different Ti electrode thicknesses. The switching polarity changes from unipolar to bipolar with increase of the Ti TE thickness, while for the Pt/ZrO_2/Ti(20 nm)/Pt cells both types of RS polarity were found simultaneously [21].

Prior to the RS characterization all Pt/ZrO_2/Ti/Pt cells were electroformed using positive voltage applied to the Ti/Pt top electrode. Figure 5.3 comprises characteristic RS cycles obtained from the stable switching regime of the ZrO_2 based devices with the different thickness of the TE. In Figure 5.3 from top to bottom the thickness of the Ti TE increases from 0 nm (100 nm Pt TE) to 90 nm, as indicated on the bar on the right side. The x-axes show the applied voltages to the TE and the y-axes the absolute currents plotted on logarithmic scale.

Devices with a Ti TE thickness up to 20 nm showed unipolar type RS characteristics with set voltages in the range of 1.5 V. The calculated R_{off} values are in MΩ regime and the R_{on} values in the range of a few hundred Ω.

The switching polarity of the cells changed from UP to BP with the increase of the Ti TE thickness. In case of the 20 nm Ti TE the presence of the UP and BP switching was found for different cells on the same film sample. The ratio of the numbers of BP and UP switching cells was approximately 1.4. In Pt/ZrO_2/Ti(20 nm)/Pt devices a regime of instability could be characterized by the fact that tiny changes of the configuration which are within the range of experimental variation induced a complete change in the RS polarity of the devices. When the thickness of the Ti TE was further increased, the RS behaviour of the devices has completely changed to the BP type with typical values of V_{set} ≈ +0.5 V, V_{reset} ≈ -1.0 V, and calculated resistance values R_{off} in the 100 kΩ range and R_{on} of about a few kΩ.

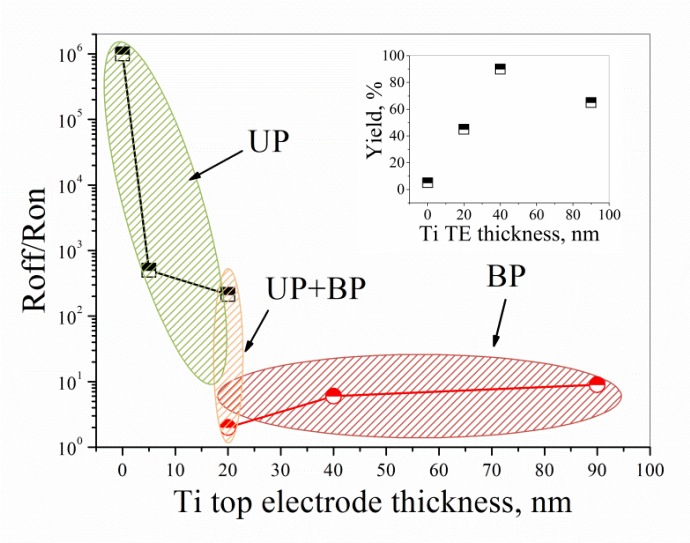

Figure 5.4: The R_{off}/R_{on} ratios for different Ti electrode thicknesses for the Pt/ZrO_2(20 nm)/Ti/Pt. The inset shows the yield (in %) of the working devices out of 20 measured cells, which exhibited at least 3 successful switching cycles for each considered pad [21].

Figure 5.4 comprises the R_{off}/R_{on} values taken at 0.3 V for the samples with the different Ti TE electrode thicknesses. Starting from 0 nm Ti (100 nm Pt TE), the R_{off}/R_{on} ratios of different devices were found to first decrease for the UP switching cells, while after the change to the BP switching a slight increase was identified. Beside the R_{off}/R_{on} ratio values of the different

working cells, also the yield of the sample configuration is important. This information is given in the inset of Figure 5.4. For statistics, minimum 20 investigated devices of each configuration were taken. From the combination of the two graphs, one can see that the minimum of R_{off}/R_{on} ratio was found at the switching polarity transition region (20 nm Ti TE), and the devices with 40 nm Ti TE gave the best yield (90%) with respect to the working cells on the sample, as well as a decent R_{off}/R_{on} ratio close of approx. 10 (slightly depending on the cell). Additionally, it was found that the overall endurance of the bipolar films was higher than that of the unipolar ones. The maximum number of switching cycles in quasi-static regime varied from 10 to 100 for UP switching devices while for bipolar RS cells stable switching up to 10^4 cycles was obtained.

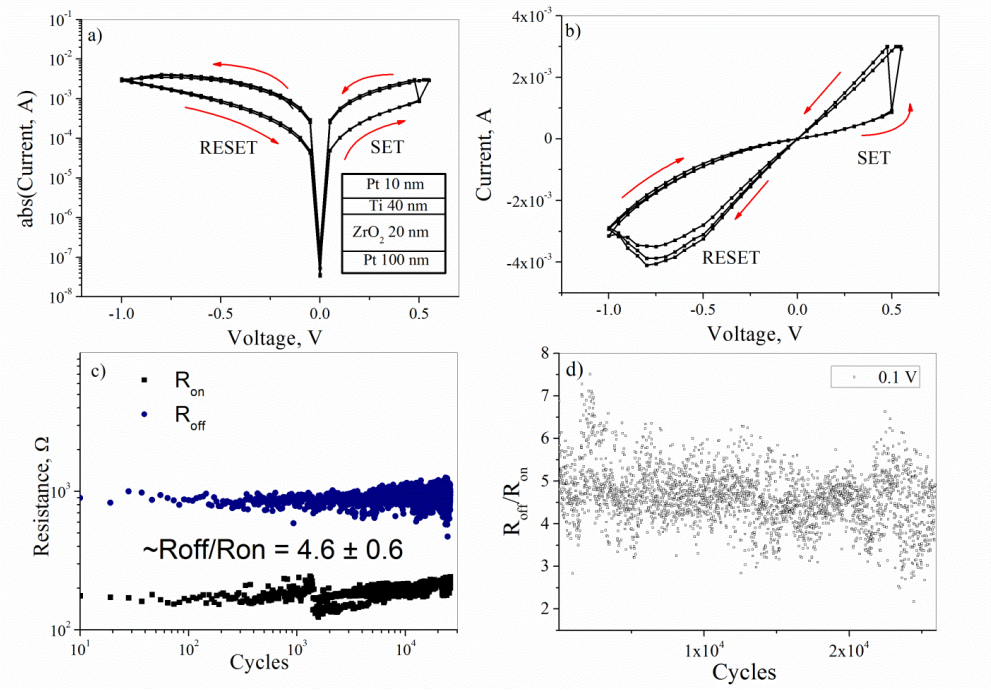

Figure 5.5. Switching characteristics of the planar Pt/ZrO_2/Ti (40 nm)/Pt cell (Ø 200 µm): (a) bipolar switching *I-V* curves in logarithmic scale, (b) *I-V* curves in linear scale, (c) endurance test, (d) distribution of RS ratio taken at 0.1 V.

A long term endurance test was performed for the Pt/ZrO_2 (20 nm)/Ti (40 nm)/Pt cell. Figure 5.5 shows the RS *I-V* curves (a,b) and the endurance test (c) of the Pt/ZrO_2/Ti/Pt cell with the 40 nm Ti top electrode. In the quasi-static mode with a constant voltage ramp the BP switching cells exhibited high endurance of more than 10^4 cycles. The RS ratio distribution is presented in Figure 5.5 (d). The average R_{off}/R_{on} value at 0.1 V was around 5.

The transition of the switching polarity from UP to BP with the increase of the Ti layer thickness is consistent with the results reported by Wang et al. [17] for 40 nm thick, sputtered ZrO_2 films. The authors discussed the formation of TiO_x at the interface of titanium with zirconia due to the high oxygen gettering ability of Ti. By this a TiO_x/ZrO_{2-x} layer could be formed within the Ti/ZrO_2 stack. The thickness of the sub-stoichiometric ZrO_{2-x} layer increased with increasing thickness of the Ti layer. On the contrary, the effective oxide thickness of ZrO_2 and subsequently its dielectric strength were reduced. The decrease of the zirconia effective thickness resulted in a decrease of the forming voltages in the device. The Wang's model, however, did not explicitly explain the origin of the UP switching, and the reason of the switching polarity transformation with increase of the Ti TE thickness.

5.3. The closer investigation of the differences in the UP and BP switching in the TEMA-Zr/O_3 grown ZrO_2 film based devices

The following study was conducted to achieve a better understanding of the fundamental differences between the UP and BP switching in the ZrO_2 based devices. Two different materials of EAE, Ti and TiN, were chosen in order to investigate the RS properties of the zirconia films, which would not be dependent on the particular material of the EAE. The 14 nm ZrO_2 films used for this study were grown from TEMA-Zr and O_3 at 240 °C.

Resistive switching measurements were performed on the Pt/ZrO_2/Ti/Pt and Pt/ZrO_2/TiN devices. The Pt bottom electrode (BE) in the Pt/ZrO_2/Ti/Pt and Pt/ZrO_2/TiN structures devices was 30 nm thick. The thickness of the Ti/Pt and TiN top electrodes (TE) were 5 nm/ 30 nm and 30 nm, respectively. The devices had a cross-bar architecture as presented in Figure 3.5 (b).

I-V curves of the Pt/ZrO_2/Ti/Pt cells were measured in a quasi-static mode with a constant voltage ramp of 2.5 mV/ms applied to the TE while the BE was grounded. The square

pad sizes of the cross-bar junctions chosen for the measurements varied from 2.25 μm^2 to $16 \cdot 10^4$ μm^2. Figure 5.6 presents typical UP switching curves of the Pt/ZrO_2/Ti/Pt device. Unlike previously discussed planar devices, most of the Pt/ZrO_2/Ti/Pt cross-bar cells needed an electroforming step (EF) with electroforming voltages (V_{ef}) of about V_{ef} ≈7-8 V for the smaller pad sizes, while the value was reduced to V_{ef} ≈ 5-6 V for the large ($16 \cdot 10^4$ μm^2) structures. Typically, the cells were electroformed to the ON state. In the UP operation mode (Figure 5.6 (a)), the cell was switched to the OFF and ON states by applying a voltage with the same polarity. The characteristic values of the UP type switching behavior were SET voltages between 2 to 6 V, and RESET voltages of 3 to 4 V, at current compliances of 10 μA and 100 mA, respectively. The endurance of the Pt/ZrO_2/Ti/Pt cells was low, i.e., about 10 stable switching cycles for the smaller pad sizes, and up to 100 cycles for the bigger pad sizes (≥ $1 \cdot 10^4$ μm^2). The small devices with 2.25 μm^2 size often switched only 1 to 5 times. The higher endurance of the larger size pads might have probably related to a larger number of conductive filaments that could be created and disrupted. The obtained ratio of the resistances in OFF and ON state measured at 0.3 V was about R_{off}/R_{on} ~ $1 \cdot 10^6$.

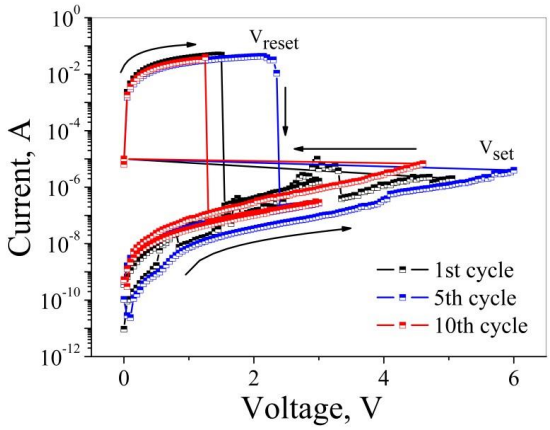

Figure 5.6: Unipolar switching of the Pt/ZrO_2/Ti/Pt device, measured on a pad of $1 \cdot 10^4$ μm^2. Current compliance for the SET and RESET processes was 10 μA and 100 mA, respectively.

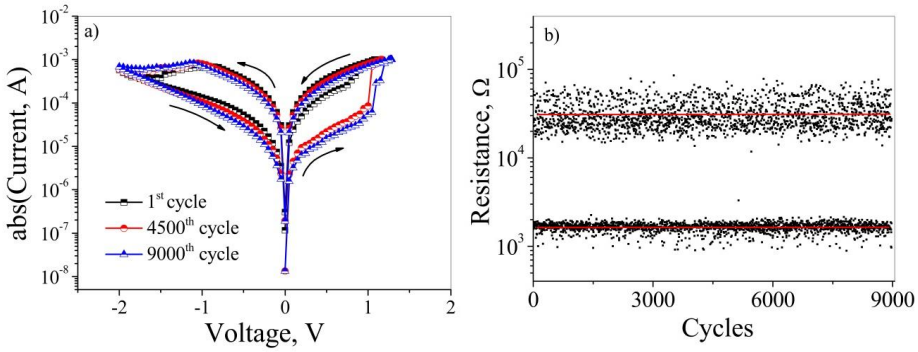

Figure 5.7. (a) Bipolar switching of Pt/ZrO_2/TiN device, measured on a 2.25 μm^2 pad. For the endurance test (b), the R_{off} and R_{on} values are taken at 300 mV.

The resistive switching *I-V* characteristics of the Pt/ZrO_2/TiN crossbar devices were measured in the quasi-static mode with the voltage ramp of 2.5 mV/ms (Figure 5.7 (a)) and in the voltage pulse mode (Figure 5.8). Figure 5.7 (a) shows the *I-V* curves of the bipolar switching Pt/ZrO_2/TiN device, measured in the voltage ramping mode. The devices needed an EF step with positive voltage of 5 V for 2.25 μm^2 pads. After electroforming into the ON state the devices were RESET with a voltage of negative polarity. The subsequent switching of the devices was performed without application of any current compliance. Typical values of the SET and RESET voltages lied between 1 and -1 V, respectively. The devices could be switched more than $9{\cdot}10^3$ cycles without any observable degradation (Figure 5.7 (b)). The average R_{off}/R_{on} ratio of 20 was determined that is a reasonable number for memory application.

Endurance and retention of the bipolar switching Pt/ZrO_2/TiN cells were also studied in the voltage pulse switching mode (Figure 5.8). The pulsing sequences used for the tests are depicted in the insets. The length of the pulses was 100 ms, the waiting time between the pulses was 200 ms. In the pulsing regime the device showed RS stability more than $2*10^3$ cycles (Figure 5.8 (a)). Furthermore, the ON and OFF resistance states were stable for at least 7.5 hours at RT (Figure 5.8 (b)).

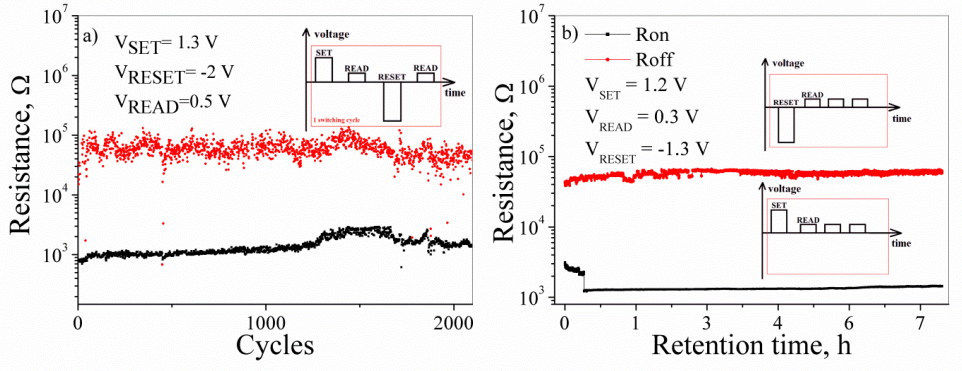

Figure 5.8: (a) Endurance test, and (b) retention test of the Pt/ZrO_2/TiN device in pulsing regime. The length of the pulses was 100 ms, the waiting time between the pulses was 200 ms. The measurement was done on 2.25 μm^2 pad. The current compliance for the SET process was (a) 1 mA, and (b) 0.3 mA; and for the RESET (a) 100 mA, and (b) 10 mA.

In summary, the BP type Pt/ZrO_2/TiN devices exhibited a high yield, reasonable stability with respect to cycling endurance and retention. This is, in contrast to the above discussed UP switching Pt/ZrO_2/Ti (5 nm)/Pt cells.

5.3.1. Temperature dependences of the ON and OFF states

Temperature dependencies (TD) of the ON and OFF resistance states of the UP Pt/ZrO_2/Ti/Pt and BP Pt/ZrO_2/TiN cells were measured from RT to 200 °C. The oven temperature was controlled by means of a LakeShore 331 thermo-controller, regulated by the custom-made software. The resistance values were measured with Keithley source meter. Two types of measurements were carried out. First, the films were heated with a moderate speed of 3 K/min, and a constant voltage was applied to the device, while the current was recorded every 0.5 K. Second, the I-V characteristics from 0V to 0.3 V were measured at several fixed temperatures after thermal stabilization of the system. During the TD measurements the applied voltages were lower than the V_{set} or V_{reset} for the corresponding cells, in order to prevent unwanted switching in to another resistance state.

Prior to the TD measurements the devices were set to a defined ON state at RT by electroforming, reset, and several RS cycles. Then, the ON state resistances were measured with a small signal of 0.1 V during heating of the device from RT to 200 °C. After cooling to RT the device was switched to OFF state, and the respective TD of the OFF state resistance was recorded. As the UP switching cells had very high resistances in the OFF state and the SET voltages were in the range of 4-6 V (Figure 5.6), a reading voltage of 1.0 V was chosen in order to improve the signal to noise ratio.

The TD of the ON and the OFF resistance states of the Pt/ZrO_2/Ti/Pt and Pt/ZrO_2/TiN cells, measured on the $1{\cdot}10^4$ μm^2 pads, are presented in Figure 5.9. The temperature coefficients of the resistance (TCR), denoted as β, are calculated using the following equation:

$$R = R_0\big(1 + \beta(T - T_0)\big) \qquad (5.1),$$

where R_0 is the resistance taken at the reference temperature T_0, which was set to RT. The insets in Figure 5.9 (a) and (b) show the respective graphs for the determination of the TCR value for the ON state of the UP and BP switching devices.

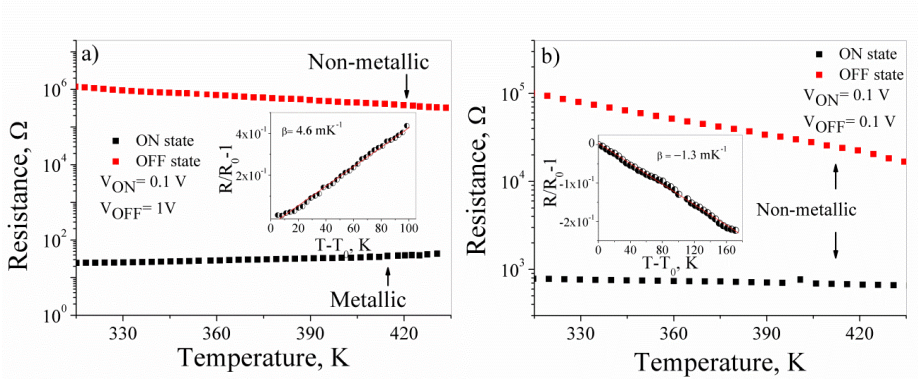

Figure 5.9: Temperature dependences of the ON and OFF state resistances taken at 0.1 V or 1 V for the (a) Pt/ZrO_2/Ti/Pt (UP) and for the (b) Pt/ZrO_2/TiN (BP) cells, measured for the $1{\cdot}10^4$ μm^2 pad size. The insets show recalculated graphs of the respective ON-state resistances from which the TCR values were determined by the least square linear fits according to the Equation (5.1). The calculated TCR values for the ON states were positive and negative indicating a metallic and non-metallic behavior for the UP and BP switching cells, respectively.

With increasing temperature the UP switching Pt/ZrO_2/Ti/Pt cells showed an increase of the ON-state resistance and a decrease of the OFF-state one (Figure 5.9 (a)). Consequently, the ON-state in the UP devices can be regarded as a metallic conducting state, while in the OFF state a semiconductor-type behavior is observed. As an average of different cells a positive TCR value of $\beta = 3.6 \pm 0.1\ \mathrm{mK}^{-1}$ in the ON state was calculated. The value is very close to representative values which are reported for metal bulk material, like for example $\beta = 4.4\ \mathrm{mK}^{-1}$ for Zr, $\beta = 3.9\ \mathrm{mK}^{-1}$ for Pt , and $\beta = 5.4\ \mathrm{mK}^{-1}$ for Ti [110]. In addition to the TCR values, the I-V characteristics of the cells were recorded for certain temperatures. The results are shown in Figure 5.10 (a). Beside the positive TCR, the UP switching cell in the ON state shows a linear I-V curve. This further confirms a metallic-like conducting state for the Pt/ZrO_2/Ti/Pt device in the ON state. The metallic-like TD of the ON state combined with the linear *I-V* characteristics indicate that the UP switching in the Pt/ZrO_2/Ti/Pt cells is characterized by the formation and rupture of the metallic-like conducting filaments.

Upon heating the BP switching Pt/ZrO_2/TiN cells (Figure 5.9 (b)) showed a resistance decrease and, correspondingly, a negative TCR was obtained for the BP-ON state. In addition, the *I-V* characteristics of the BP switching Pt/ZrO_2/TiN cells in the ON state were non-linear (see Figure 5.10 (b)). This observation indicated the formation and rupture of non-metallic-like filaments.

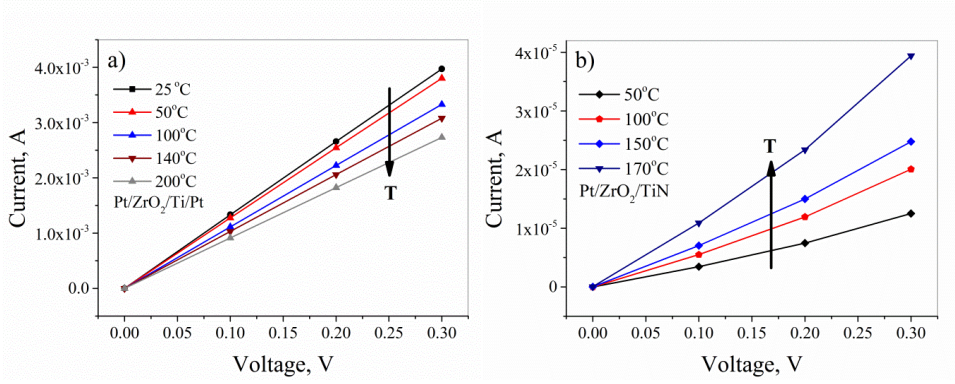

Figure 5.10: ON state I-V characteristics measured at different temperatures of the (a) Pt/ZrO_2/Ti/Pt and (b) Pt/ZrO_2/TiN devices. A downward shift (a) of the *I-V* curves with the temperature increase accounts for an increase of the resistance and hence a metallic-like behavior. Conversely, the *I-V* curves shifting upwards (b) show that the device exhibits semiconducting properties.

5.4. Comparison of the RS in the TEMA-Zr and guan-Zr grown ZrO_2 based devices

Additionally to the comprehensively investigated RS properties of the TEMA-Zr grown films, the films grown from the guan-Zr precursor embedded into the MOM structures were also tested with regard to their RS behavior. The 9 nm guan-Zr/O_3 (@ 300 °C) grown ZrO_2 film was integrated into the cross-bar structure with the 30 nm TiN as a top electrode.

Figure 5.11 (a) shows the first electroforming cycle and the consequent RS curve of the Pt/ZrO_2/TiN device. The measurement was done in the quasi-static mode on the pad of 2.25 μm^2. The cells were formed to ON state with the forming voltages between 4 – 6 V. The Pt/ZrO_2 (guan-Zr/O_3)/TiN devices also revealed a bipolar-type resistive switching and R_{off}/R_{on} ratio was slightly lower, in the range of 3-7, as compared to the Pt/ZrO_2 (TEMA-Zr/O_3)/TiN devices. Furthermore, the Pt/ZrO_2 (guan-Zr/O_3)/TiN devices exhibited a lower endurance up to 10^3 cycles (Figure 5.11(b)), in comparison to the Pt/ZrO_2 (TEMA-Zr/O_3)/TiN cells.

It should be mentioned that the MOM devices with the ZrO_2 layers grown from guan-Zr/O_3 often exhibited bi-stable switching, i.e. during RS cycling the I-V behavior in the ON state was non-liner during some number of cycles, later it switched to linear, followed by the switching back to the non-linear regime. As a consequence, in these samples the R_{off}/R_{on} ratio was not constant.

As the overall switching behavior of the Pt/ZrO_2 (guan-Zr/O_3)/TiN devices, like the R_{off}/R_{on} ratio, endurance, and bi-stable behavior in the ON state, yielded to the respective Pt/ZrO_2 (TEMA-Zr/O_3)/TiN cells, further studies were continued on the devices based on the ZrO_2 films grown from TEMA-Zr.

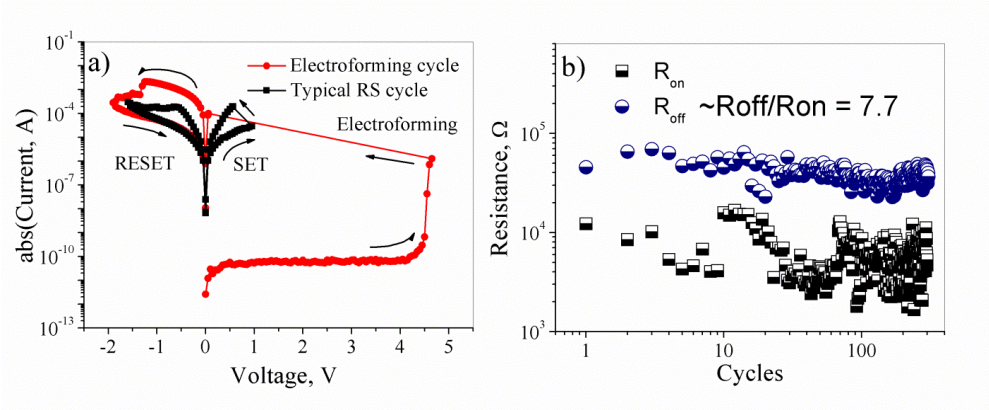

Figure 5.11: (a) Electroforming and RS curves of the Pt/ZrO_2 (guan-Zr/O_3)/TiN device. (b) Endurance test of the Pt/ZrO_2(guan-Zr/O_3)/TiN cell at 0.3 V.

5.5. Resistive switching in the ZrO_2/TiO_2 bilayers

The investigation of the RS multi-layer stacks is generally targeted to the optimization of the RS properties of the devices, e.g. a reduction of the sneaking paths [48], operative voltages, currents [111], as well as an enhancement of the RS ratio [112]. The purpose of this study was to test, beside a single-layer zirconium oxide based devices with different EAE, also the oxide bilayer ZrO_2/TiO_2 structures with different oxidation potentials of the corresponding oxides. For this purpose different stacks were grown in-situ via ALD on the Si/Pt substrates. The ALD TEMA-Zr/TTIP/O_3 process @ 240 °C was chosen for ZrO_2 and TiO_2, since the corresponding ZrO_2 devices have shown an improved performance, compared to the H_2O films. The bilayers were integrated into the planar device structures with the diameter of the investigated pads of 200 µm.

Two separate RS studies on bilayers were conducted: first, on ZrO_2/TiO_2 bilayers planar microstructures fabricated with a thin EAE (5 nm Ti/ 30 nm Pt); second, on the planar microstructures equipped with a thick EAE (30 nm Ti/10 nm Pt). In both studies the thickness and layer stacking sequences of the ZrO_2 and TiO_2 films were varied.

5.5.1. Resistive switching in the ZrO_2/TiO_2 and TiO_2/ZrO_2 bilayers integrated into Pt/bilayer/Ti(5 nm)/ Pt devices

In the first study, the ZrO_2/TiO_2 stacks with the thin electrochemically active TE (5 nm Ti / 30 nm Pt) were investigated. The sequence of the oxide layers as well as their thickness was varied, as presented in the insets of Figure 5.12.

Figure 5.12 (a-d) presents the I-V switching curves depicted for the different bilayer stacks, and the calculated R_{off}/R_{on} values taken at 0.3 V. The electroforming voltages were around 4 V and the forming was typically into the ON state.

Samples with the stack sequence $Pt/ZrO_2/TiO_2/Ti/Pt$ showed unipolar-type resistive switching behavior (Figure 5.12 (a, c)). Comparable R_{off}/R_{on} ratios independent on the thickness of both ZrO_2 and TiO_2 films were obtained (ca 170 – 180) for the samples with zirconia in contact to the Pt BE. Moreover, the $Pt/ZrO_2/TiO_2/Ti$ (5 nm)/Pt cells showed a RS behavior comparable to the $Pt/ZrO_2/Ti$ (5-20 nm)/Pt cells.

In contrast, samples with the stack sequence of $Pt/TiO_2/ZrO_2/Ti/Pt$ showed a non-switching behavior (Figure 5.12 (b, d)), independent of the TiO_2 and ZrO_2 films thicknesses, either {TiO_2 (11 nm)/ZrO_2 (4 nm)} or {TiO_2 (4 nm)/ZrO_2 (14 mn)}.

Assuming the formation of a titanium oxide interface layer close to the slightly reduced ZrO_2 during the electroforming process, the nominal structure of the $Pt/ZrO_2/Ti/Pt$ films might be considered as $Pt/ZrO_2/ZrO_{2-x}/TiO_x/Pt$. Thus, by the redistribution of oxygen in the complete stack the two devices described in Figure 5.1 and Figure 5.12 (a, c) became tentatively similar. This might explain, to a certain extent, the comparable unipolar-type resistive switching characteristics. Following the argumentation the $Pt/TiO_2/ZrO_2/Ti/Pt$ stacks might become $Pt/TiO_2/ZrO_{2-x}/ZrO_2/ZrO_{2-x}/TiO_x/Pt$. Despite of a possible oxygen gradient the structure of these cells might look nearly symmetric. On the one hand, the VCM type switching requires an asymmetric device structure [113]. On the other hand, it is not explicitly clear why the $Pt/TiO_2/ZrO_2/Ti/Pt$ cells, if they would be considered as symmetric structures, do not show unipolar type RS in comparable manner as symmetric $Pt/ZrO_2/Pt$ ones (see Figure 5.3).

In summary, for the ZrO_2/TiO_2 bilayers with the thin EAE top electrode (Ti (5 nm)/ Pt (30 nm)) the stacking sequence, either ZrO_2/TiO_2 or TiO_2/ ZrO_2, effects the RS behaviour while an influence of the thickness of the different oxide layers was not observed.

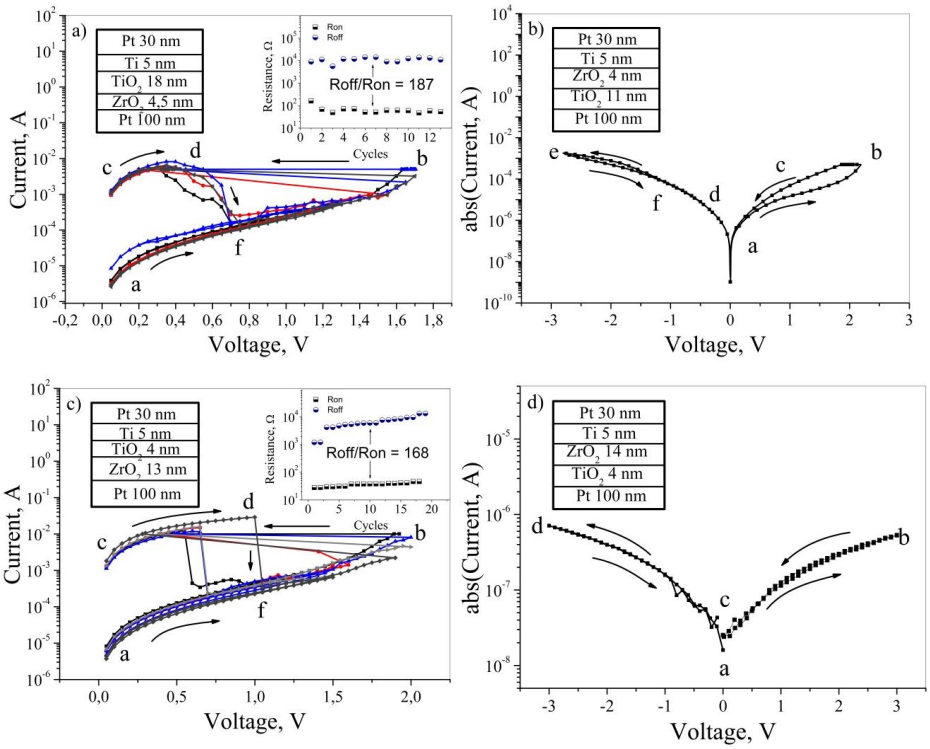

Figure 5.12: *I-V* curves of the four ZrO_2/TiO_2 bilayer structures (insets) with the thin EAE (5 nm Ti/ 30 nm Pt) top electrodes. The unipolar switching is observed in case of the $Pt/ZrO_2/TiO_2/Ti/Pt$ stacks, while the opposite stack combination $Pt/TiO_2/ZrO_2/Ti/Pt$ gives no switching effect. The R_{off}/R_{on} ratio of the (a) and (c) devices is taken at 0.3 V.

5.5.2. Resistive switching in the ZrO_2/TiO_2 and TiO_2/ZrO_2 bilayers integrated into Pt/bilayer/Ti (40 nm)/Pt devices

In the second study, the ZrO_2/TiO_2 stacks integrated into devices with the thick electrochemically active TE (40 nm Ti/ 10 nm Pt) were investigated. The *I-V* curves and the sketches of the four ZrO_2/TiO_2 stack structures with different thicknesses and layer sequences are shown in Figure 5.13. Generally, all cells were leaky in as-deposited state and required an electroforming step at low voltages (-0.8 to -2 V). As in case of the planar $Pt/ZrO_2/Ti/Pt$ stacks, the electroforming voltages were comparable to the switching voltages, that could be

considered as practically a non-forming effect. Although, the forming of the bilayer cells, presented in Figure 5.13 was performed in the negative direction, as shown e.g. in Figure 5.15 (a), in many cases it could be also done with positive voltages, without any affect to the RS properties of cells. An example of the forming of the $Pt/ZrO_2/TiO_2/Ti/Pt$ cell with a positive voltage is shown in Figure 5.14.

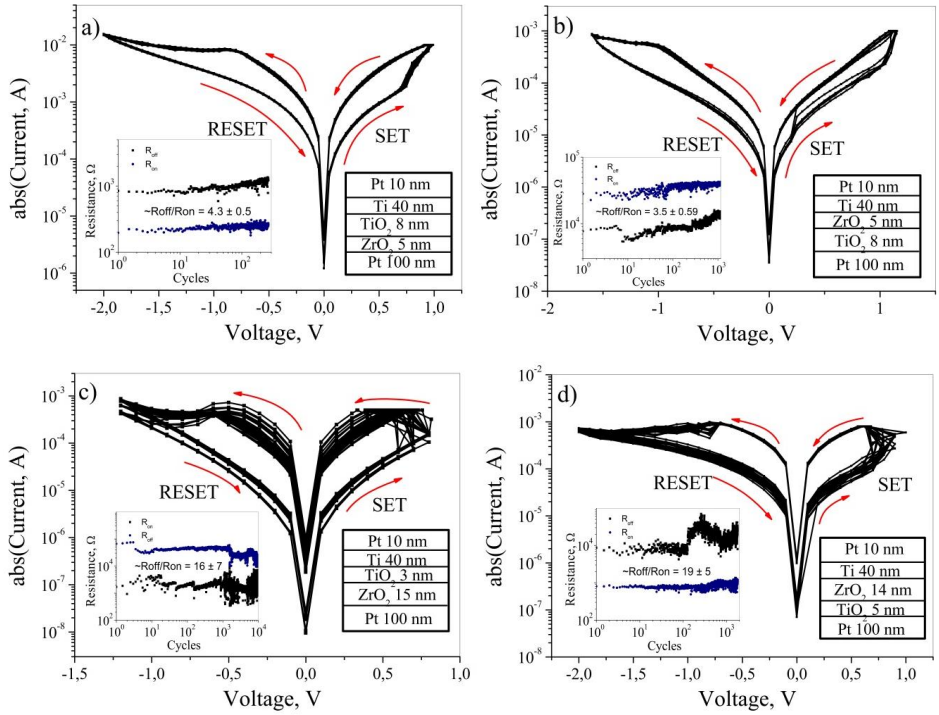

Figure 5.13. *I-V* curves of the different ZrO_2/TiO_2 bilayer structures (insets) with the 40 nm Ti/ 10 nm Pt top electrodes. The bipolar switching was observed for all four devices. The RS ratio in the thicker films was slightly higher (c, d), than in the thinner ones (a, b). The R_{off}/R_{on} ratio (inset) is taken at 0.1 V. The cells' pad diameter 200 μm.

The BP switching was observed for all four devices. The SET was characterized by an abrupt increase of the current at about 0.5 V – 1 V and the system was switched to LRS. Further, at the negative voltage polarity the cells were RESET at V_{reset} of about -0.5 V to -1.5 V.

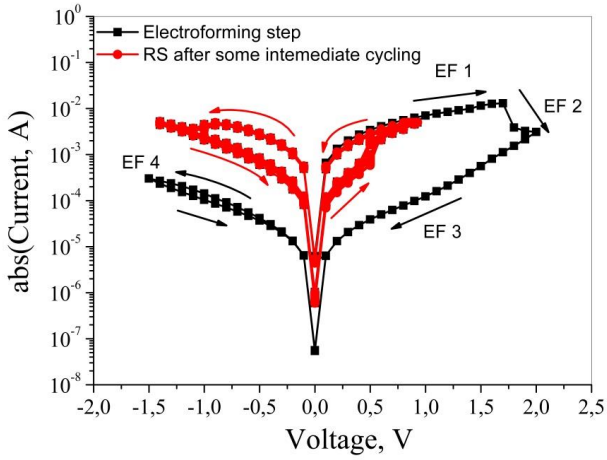

Figure 5.14. Electroforming of the Pt/ZrO_2/TiO_2/Ti/Pt cell with positive voltage (black curve). The consequent cycle *I-V* curve is in red color. The pad diameter of the cell was 200 μm.

As can be seen from Figure 5.13, the samples (c) and (d) had higher total thickness of the stack as well as higher thickness ratio between the layers, in comparison to the samples (a) and (b). The R_{off}/R_{on} ratios of about 15-20 for the thicker devices (c, d) were found to be slightly higher than for the thinner ones (a, b). Interesting to notice that regardless of the practically similar RS parameters (I_{set}, I_{reset}, V_{set}, V_{reset}) of all presented cells, the SET process of the samples (b) and (d) was more "smooth" in comparison to the samples (a) and (c). Regardless the described tiny differences in the RS, the overall RS behavior of the ZrO_2/TiO_2 bilayer stacks with the thick EAE, shown in Figure 5.13, was quite similar for all structures and did not reveal any big differences depending on the sequence of the layers. This result suggests that the actual switching events may appear on the interface between zirconia and titania, as described e.g. by Lee et.al. [114]. The endurance of the thick EAE bilayer devices in a quasi-static mode is shown in the insets of Figure 5.13. All four configurations exhibited high endurance (more than 10^4 cycles) that is comparable with the single-layer Pt/ZrO_2/40 nm Ti/Pt cells (Figure 5.5).

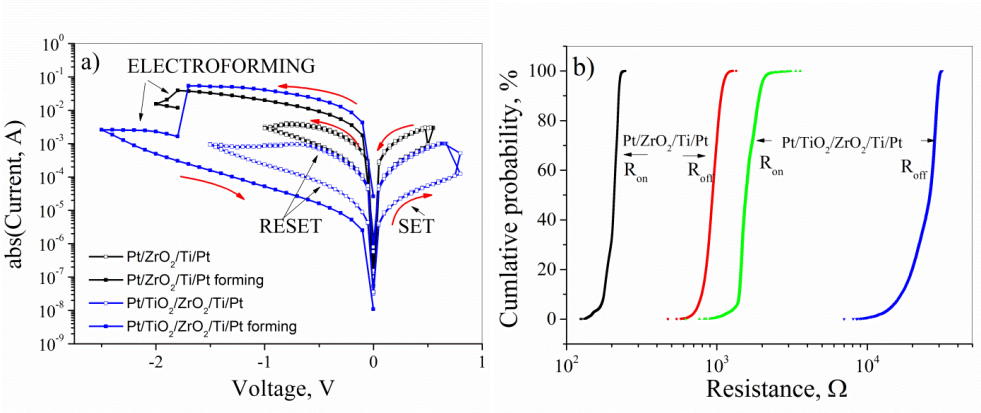

Figure 5.15. (a) Comparison of the *I-V* curves of the single-layer ($Pt/ZrO_2/Ti/Pt$) and the bilayer ($Pt/TiO_2/ZrO_2/Ti/Pt$) devices with the 40 nm Ti/ 10 nm Pt top electrodes (Ø 200 µm). Both cells were electroformed at the negative voltages of about -2 V. The operative current of the bilayer devices was reduced approximately an order of magnitude in comparison to the single-layer $Pt/ZrO_2/Ti/Pt$ cells. (b) Cumulative probabilities of the resistance values taken at 0.1 V for the single- ($2.6 \cdot 10^4$ cycles) and bi-layer (10^4 cycles) devices clearly demonstrate a higher R_{off}/R_{on} ratio in case of the bilayer device.

It is interesting to compare the RS characteristics of the 20 nm thick ZrO_2 based single-layer devices with the approximately 20 nm thick (~19 nm) bilayer structures, when the both devices had the same thickness (40 nm) of Ti TE. Figure 5.15 (a) presents electroforming and the consequent *I-V* switching curves of the planar $Pt/ZrO_2/Ti/Pt$ and $Pt/TiO_2/ZrO_2/Ti/Pt$ cells, where a TiO_2 (5 nm)/ZrO_2 (14 nm) bilayer structure is depicted in the inset of Figure 5.13 (a). As can be seen from Figure 5.15 (a), the operating current was reduced to an order of magnitude in the bilayer structure in comparison to the single-layer cell. However, the forming voltage remained the same for both cells. It can be noticed, that the forming voltages of the single- and bi-layer planar devices, which were based on the OGF, were in the same range, i.e. from -2 to 2 V, and were comparable to their V_{set} and V_{reset} voltages. The switching ratio of the bilayers was slightly higher (15-20) than for the single-layer devices (5-10), which can be well seen from the cumulative probability curves for the resistance values taken at 0.1 V (Figure 5.15 (b)).

The enhancement of the RS ratio as well as the reduction of the operative currents in the bilayers, in comparison to the corresponding single-layers (with the thick EAE), showed that addition of the extra layers into the ZrO_2 based RS device enables to improve its RS properties,

in addition to varying the thickness of the EAE in single-layer cells. However, the EAE thickness in the bilayers has to be also considered, as it was shown that the thin EAE bilayers were switching poorly (only the samples with the $Pt/ZrO_2/TiO_2/Ti/Pt$ configuration showed UP switching), whereas in case of the thick EAE the stable BP switching was observed for all investigated structures.

6. Impedance spectroscopy

Impedance spectroscopy (IS) is a powerful tool for investigation of the electric properties of the materials. It enables a separation of the electrical contributions from the different regions of the samples. In the recent years, impedance spectroscopy was successfully used as an analytical technique in RS application. Impedance spectroscopy (IS) measurements are sensitive to changes that arise in RRAM devices upon switching from high-ohmic OFF state to the low-ohmic ON state, especially for cases where interface switching or shortening of the depletion layer by the conducting filament are involved [115-119].

The thin EAE Pt/ZrO_2/Ti (5 nm)/Pt (UP) devices and the thick EAE Pt/ZrO_2/TiN (30 nm) (BP) cells were investigated by IS. The characteristic properties of the investigated cells in the present study comprised (i) the low ZrO_2 oxide film thickness of 14 nm, (ii) the oxides' polycrystalline microstructure with columnar shaped grains and straight, vertical grain boundaries, and (iii) different thicknesses of the chosen top EAE. The columnar microstructure might be described by a parallel network of grain (G) and grain boundary (GB) regimes. For the most part, a differentiation of the grain and grain boundary properties is complicated by means of IS. This is because the Voigt elements of the corresponding equivalent network cannot be calculated unambiguously [115].

In this study, we applied a slightly different approach by comparing the impedance data that were determined for the RS devices in their ON and OFF states with the equivalent network elements determined for these devices in their pristine state. In addition, in order to be more precise in describing the actual device structure we described the grain and grain

boundary regime by a parallel circuit of an ohmic resistor *R* and a phenomenological constant phase element (CPE) [120] which describes an imperfect capacitor. The *CPE* accounts for a more accurate description of the nano-crystalline, cubic/tetragonal material which has to be regarded as highly disordered media. Nevertheless, in case of a parallel connection of *CPE* and *R*, a real value of the capacitance *C* can also be calculated applying an equation which has been developed by Hsu and Mansfield [121]. In the following, the impedance spectra were taken at RT for the frequency range from 1 Hz to 1 MHz for the devices in their pristine state, low resistance (ON) and high resistance (OFF) states. The values of the elements of the respective equivalent networks are summarized in Table 6-1 at the end of this section.

6.1. Pristine states

Figure 6.1 (a) and (b) show the Nyquist plots for the pristine states of the Pt/ZrO_2/Ti/Pt and Pt/ZrO_2/TiN devices, respectively, determined for a pad size of 100 μm^2. For both types of cells a part of a large semicircle was observed consistent with the IS of an insulating capacitor. The dots represent experimental values and the lines respective fitting curves. The arrows in the figures show the direction of the frequency decrease. The corresponding equivalent circuits which are applied for the fitting of the data are shown in the figures' insets. The inductance of the leads (L_{leads}) and the resistance of the interfaces and contacts (R_i) were considered in the simulation by a serial element L_{leads}-R_i, while the capacitors in pristine state were in best manner described by a parallel circuit of a resistor and a constant phase element, $R_2|CPE_2$.

The impedance of a R|CPE parallel circuit is given as:

$$Z_{R|C} = \left(\frac{1}{R} + \frac{1}{Z_{CPE}}\right)^{-1} \quad (6.1).$$

The impedance of a CPE is calculated from

$$Z_{CPE} = \left(\frac{1}{Q}\right) \cdot (i\omega)^{-\alpha} \quad (6.2),$$

where Q and α are parameters, which are independent of the circular frequency ω [122]. For the limiting case, when $\alpha = 1$, Q equals C, the capacity of the system. The case $\alpha \neq 1$ addresses the case of a disordered system which might be characterized by a distribution of relaxation times τ scattered around the mean value $\tau_{max} = (\omega_{max})^{-1}$[123]. Consequently, parameter Q describes a "pure" resistance in the case of $\alpha = 0$ ($Q = 1/R$). According to the the theory of CPE [120, 121] the real capacitance of the system can be calculated from the CPE elements as follows:

$$C = R^{\frac{1-\alpha}{\alpha}} \cdot Q^{\frac{1}{\alpha}} \qquad (6.3).$$

Basically, the inductance (L_{leads}) and the resistance (R_{leads}) of the leads have to be taken into account in the fitting process. The value of L_{leads} was found to be equal to ~1 mH. The value of R_{leads} is generally less than 100 Ω. However, the R_i value, obtained from the fitting of the both devices was about 4 kΩ, which could be interpreted in the way that apparently some type of interface layer or "virtual electrode" formed between the EAE and the films, presumably, during the device fabrication, which appeared as an increased electrode resistance. The serial (L_{leads}-R_i) elements were considered in all subsequent IS fitting procedures, while the elements are omitted in the equivalent schemes for the different ON and OFF states. The fitting parameters for $R_2|CPE_2$ element which describe the pristine states of the Pt/ZrO_2/Ti/Pt and Pt/ZrO_2/TiN devices are listed in Table 6-1. The resistances of the RS devices in pristine state at RT were in the order of tera-ohms, indicating a good insulating behavior. In accordance, the determined value of α was very close to 1. Using equation (6.3) the real capacitances of the Pt/ZrO_2/Ti/Pt and Pt/ZrO_2/TiN cells were calculated, giving the values of about 1.78 pF and 1.85 pF, respectively. If a certain tolerance in the device size was taken into account, we could summarize that these devices with the different thicknesses of the EAE revealed practically identical, capacitor-like impedance properties in their pristine states. Assuming thin parallel plate capacitor geometry the effective dielectric permittivity of the 14 nm ZrO_2 layers could be estimated from:

$$\varepsilon = \frac{C \cdot d}{A \cdot \varepsilon_0} \qquad (6.4),$$

with A being the capacitor area, and the vacuum dielectric constant ε_0 =8.854×10^{-12} F m^{-1}. Inserting A = 100 μm^2, d=14 nm, C = (1.8 ± 0.05) pF results in a mean value of the calculated

effective dielectric permittivity of about (28.5 ± 1.0) which is in good agreement with the effective dielectric permittivity values obtained for the ALD grown ZrO_2 films from a more basic analysis in one of our studies [21], presented in Figure 4.14.

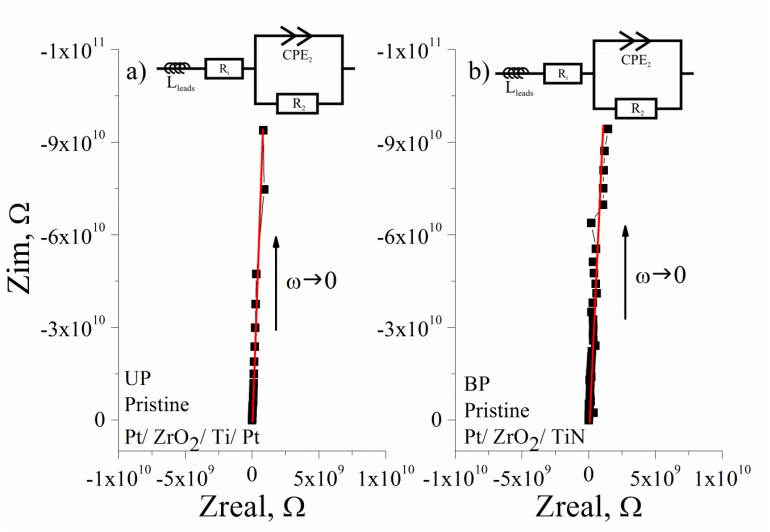

Figure 6.1. Nyquist plots of the impedance spectra taken from the a) Pt/ZrO_2/Ti/Pt and b) Pt/ZrO_2/TiN cells in pristine state for frequencies from 1MHz to 1Hz. Both devices behave as nearly identical capacitors, independently from the electrode configuration.

6.2. ON states

After the characterization of the pristine states, the devices were electroformed and switched into the low resistance ON state according to the procedure which is described in Section 5.3. The ON states were then again characterized by impedance spectroscopy. Figure 6.2 (a) and (b) show the Nyquist plots of the Pt/ZrO_2/Ti/Pt (UP) and Pt/ZrO_2/TiN (BP) devices in ON state, respectively. The ON-state Pt/ZrO_2/Ti/Pt cells exhibited extremely low impedance values which made the IS measurement of the cross-bar structures in the two probe configuration rather difficult due to artifacts arising from the external circuit parasitic elements [123]. At higher frequencies the imaginary impedance Z_{im} component shifted to

positive values and the IS characteristics appeared in the fourth quadrant of the coordinate plane (see Figure 6.2 (a)). A similar behavior is reported in other studies, like for example by Kundozerova et al. for Nb_2O_5 RS cells [124] and by Jiang et al. for the metallic conducting low resistance state of HfO_2 based RS devices [116]. Instead of trying an equivalent circuit fitting, the IS behavior of the UP cell in ON-state was experimentally compared to a standard 62 Ω resistor. From the similar form of the IS of the simple resistor and of the UP ON state device (see Figure 6.2 (a)) we conclude that the ON state of the UP switching $Pt/ZrO_2/Ti/Pt$ cells is characterized by a metallic conducting state. This is in good agreement to the observed linear *I-V* characteristic and to the positive TCR value.

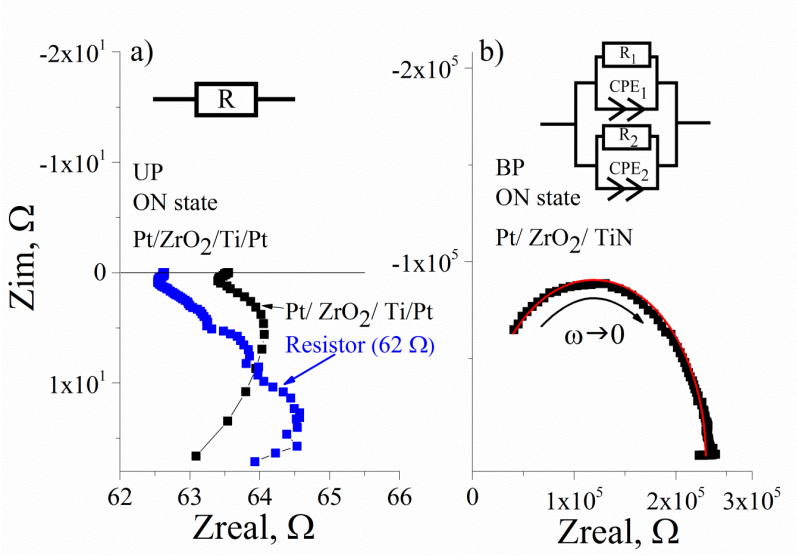

Figure 6.2. Nyquist plots of the impedance spectra taken from the a) $Pt/ZrO_2/Ti/Pt$ and b) $Pt/ZrO_2/TiN$ cells in their ON states for frequencies from 1MHz to 1Hz.

In contrast, the Nyquist plot for the ON state of the BP switching $Pt/ZrO_2/TiN$ device in Figure 6.2 (b) shows a slightly distorted semicircle. This result from the IS measurements is in good agreement to the non-linear *I-V* characteristic (Figure 5.10 (b)) and semiconductor-like temperature dependence (Figure 5.9 (b)) found for the BP ON state. The semi-full arc in Figure 6.2 (b) could be best fitted using a parallel R|CPE element. The values for the equivalent elements were $R \approx 225$ kΩ and $Q \approx 2.084$ $pF/s^{1-\alpha}$ with $\alpha = 0.984$. All values and tolerances are also listed in Table 6-1. In comparison to the pristine state, the BP ON state

shows a slightly larger CPE value with a slightly decreased α value that also corresponds to a significantly decreased insulation resistance. Again, the value of R obtained from the IS analysis fits very well with the value of R_{on} as obtained from the quasi-static switching experiments.

Although the modeling of the microscopic structure of the ZrO_2 based RS devices is the topic of the Chapter 7, at this stage the RS model has to be shortly introduced in order to motivate the further fitting procedures. According to the structure of the ALD ZrO_2 films consisting of columnar shaped crystallites and grain boundaries that extend from the bottom to the top electrode, one might assume an equivalent circuit of two R|CPE elements in parallel, while one element, here $R_2|CPE_2$, stands for the properties of the grains and the other element, i.e. $R_1|CPE_1$, represents the characteristics of the grain boundaries (inset in Figure 6.2 (b)).

For the clarity, I would first like to show that the procedure of taking two parallel R|CPE blocks instead of one is mathematically and physically correct. The equivalent schemes presented in the insets of Figure 6.3 (a) and (b) are similar, and the R and CPE in the inset of the Figure 6.3 (a) can be written in respect to the R_1, R_2, CPE(Q_1) and CPE(Q_2), given in the inset of Figure 6.3 (b), as follows:

$$Z_R = \frac{1}{Z_{R_1}} + \frac{1}{Z_{R_2}} \qquad (6.5),$$

and

$$Z_{CPE} = Z_{CPE(Q_1)} + Z_{CPE(Q_2)} \qquad (6.6),$$

if we assume that CPE elements present plain capacitors with a small degree of structural inhomogeneity, and the parameter α is taken equal for both (a) and (b) cases. The fitting of the IS data of the BPS cell with the equivalent scheme with two parallel R|CPE blocks instead of one, is bonded to an increase of the total CPE(Q) value of the cell after forming as compared to the pristine state. The increase of the CPE(Q) value can be addressed to the appearance of the second phase, as the two-(R|CPE)-block scheme presents a standard vertical two parallel phase equivalent model [122]. This corresponds to the empirical RS model presented in the next chapter that describes the zirconia film in the electroformed device consisting of insulating grains and strongly reduced grain boundary cores.

In the 'ZrO_2 RS model' we assume that the dominant RS events may happen at the weakest points of the device structure, which are the grain boundaries. A comparable assumption has been introduced for the modeling of the RS behavior of HfO_x-based devices by Bersuker et al. [125]. The BP switching Pt/ZrO_2/TiN devices revealed a highly insulating behavior in the pristine state, while for the ON-state a significantly reduced resistance was measured. Consequently, the approach to describe the ZrO_2 thin film microstructure by an equivalent network of two R|CPE circuits in parallel where one element represents the pristine state ($R_2|CPE_2$) and one element represents the additional leakage path in the RS state ($R_1|CPE_1$), might be reasonable. It is assumed that the resistive switching events occur at the very thin grain boundary cores and that the main area of the ZrO_2 based capacitor, i.e. the grains, remains unaffected from the electroforming. Therefore, the R|CPE element for the BP ON-state is replaced by a parallel $R_2|CPE_2$ and $R_1|CPE_1$ network which is shown in the inset of Figure 6.2 (b). From the complementary IS fitting which takes the properties of the pristine state into account reasonable values for the properties of the semiconducting filaments could be extracted. From this fitting procedure the properties of the conducting filament giving values of R_1 = 225 kΩ and Q_1 = 60 fF/$s^{1-\alpha}$ and α=1.00 are derived, taking R_2 = 47 TΩ and Q_2 = 1.708 pF/$s^{1-\alpha}$.

6.3. OFF states

After the IS measurements of the ON states, the cells were subjected to several switching cycles before they were set to the OFF state for further impedance characterization. Figure 6.3 (a) and (b) show the Nyquist plots of the Pt/ZrO_2/Ti/Pt (UP) and Pt/ZrO_2/TiN (BP) devices in the OFF state, respectively. The impedance spectra of the Pt/ZrO_2/Ti/Pt cell present a semicircle, and a non-complete semicircle for the Pt/ZrO_2/TiN cell. In a first step, both arcs were fitted by a single R|CPE element. The values which were determined from the fitting are given in Table 6-1.

For the OFF state of the UP switching Pt/ZrO_2/Ti/Pt device, a high insulation resistance of about R = 1.45 GΩ was obtained while the value of the CPE element results in an equivalent capacitance (see eq. (6.4)) of C ≈ 0.20 pF. The most striking outcome from the

analysis of the UP OFF state is that the capacitance of the UP device after electroforming and switching is decreased to about one ninth of the value for the pristine device. A possible interpretation for this observation will be given in the discussion Chapter 7.

When the IS data for the OFF state of the BP switching Pt/ZrO_2/TiN device was fitted with the single R|CPE element, the increased insulation resistance of $R \approx 750$ kΩ and larger value for the CPE element of $Q \approx$ 2.098 pF/$s^{1-\alpha}$ with α =0.992 as compared to the BP ON state were found.

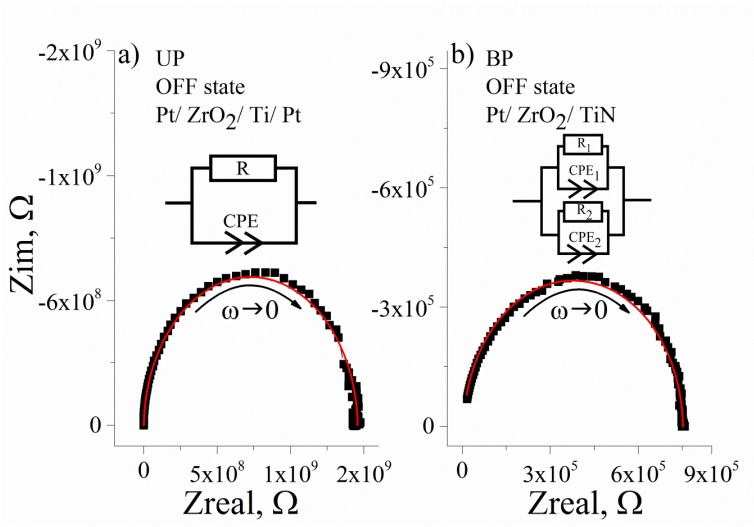

Figure 6.3. Nyquist plots of the impedance spectra taken from the a) Pt/ZrO_2/Ti/Pt and b) Pt/ZrO_2/TiN cells in OFF state for frequencies from 1MHz to 1Hz.

In parallel to the discussion of the BP ON state, also the BP OFF state IS was fitted with an equivalent circuit of two parallel R|CPE blocks, again with the elements of block R_2|CPE_2 taken from the fitting of the device in the pristine state. Accordingly, from the fitting the properties of the conducting filament in the OFF state being R_1 = 750 kΩ, Q_1 = 325 fF/$s^{1-\alpha}$ and α=0.99 could be derived. Analog to the case of the ON-state filament, also the properties determined for the OFF-state filament are reasonable with respect to the microstructure and the electrical properties of the BP RS ZrO_2 based devices.

It should be remarked that any contribution of a formed electrode/film interfacial layer which for example has been observed for thick MIM devices from Pt/ (750 nm) $SrTiO_3$ / Nb:STO [115] and for ITO/TiO_2/ITO structures [116] has not been found in these studies.

This might be explained with the very low thickness of about 14 nm of the insulating ZrO_2 layer.

State/ Device parameters	Pristine		ON		OFF	
	UP	BP	UP	BP	UP	BP
V_{AC}, mV	500	100	100	10	500	10
L_{leads}, mH	0.9 ± 0.5					
R_i, Ω	4508±982	3951±168	-	3951±168	4508±982	3951±168
R, Ω	-	-	~63	(225 ± 0.2)e3	(1.55 ± 0.05)e9	(748 ±1.2)e3
Q, $pF/s^{1-\alpha}$	-	-	-	2.084±0.061	0.022±0.005	2.098±0.005
α	-	-	-	0.984±0.001	0.988±0.001	0.992±0.002
C, pF	-	-	-	**1.65**	**0.20**	**1.88**
R_1, Ω	-	-	-	(225 ± 0.2)e3	-	(748 ±1.6)e3
Q_1, $pF/s^{1-\alpha}$	-	-	-	0.06 ± 0.01	-	0.325 ± 0.059
α_1	-	-	-	1	-	0.99 ± 0.01
C_1, pF	-	-	-	**0.06**	-	**0.278**
R_2, Ω	(47.7 ±1.81) e12	(47.7 ±1.81) e12	-	(47.7 ±1.81) e12 (*)	-	(47.7 ±1.81) e12 (*)
Q_2, $pF/s^{1-\alpha}$	1.708±0.002	1.772±0.019	-	1.772±0.019(*)		1.772±0.019(*)
α_2	0.990±0.001	0.992±0.001	-	0.992±0.001(*)	-	0.992±0.001(*)
C_2, pF	**1.78**	**1.85**		1.85(*)	-	1.85(*)

Table 6-1. Fitted values of the impedance parameters for the $Pt/ZrO_2/Ti/Pt$ (UP) cells, and $Pt/ZrO_2/TiN$ (BP) cells in the pristine, ON and OFF states. (*) The pristine state input parameters for fitting the device impedance data with the two R|CPE block scheme.

6.4. Bode plots

Before I continue with the discussion of the electrical properties of the ZrO_2 based RS devices on the basis of a micro-structural model of the central ZrO_2 films, the consistency of the impedance analysis should be checked. This is done by a comparison of phase shift of the complex impedance data for all three states (pristine, ON, and OFF) for both UP and BP switching devices by means of a Bode diagram (Figure 6.4). The graph clearly demonstrates, that the behavior of both types of pristine cells is best described by a constant phase element with α close to 1 which is characterized by a phase shift of -90°. In contrast, clear

differences can be observed for the devices after forming. The metallic behavior of the UP ON state (phase ≈ 0°) is consistent with the positive TCR value obtained from the temperature dependency (Figure 5.9 (a)). However, in the OFF state the UP switching system is highly insulating. In contrast, the BP switching cells in the ON and OFF states exhibit only slight differences in their IS behaviors, which is consistent with the observed semiconducting behavior and the small R_{off}/R_{on} ratio.

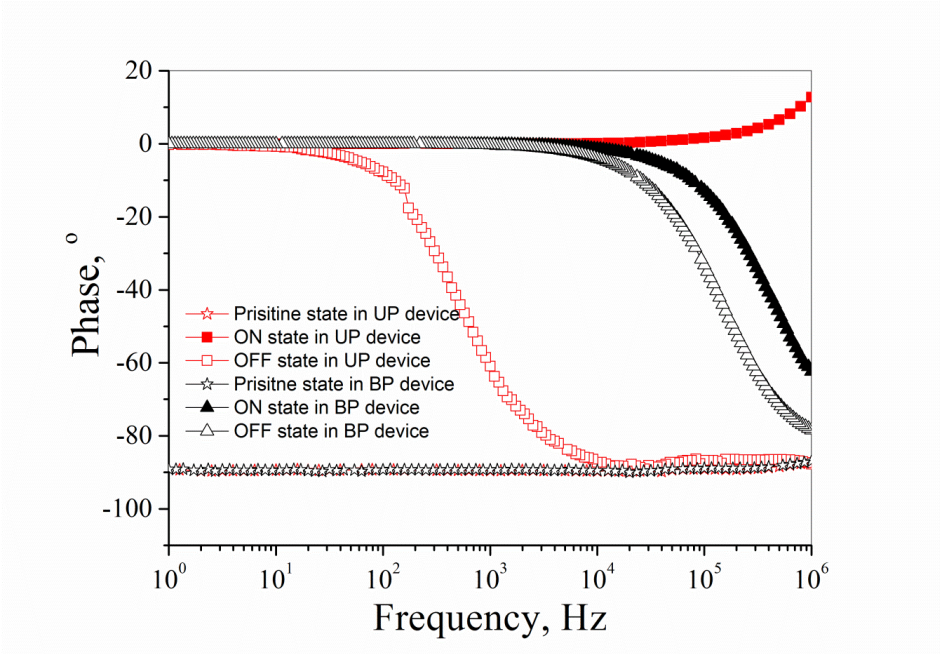

Figure 6.4. Bode plots of the pristine, ON and OFF states of the UP ($Pt/ZrO_2/Ti/Pt$) and the BP ($Pt/ZrO_2/TiN$) devices. The responses of the devices in their pristine state overlap in the Bode-graphs, while the switching devices give clearly different responses.

7. Differentiating the UP and BP switching in $Pt/ZrO_2/(EAE)$ devices

7.1 Empirical model of RS in $Pt/ZrO_2/(thin\ EAE)$ and $Pt/ZrO_2/(thick\ EAE)$

The following section discusses the effect of the morphology and structure of the TEMA-Zr/O_3 (@ 240 °C) grown 14 nm ZrO_2 films in as-deposited state and the influence of the thickness of the EAE on the polarity of the observed switching behavior in $Pt/ZrO_2/(EAE)$ devices. For that a ZrO_2 RS model based on the actual oxide micro-structure and EAE thickness is proposed. The polycrystalline meta-stable cubic-tetragonal (c-t) structure of the ZrO_2 films in as-deposited state is attributed to an effect of partial phase stabilization due to incorporation of residual ALD process related impurities, such as carbon, nitrogen, and hydroxide-related species. In addition, the columnar shape of the ZrO_2 grains have to be taken into account, which results in grain boundaries which extend straight from one electrode to the other through the thin ZrO_2 film. The main features that are important for the discussion of the electrical properties of the ALD ZrO_2 based thin film RS devices are summarized in the schematic picture on top of Figure 7.1. In such meta-stable, polycrystalline zirconia thin films, grown by ALD, complex defect structures might appear which cannot be handled in some detail. Therefore, a very basic approach starting with the defect chemical description of acceptor-doped nano-crystalline zirconium oxide was proposed. Taking into account the non-equilibrium deposition conditions during ALD process, it might be possible that the N and C impurities may form acceptor-type defects on anion lattice sites [73, 129-130]. Charge compensation of acceptor-type impurities in ZrO_2 occurs via formation of oxygen vacancies and electron holes. It was assumed that in polycrystalline ZrO_2 acceptor-ions segregate towards the grain boundaries in order to

compensate for a donor-type grain boundary core (GB-C) charge which is built from immobile defects [81]. This grain boundary regime can best be described as a double Schottky barrier that is formed from a two space charge layers (SCL) adjacent to a GB-C.

According to the experimental data, the Pt/ZrO_2/Ti/Pt and the Pt/ZrO_2/TiN cells in pristine states were described by good insulating capacitor structures, showing no significant effect of the different thicknesses of the EAE, either 5 nm Ti or 30 nm TiN. Therefore, it might be concluded that the pristine states of both Pt/ZrO_2/(EAE) cells could be described as homogeneous capacitors.

After electroforming the cells into the ON states the situation has completely changed. The Pt/ZrO_2/Ti/Pt cells with the thin EAE switched in UP manner and the ON state conduction had a metallic-type behavior. On the contrary, the Pt/ZrO_2/TiN cells, i.e. thick EAE, exhibited a semiconducting ON-state and a BP switching behavior. The experimental results of the impedance analysis were discussed in detail in Chapter 6. Schematic pictures of the ZrO_2 thin film microstructural defects and the corresponding equivalent networks obtained from the experimental fittings are shown in Figure 7.1.

During the electroforming step a high positive voltage was applied to the top EAE, which generated an increased current flow through the ZrO_2 thin film. Due to a higher intrinsic defect concentration the grain boundaries (GB) may possibly form regions with a higher conductance than the insulating grains which are even considered as depleted due to their small grain size. Therefore, the lateral current distribution under the capacitors pad is perhaps not homogeneous but concentrated at the grain boundaries and especially at sites of highest intrinsic conductivity. If this is the case, the high current density may induce a local heating of the thin film material which enables a considerable migration of oxygen ions from the ZrO_2 film towards the EAE under the applied voltage.

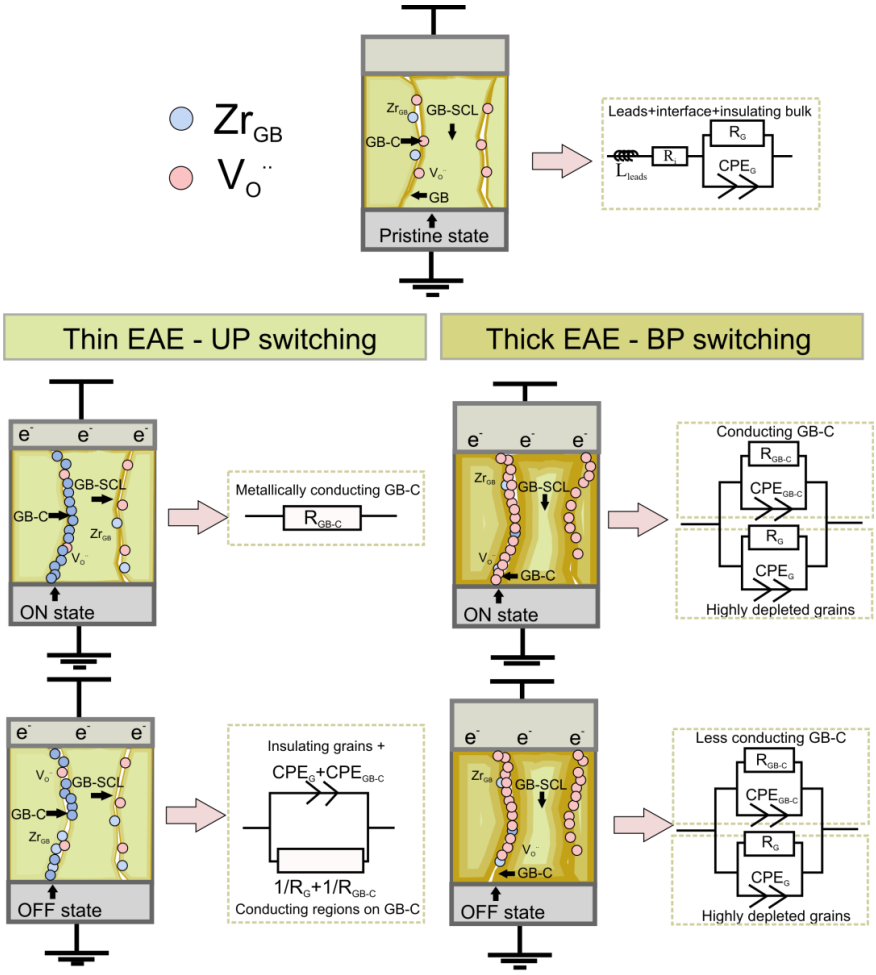

Figure 7.1 Resistive switching mechanism proposed for polycrystalline ALD ZrO_2 thin films, comprising the experimental observations of structural, morphological, and impedance spectroscopy studies. The upper part shows a sketch of switching cell in pristine state together with the equivalent circuit. According to the morphological and structural analysis the polycrystalline ALD grown ZrO_2 films exhibit a meta-stable cubic-tetragonal structure with columnar shaped grains. The lower part shows a model for the unipolar and bipolar RS scenarios which were observed for thin (left side) and thick (right side) electrochemically active electrodes (EAE). The stabilization of the c-t meta-stable phase is considered due to the presence of a certain concentration of defects in the films which in consequence results in defective grain boundaries. The grains are denoted as G, grain boundaries as GB, grain boundary space-charge layers as GB-SCL, and grain boundary cores as GB-C. The respective impedance spectroscopy equivalent schemes are given next to the device sketches.

At this point, the Pt/ZrO_2/Ti/Pt and the Pt/ZrO_2/TiN devices have to be differentiated with respect to the thickness of the EAE layer, starting with the UP type switching mode obtained for Pt/ZrO_2/Ti/Pt cells with a relatively thin EAE of about 5 nm Ti, which is shown on the left side of Figure 7.1. In this case, oxygen ion migration into the Ti electrode may be locally hindered by the limited thickness of the Ti electrode of only 5 nm. Hence, upon electroformation a locally conducting TiO_x ($x < 2$) region might be formed between ZrO_2 and Ti electrode. However, the conducting path along the grain boundary perhaps does not elongate through the whole film, but leaves a partially insulating region of the GB-C. Then the weakest insulating 'plug' will finally break at higher voltages as a result of a 'hard' dielectric breakdown [25, 35]. This might result in a local destruction of the ZrO_2 material and even a reduction of GB-C region to ZrO_x with $x \leq 1$ [126]. The formed ZrO_x -like filament might exhibit a metallic conductivity which was measured experimentally for the ON states of the Pt/ZrO_2/Ti/Pt cells. As a consequence of the high conductivity of the metallic filaments of the Pt/ZrO_2/Ti/Pt cell in the ON-state, a considerable high current was flowing through this filament already at low applied voltage. Therefore, in the RESET process with the same polarity of the applied voltage, the filament might be easily distorted due to thermal melting, leaving behind a highly insulating capacitor, which characterizes the UP RS cell in the OFF state. In subsequent switching cycles, always a new metallic conducting filament might be formed at the actual weakest local point, and during RESET this filament might be broken by Joule heating. This working hypothesis can give a consistent picture for the RS behavior of UP switching devices, which was mainly described by a metallic conductivity in the ON state, a well insulating behavior in the OFF state, a high R_{off} /R_{on} ratio, and high SET voltages (4 to 6 V). In addition, the overall low endurance of the UP switching devices, and the slightly increased endurance that was found for the devices with larger pad areas, could be understood from this model of formation and complete rupture of metallic filaments, for which every filament might be formed and broken only once.

In comparison to UP switching Pt/ZrO_2/Ti/Pt cell, for the case of the Pt/ZrO_2/TiN/Pt devices with a thicker EAE a bipolar type (BP) resistive switching behavior was observed with a lower R_{off}/R_{on} ratio, but also lower switching voltages, and higher endurance. For the BPS cells, both ON and OFF states showed a non-linear *I-V* characteristic with a semiconductor-like temperature dependence of the resistance states and IS which could be simulated by

parallel R|CPE circuits, where only the values of the elements differ for the different states. The phenomena observed for the BP switching devices could also be understood from the empirical model which takes the morphology and defect structure of the ALD ZrO_2 films into account. The BP RS devices underwent an electroforming into the ON state by a positive voltage applied to the EAE top electrode. The mechanism for oxygen ion movement from the ZrO_2 film to the TiN electrode might be comparable to the case of the thinner Ti electrode, but with the difference that the thicker EAE could locally take up a higher amount of oxygen ions. At this point it should be mentioned that the material of the 'TiN' electrode which was deposited by sputtering is in fact most probably a TiN_x, which is characterized by an excess of Ti and therefore its ability to take-up oxygen [127], as compared pure TiN which is seldom. The model for the BP RS devices from polycrystalline ZrO_2 films and thick TiN_x EAE consider that during electroforming the temperature at some local points might be high enough that a considerable oxygen ion drift/diffusion takes place resulting in conducting ZrO_{2-x} filament-like regions, preferable along the GB-C, in contact to a partially oxidized TiN_x electrode layer. Two reasonable scenarios might address the semiconducting ON-state behavior of the BP switching devices. First, the non-linearity of the *I-V* curve might be caused by the semiconducting filament in contact to the Pt and TiN metal electrodes thus forming a local M-S-M cell. Interesting to notice is that a conductive semi-metallic 'Zr_2O_3' phase has recently been proposed by Xue et al. [128] from density functional theory (DFT) calculations. We suppose that this kind of phase could appear on the GB-C of BP switching devices after electroforming. The second scenario would be that the locally reduced ZrO_{2-x} filament does not completely extend down to the Pt bottom electrode, but a thin plug of insulating ZrO_2 material remains forming a local M-I-S-M cell. Consequently, the RESET process initiates a thermally stimulated ion drift in opposite direction that leads to an increase of the insulating gap between the BE and the semiconducting part of the zirconium oxide. The model of thermally assisted oxygen vacancy drift is well established in the understanding of oxide-based resistive switching devices [54]. The suggested empirical model for the polycrystalline ZrO_{2-x} based BP switching devices is shown in the right picture of Figure 7.1.

7.2 Comparison of the empirical model with the experimental results

Finally, the empirical model which was suggested on basis of the measured RS behavior, the TCR of the conducting and insulating states, the morphology and defect structure of the ALD ZrO_2 thin films should be compared with the quantitative results which were obtained from the IS fitting.

While for the UP RS device in ON state, only a metallic like conduction path can be derived from the IS data, the most conspicuous result of the IS analysis was the significantly reduced capacitance of the UP RS device in the OFF state with a value of about one ninth of the capacitance of the device in pristine state (see Table 6-1). The formation and rupture of small metallic filaments cannot explain this decrease in the device's capacity. But the decrease of the capacitance could be understood from the model for the UP RS case, if we assume that the power which is put into the system during the UP SET process might be so large that at weak spots the thermal breakdown could be accompanied by a local deterioration of the device. To clarify this, I performed an additional optical inspection of UP switched Pt/ZrO_2/Ti/Pt cells by means of electron microscopy. One characteristic picture is shown in Figure 7.2 (a). This clearly shows that a significant part of the Pt/ZrO_2/Ti/Pt cell is deteriorated after several cycles of UP switching. This observation could explain the decreased capacitance originating from a decreased pad area (see Eq.(6.4)). This additional result supports the UP switching model for the investigated Pt/ZrO_2/Ti/Pt cells which might be described by formation and complete rupture of metallic filaments, for which every filament might be formed and broken only once. In addition, reference micrographs were obtained from Pt/ZrO_2/TiN cells after numerous cycles of BP switching. Figure 7.2 (b) shows a characteristic picture revealing that no such type of deterioration was observed in any of the BP cells.

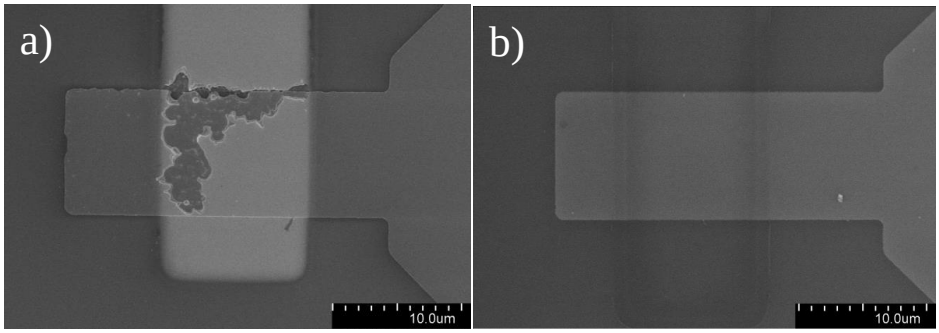

Figure 7.2 (a) SEM micrograph of a significantly deteriorated $Pt/ZrO_{2-x}/Ti/Pt$ cell after electroforming and UP switching. The deterioration was presumably caused by thermal breakdown. (b) SEM micrograph of $Pt/ZrO_{2-x}/TiN$ cell after RS.

For the case of the BP switching $Pt/ZrO_2/TiN$ cells with 30 nm of TiN, for which the switching was considered to be due to a thermally assisted drift of oxygen vacancies along the ZrO_2 grain boundary cores, also interesting results could be derived from the fitting parameters of the respective impedance spectra. The IS data of the RS devices in the ON and OFF states were approximated by a parallel circuit of two R|CPE elements, where one block should describe the contribution of the non-deteriorated 'matrix', and another one the contribution of the grain boundary cores. Applying this potential scenario we could deduce different properties of the conducting filament in the BP switching $Pt/ZrO_2/TiN$ cells in the ON and the OFF state. The $R_1|C_1$ element, attributed to the GB-C, for the BP ON state is described by a resistor of about R_1 = 225 kΩ and a capacitor of C_1 ≈ 60 fF. For the BP OFF state the $R_1|CPE_1$ element which is addressed to the RS behavior was characterized by a resistance of about R_1 = 750 kΩ and a capacitance value of C_1 ≈ 280 fF. These elements of the equivalent circuit might be addressed to the nature of (one or more) filaments in OFF state which are characterized by a reasonable semiconductor-type insulating behavior and a reasonable capacitance which might originate from re-oxidized material closing the filament in form of an insulating plug.

7.2.1 Discussion of the microscopic switching model of the Pt/ZrO_2/(thick EAE) devices

In the following I would like to discuss the proposed "grain boundary model" or GBM (Figure 7.3) of the two parallel (vertical) phases represented by two parallel R|CPE elements further for the case of the BPS device in its OFF state. For this the capacitance values are used which were calculated from the CPE's (Table 6-1) applying Eq. (6.3) earlier. It was found that the IS of the BP OFF state could be fitted by a two parallel R|CPE elements when one element was defined as the pristine matrix (R_2=47.7 TΩ, C_2=1.85 pF). With this the elements of the additional R_1|CPE_1 element could be calculated, as R_1=750 kΩ, C_1=280 fF. On the basis of the micro-structural model of the ZrO_2 films consisting of columnar shaped grains I will now discuss the idea that the contribution of R_1|CPE_1 element might originate from the semi-conducting grain boundary region.

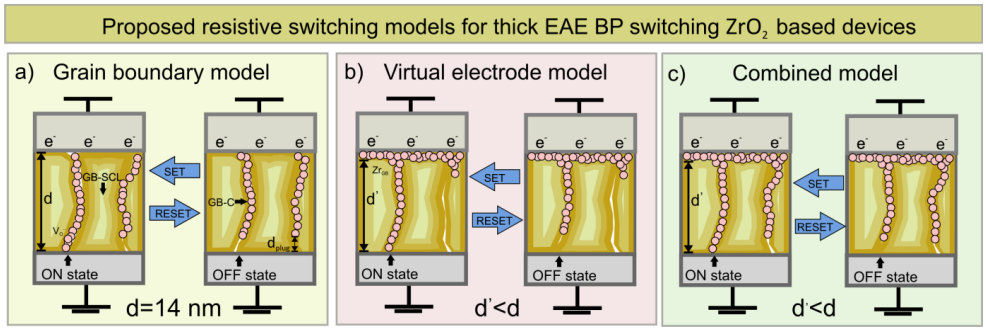

Figure 7.3. The schematic representation of three possible scenarios for the BP RS in the thick EAE Pt/ZrO_2/(EAE) device after electroforming. (a) The grain boundary model, which was discussed in Chapter 7, describes the reduction of the GB-C in ZrO_2 film, and the creation of the conductive filaments along them. This model can be presented as a two (vertical) phase structure, which was described by a two-R|CPE-block scheme in the fitting of the impedance data for the BPS cell. (b) The virtual electrode model implies the formation of the "virtual electrode" underneath the EAE, which reduces the effective thickness of the ZrO_2 layer. (c) The combined model presents a mixture of the models (a) and (b).

The capacitance C_2 (Table 6-1) is defined as a matrix or pristine capacitance C_{Pad} or a total pad capacitance C_{Pad}, which was calculated from the IS data of the pristine state of the device. Accordingly, I will define the calculated C_1 as a capacitance which is related to additional semi-conductive paths that I suppose to be located at the GB-C region and name the corresponding capacitance value $C_{GB\text{-}C}$. Further, from the values of C_2=C_G=C_{Pad}=1.85 pF and C_1= $C_{GB\text{-}C}$=280 fF, the ratio between the capacitance of the grain boundary regime and the capacitance of the pristine state can be defined as:

$$C_{GB-C} = 0.15 \cdot C_{Pad} \qquad (7.1).$$

For a film with columnar microstructure (Figure 4.13 (b)) the ratio of the capacitances relates directly to the ratios of area to thickness of the respective regimes. Therefore, I will first calculate the approximate values for the projected lateral area of the semiconducting grain boundary cores $A_{GB\text{-}C}$. Assuming that the grains are columnar and of cubic shape (Figure 7.4), so that the lateral size of the cubic grains equals the film thickness 14 nm (d), and that the width of the GB-C is around 1 nm ($d_{GB\text{-}C}$), then it is possible to calculate the number of the grains underneath the pad with the size of A_{Pad}=100 µm^2:

$$n = \frac{A_{Pad}}{d^2} \qquad (7.2),$$

and the single grain projected lateral area of the GB-C would be:

$$A_{GB-C} = d^2 - (d - 2 \cdot d_{GB-C})^2 \qquad (7.3).$$

After the substitution of the corresponding values to equation (7.2) and (7.3) the total number of the grains underneath the top electrode of 100 µm^2 is found to be around $n \sim 5 \cdot 10^5$ and the GB-C area is estimated as $A_{GB-C} \sim 52$ nm^2. The total projected GB-C area is calculated as $A^t_{GB-C} = n \cdot A_{GB-C} = 5 \cdot 10^5 \cdot 52 \cdot 10^{-18}\, m^2 = 26$ µm^2.

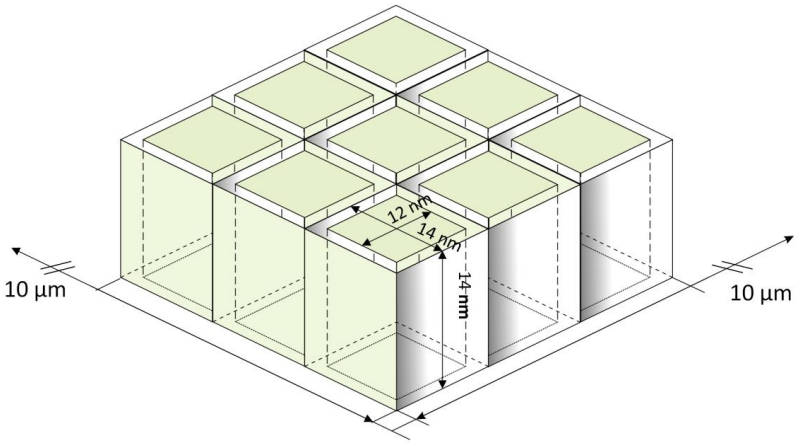

Figure 7.4. Schematic representation of the zirconia cubic grains between the electrodes (not shown). The grains have a facial size of 14 nm (d). The grain boundary width of one grain is taken as 1 nm ($d_{GB\text{-}C}$), hence, the size of the top bulk facet of the grain is 12 nm. The total area of the grains (A_{Pad}) is the area underneath the pad, which is 100 µm^2.

Next, I am going to calculate the ratios of the actual area A_{GB-C}^{actual} of the semi-conducting paths and the thickness of the insulating path d_{plug} that participate in the RS of Pt/ZrO_2/TiN device (Figure 7.3 (b)). For that I assume that in first approximation the electric field distribution across the device, divided between grains and GB-C, remains homogeneous as in case of the pristine state and hence Equation (6.4) for the planar capacitor can be applied for the GB-C. Accordingly, Equation (7.2) can be re-written as:

$$\frac{A_{GB-C}^{actual}}{d_{plug}} = 0.15 \cdot \frac{A_{Pad}}{d} \qquad (7.4),$$

assuming that the dielectric permittivity is the same (ε~28) for the grains and grain boundary cores. $\mathrm{A_{Pad}}$ in the Eq. (7.4) is the device pad area (100 µm^2), d is the film thickness (14 nm), A_{GB-C}^{actual} is the area that takes part in the switching process and is defined as an "area of the semiconducting filaments" or "reduced area", d_{plug} is the distance between the bottom electrode and the ruptured filaments (insulating plug). From the Eq. (7.4) the ratio $\frac{A_{GB-C}^{actual}}{d_{plug}}$ can be now derived:

$$\frac{A_{GB-C}^{actual}}{d_{plug}} = 0.15\frac{100\cdot10^{-12}}{14\cdot10^{-9}}m = 1071\ \mu\text{m} \qquad (7.5).$$

Equation (7.5) is a linear function of the A_{GB-C}^{actual} from d_{plug}. Therefore, if we consider $d_{Plug} \leq d$, it can be solved graphically as shown in Figure 7.5.

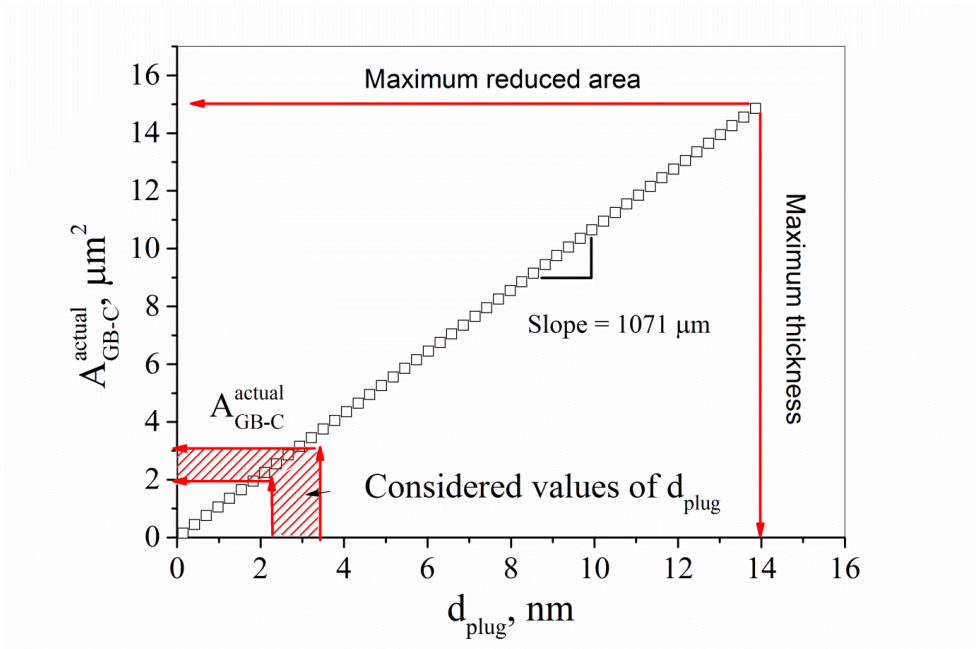

Figure 7.5 Graphical solution of Equation (7.7). The A_{GB-C}^{actual} can be estimated by taking the reasonable length of the insulating plug d_{plug}, which cannot be longer than the film thicknes, which is 14 nm.

From the Figure 7.5 one can see that maximum value of A_{GB-C}^{actual} is even lower than the estimated value of the total projected GB-C area $A_{GB-C}^{t} \approx 26\ \mu m^2$. This shows that most probably not all GB-C's are participating in the electroformation process. Considering the values of the insulating plug length of about 2-3 nm (red area in Figure 7.5), the A_{GB-C}^{actual} would be around 2-3 % of A_{Pad}. Hence, a certain number of conductive paths are formed between the electrodes where each of them might form a switching filament after a SET process. In contrast, the extrapolation of the line in Figure 7.5 shows that it is not possible to propose only one single spot of reduced material that may form a single conducting filament. The area of this filament should not exceed ~25-100 nm^2, the value which is taken

from the theoretical calculation based on self-heating of the filament [132]. Such a small area of $A_{fil} = 25 - 100\ nm^2$ would result in a non-physical value for d_{plug} in order to fit the experimental results (Eq. (7.5)).

Another possibility which might explain the measured increase the capacitance of the BP RS ZrO_2 cell in the OFF state in comparison to the pristine state is a formation of a "virtual electrode" (Figure 7.3 (b)) [16]. This virtual electrode (VE) should consist of a highly oxygen deficient conductive ZrO_x region close to the top EAE. This VE layer would not be directly observable in IS, as it would be regarded as a part of the top electrode. The formation of the virtual electrode would result in a reduction of the "effective" thickness of the insulating oxide layer and hence yield to an increase of the capacitance of the device. If this is the case, then the capacitance obtained from the fitting of the impedance spectra with a one-R|CPE-block scheme must be considered, which I will denote here as C_{OFF}. As it was already mentioned the C_{OFF}, which was found to be 1.88 pF, is higher than the calculated capacitance of the pristine state (C_2=$C_{pristine}$= 1.85 pF). Hence, the increase of the capacitance is:

$$\Delta C = C_{OFF} - C_{pristine} = 0.3\ pF. \qquad (7.6).$$

This defines also the decrease of the effective ZrO_2 layer thickness, which can be then denoted as:

$$d' = d - d_{VE} \qquad (7.7),$$

where d_{VE} is the thickness of the formed virtual electrode. From the Eq. (6.4), if the area of the pad and the virtual electrode as well as dielectric constants are taken as equal in the pristine and OFF states, then we can do the following:

$$C_{OFF} = \varepsilon \cdot \varepsilon_o \cdot \frac{A_{Pad}}{d'} = \left(\varepsilon \cdot \varepsilon_o \cdot \frac{A_{Pad}}{d}\right) \cdot \frac{d}{d'} = C_{pristine} \cdot \frac{d}{d'} \qquad (7.8),$$

and hence from Eq.(7.6) and Eq. (7.8) we obtain:

$$\Delta C = C_{OFF} - C_{pristine} = C_{pristine}\left(\frac{d}{d'} - 1\right) \qquad (7.9).$$

From the last equation one can finally calculate the obtained effective thickness of the oxide layer after forming of the virtual electrode:

$$d' = \frac{d}{\frac{\Delta C}{C_{pristine}} + 1} = 12.04\ nm \qquad (7.10).$$

From this the thickness of the virtual electrode in the OFF state follows to be around 2 nm. In the ON state tiny filaments will form and elongate through the film connecting the BE with the top virtual one, as shown in Figure 7.3 (b). However, the number of conducting filaments will be probably smaller than in case of the GBM.

Both, the GBM and the virtual electrode model (VEM) could only define “extreme” cases of possible switching scenarios. The reality might be probably described by a combined model, presented in Figure 7.3 (c). In this case the virtual electrodes as well as the filaments along the grains might be formed during electroforming. The switching is again performed merely by the local oxidation of the filament near the Pt electrode. In this case a higher number of filaments are formed compared to the VEM.

In addition, I would like to notice that the calculated GB-C capacitance in ON state of the BPS cell, for the one-R|CPE-block scheme was lower (1.65 pF) than in the pristine state (1.85 pF). This can be explained by the increase of the degree of system’s inhomogeneity after SET process, and as a consequence the decrease of the corresponding coefficient α (Eq. (6.3)). Hence, for the comparison of the pristine and ON states, the CPE values have to be considered. Furthermore, the CPE values in ON and OFF states for the BPS cells are practically identical, even though the cells exhibit very different conductivity. This result further supports the filamentary switching model in ZrO_2, because not all the conducting filaments are believed to contact the BE in the ON state.

8. General conclusions

This thesis presents a comprehensive study of the resistive switching phenomena in ZrO_2 thin film based devices. ZrO_2 thin films as well as ZrO_2/TiO_2 bilayers were grown using the atomic layer deposition (ALD) technique, structurally characterized, integrated into resistive switching (RS) devices, and tested for their RS properties. The films' microstructure features, metal-oxide-metal (MOM) device configuration, and stacking sequence in bilayers were considered as the factors influencing the RS performance.

Most of the zirconia films were grown from TEMA-Zr precursor, but also the guan-Zr precursor was tested. For the films grown from TEMA-Zr, the variation of the ALD oxygen sources (O_3 or H_2O) influenced the films' morphology, crystalline structure, and slightly the RS properties. The films' crystalline structure was a mixture of cubic and tetragonal phases. The ozone grown films (OGF) had a preferred orientation on Pt and a cubic shape of the grains. On the contrary, the water grown films (WGF) were randomly oriented on Pt with the grains of all shapes and sizes. The RS devices based on the OGF exhibited a higher yield, i.e. the number of working cells, in comparison to the ones based on WGF.

The MOM device configuration was varied in a sense of the selection of a top electrochemically active electrode (EAE) material and its thickness. The $Pt/ZrO_2/Ti/Pt$ structures exhibited unipolar-type RS when the Ti top electrode (TE) thickness was varied between 0 to 20 nm. A further increase of Ti TE thickness resulted in a gradual change of the switching mode from unipolar (UP) to bipolar (BP) with the yield of the working cells reaching 90% that was the highest among all tested devices, when the 40 nm thick Ti TE was used. The TiN TE was also tested in $Pt/ZrO_2/TiN$ structures, which exhibited stable BP switching with the TiN thickness of 30 nm. The RS characteristics of all BP switching cells exhibited good stability, yield, endurance, and retention. Hence, the BP switching $Pt/ZrO_2/(EAE)$ devices, with zirconia films grown form TEMA-Zr/O_3 and sufficiently thick top EAE, fulfilled RRAM specifications, in contrast to the UP switching cells.

The RS of Pt/ZrO_2/TiN structures, in which the integrated ZrO_2 films were grown from guan-Zr/O_3, also had the BPS-type behaviour, when the 30 nm TiN TE were used. However, in contrast to a good performance of the Pt/(TEMA-Zr) ZrO_2/TiN (30 nm) cells, the devices based on the guan-Zr/O_3 grown films were less stable. The bi-stable RS, i.e. alternating linear and non-linear behaviour of *I-V* curves in the ON state, was found in the guan-Zr/O_3 grown films. Due to the bi-stable ON state behaviour the large variation of R_{off}/R_{on} ratio was observed.

The RS of the ZrO_2/TiO_2 bilayer structures, with the Pt bottom electrodes and Ti/Pt or TiN as top electrodes, depended on the stacking sequence of the oxide layers. While the switching of the Pt/ZrO_2/TiO_2/Ti (5 nm)/Pt devices was unipolar, and thus comparable to Pt/ZrO_2/Ti (5 nm)/Pt cells, the bilayers with the reverse structure, Pt/TiO_2/ZrO_2/Ti (5 nm)/Pt, showed non-switching behaviour, most probably due to the symmetry of the stacking sequence. In contrast, the same structures but with the Ti (40 nm)/Pt (10 nm) TE were all switching bipolar, independent on the stacking sequence.

Temperature dependences (TD) of the ON and OFF resistance states in the Pt/ZrO_2/Ti (5 nm)/Pt and Pt/ZrO_2/TiN (30 nm) devices were studied. For the Pt/ZrO_2/Ti/Pt and Pt/ZrO_2/TiN devices, that were switching UP and BP, respectively, the clear difference in the TD behaviour was identified. The UP cells exhibited metallic-type conduction in the ON state, whereas the BP cells a non-metallic one. In case of the OFF state both devices exhibited semiconductor-type behaviour. Further, this result was utilized in the description of the fundamental differences in the switching mechanism of zirconia depending on the thickness of the top EAE.

Using impedance spectroscopy the electric behaviour of the UP switching (Pt/ZrO_2/Ti/Pt) and BP switching (Pt/ZrO_2/TiN) devices in the pristine, ON, and OFF states was investigated. Both UPS and BPS devices in their pristine state were identical and showed pure capacitor-type impedance. This indicated that before electroforming the ZrO_2 films structure in the Pt/ZrO_2/Ti/Pt and Pt/ZrO_2/TiN devices was not significally affected by the top EAE with different thicknesses thus could be presented as homogeneous capacitors. After electroforming, in the ON and OFF states the impedances of these two devices differed. Accordingly, the UPS cells could be characterized as an insulating capacitor in the OFF state and a resistor in the ON state. The OFF state capacitance of the UPS cells was lower than in

the pristine case, probably due to the deterioration of the top electrode during RS, which changed the total pad area of the cell. On the contrary, the BPS cells had similar complex impedance in both ON and OFF states with slightly differing resistance and capacitance values. Due to the enhancement of the total Q value of the corresponding constant phase element (CPE) in the ON and OFF states (if the fitting was done with one R|CPE block), the impedance data of the BPS cell could be fitted with the two R|CPE block scheme (which is an equivalent to the one R|CPE block scheme), which provided a rear possibility to discern two conductive phases in the device, i.e. an insulating matrix (grains) and reduced grain boundary cores, where the conductive filaments were formed.

Through the accurate analyses of the ZrO_2 films nano-crystalline structure, impurity content, the influence of the top EAE thickness on the RS behavior, R_{on}, R_{off} temperature dependences, and impedance spectroscopy data, I could propose an empirical model for differentiating UP and BP RS mechanisms in ZrO_2 based RS devices. The UP switching of the devices with a thin EAE was addressed to a creation/rupture of zirconium metallic filaments along the grain boundary core (GB-C). The insufficient redox reactions between zirconia and the top EAE, due to the low thickness of the later, might result in a low concentration of injected oxygen vacancies into the ZrO_2 films. Consequently, during the SET process a strong thermal breakdown took place and caused a total reduction of zirconia on the GB-C and/or a melting of the electrodes that was a reason of the metallic filaments formation. The low endurance of the UP switching devices could be explained by the assumption that nearly every filament might have been only formed and broken for one time. On the contrary, the BP switching in the devices with a thick EAE was bonded to a creation/rupture of oxygen vacancies containing filaments, as the total number of oxygen vacancies in the zirconia films was higher, due to the sufficient amount of oxygen exchange reactions on the ZrO_2/(EAE) interface.

To conclude, seven questions, raised at the beginning of this thesis, were fully or partially answered. In the first part of the thesis I presented the studies that investigated the ALD related processes, for example the optimization of the precursor/oxygen source parameters for obtaining suitable films for RS application. An excellent potential of the ALD technique for growing ZrO_2 films for RS application was presented. The usage of the different oxygen sources, precursors, substrates affected the films structure and allowed to optimize

RS parameters. The best ALD parameters in that case were: the deposition temperature of 240 °C and a combination of TEMA-Zr/O_3 precursors. The Pt/ZrO_2/Ti (40 nm)/Pt and Pt/ZrO_2/TiN (30 nm) structures were considered as the optimal RS configuration in case of the single switching layer. Nevertheless, the variation of the films stoichiometry using thermal ALD appeared not to be a feasible task, unless the other ALD types would be tested, e.g. the plasma enhanced ALD.

In the second part of the thesis, the closer investigation of the RS mechanism in the zirconia based devices was done. First, the films nanostructure was considered as an inherent part for the construction of an empirical RS model. The columnar grains of ZrO_2 films were formed as a result of the meta-stable crystallization. The films crystallized into the high temperature phases (cubic-tetragonal) due to a certain concentration of the impurities that originated from the ALD process. The vertical grain boundaries cores served as the places for the formation of the conductive filaments. The switching mode also depended on the thickness of the used EAE in the device configuration that defined the number of the injected oxygen vacancies in the zirconia films. The combination of the structural analysis with measurements of the temperature dependences of the resistance states and the impedance spectroscopic characterization enabled the construction of a micro-structural grain boundary model which could describe the difference in unipolar and bipolar type RS in Pt/ZrO2/(EAE) devices as a function of the thickness of the electrochemically active electrode. Furthermore, the proposed grain boundary model was compared to the virtual electrode model which showed that the combination of these two models is the most reasonable scenario in the description of the BP switching in the thick EAE ZrO_2 based devices.

List of figures

List of tables

Bibliography

[1] R. Waser and M. Aono, “Nanoionics-based resistive switching memories,” *Nature Materials*, vol. 6, pp. 833-840, 2007.

[2] D.-H. Kwon, K. M. Kim, J. H. Jang, J. M. Jeon, M. H. Lee, G. H. Kim, X.-S. Li, G.-S. Park, B. Lee, S. Han, M. Kim, and C. S. Hwang, “Atomic structure of conducting nanofilaments in TiO_2 resistive switching memory,” *Nature Nanotechnology*, vol. 5, pp. 148-153, 2010.

[3] B.J. Choi, S. Choi, K.M. Kim, Y. C. Shin, C. S. Hwang, S. Y. Hwang, S. Cho, S. Park, and S. K. Hong, “Study on the resistive switching time of TiO_2 thin films,” *Applied Physics Letters*, vol. 89, pp. 12906/1-3, 2006.

[4] J. C. Scott and L. D. Bozano, “Nonvolatile Memory Elements Based on Organic Materials,” *Advanced Materials*, vol. 19, pp. 1452-1463, 2007.

[5] K. Tsunoda, Y. Fukuzumi, J. R. Jameson, Z. Wang, P. B. Griffin, and Y. Nishi, “Bipolar resistive switching in polycrystalline TiO_2 films,” *Applied Physics Letters*, vol. 90, pp. 113501/1-3, 2007.

[6] L. Zhang, Z. Chen, J. J. Yang, B. Wysocki, N. McDonald, and Y. Chen, “A compact modeling of TiO_2-TiO_{2-x} memristor,” *Applies Physics Letters*, vol. 102, pp. 153503/1-4, 2013.

[7] B. J. Choi, D. S. Jeong, S. K. Kim, C. Rohde, S. Choi, J. H. Oh, H. J. Kim, C. S. Hwang, K. Szot, R. Waser, B. Reichenberg, and S. Tiedke, “Resistive switching mechanism of TiO_2 thin films grown by atomic-layer deposition,” *Journal of Applied Physics*, vol. 98, pp. 33715/1-10, 2005.

[8] Ch. Walczyk, Ch. Wenger, R. Sohal, M. Lukosius, A. Fox, J. Dabrowski, D. Wolanski, B. Tillack, H.-J. Muessig, and T. Schroeder, “Pulse-induced low power resistive switching

in HfO_2 metal-insulator-metal diodes for nonvolatile memory applications," *Journal of Applied Physics*, vol. 105, pp. 114103, 2009.

[9] T. Sakamoto, K. Lister, N. Banno, T. Hasegawa, K. Terabe, and M. Aono, "Electronic transport in Ta_2O_5 resistive switch," *Applied Physics Letters*, vol. 91, pp. 92110/1-3, 2007.

[10] Y. Li, S. Long, M. Zhang, Q. Liu, L. Shao, S. Zhang, Y. Wang, Q. Zuo, S. Liu, and M. Liu, "Resistive Switching Properties of Au/ZrO_2/Ag Structure for Low-Voltage Nonvolatile Memory Applications," *IEEE Electron Device Letters*, vol. 31, pp. 117-119, 2010.

[11] S. Spiga, A. Lamperti, C. Wiemer, M. Perego, E. Cianci, G. Tallarida, H. L. Lu, M. Alia, F. G. Volpe, and M. Fanciulli, "Resistance switching in amorphous and crystalline binary oxides grown by electron beam evaporation and atomic layer deposition," *Microelectronic Engineering*, vol. 85, pp. 2414-2419, 2008.

[12] D. C. Kim, S. Seo, S. E. Ahn, D.-S. Suh, M. J. Lee, B.-H. Park, and I. K. Yoo, "Electrical observations of filamentary conductions for the resistive memory switching in NiO films," *Applied Physics Letters*, vol. 88, pp. 202102/1-3, 2006.

[13] Y. Watanabe, J. G. Bednorz, A. Bietsch, Gerber-Ch, D. Widmer, A. Beck, and S. J. Wind, "Current-driven insulator-conductor transition and nonvolatile memory in chromium-doped $SrTiO_3$ single crystals," *Applied Physics Letters*, vol. 78, pp. 3738-40, 2001.

[14] C. Y. Lin, C. Y. Wu, C. Y. Wu, C. Hu, and T. Y. Tseng, "Bistable resistive switching in Al_2O_3 memory thin films," *Journal of Electrochemical Society*, vol. 154, pp. G189-92, 2007.

[15] C. Schindler, S. C. P. Thermadam, R. Waser, and M. N. Kozicki, "Bipolar and unipolar resistive switching in Cu-doped SiO_2," *IEEE Transactions Electron Devices*, vol. 54, pp. 2762-2768, 2007.

[16] R. Waser, R. Dittmann, G. Staikov, and K. Szot, "Redox-Based Resistive Switching Memories - Nanoionic Mechanisms, Prospects, and Challenges," *Advanced Materials*, vol. 21, pp. 2632-2663, 2009.

[17] S.-Y. Wang, D.-Y. Lee, T.-Y. Tseng, and C.-Y. Lin, "Effects of Ti top electrode thickness on the resistive switching behaviors of rf-sputtered ZrO_2 memory films," *Applied Physics Letters*, vol. 95, pp. 112904/1-3, 2009.

[18] D. S. Jeong, H. Schroeder, and R. Waser, "Coexistence of bipolar and unipolar resistive switching behaviors in a Pt/TiO_2/Pt stack," *Electrochemical Solid State Letters*, vol. 10, pp. G51-G53, 2007.

[19] X. Sun, G. Li, X. Zhang, L. Ding, and W. Zhang, "Coexistence of the bipolar and unipolar resistive switching behaviors in Au/$SrTiO_3$/Pt cells," *Journal of Physics, D-Applied Physics*, vol. 44, pp. 125404/1-5, 2011.

[20] T. Yanagida, K. Nagashima, K. Oka, M. Kanai, A. Klamchuen, B.H. Park, and T. Kawai, "Scaling Effect on Unipolar and Bipolar Resistive Switching of Metal Oxides," *Scientific reports*, vol. 3, 2013.

[21] I. Kärkkänen, A. Shkabko, M. Heikkilä, J. Niinistö, M. Ritala, M. Leskelä, S. Hoffmann-Eifert, and R. Waser, "Study of atomic layer deposited ZrO_2 and ZrO_2/TiO_2 films for resistive switching application," *Physics Status Solidi A*, DOI: 10.1002/pssa.201330034, 2013.

[22] D. Y. Lee, T. L. Tsai, and T. Y. Tseng, "Unipolar resistive switching behavior in Pt/HfO_2/TiN device with inserting ZrO_2 layer and its 1 diode-1 resistor characteristics," *Applied Physics Letters*, vol. 103, pp. 32905/1-4, 2013.

[23] K. J. Yoon, S. J. Song, J. Y. Seok, J. H. Yoon, G. H. Kim, J. H. Lee, and C. S. Hwang, "Ionic bipolar resistive switching modes determined by the preceding unipolar resistive switching reset behavior in Pt/TiO_2/Pt," *Nanotechnology*, vol. 24, pp. 145201/1-8, 2013.

[24] A. Beck, J. G. Bednorz, C. Gerber, C. Rossel, and D. Widmer, "Reproducible switching effect in thin oxide films for memory applications," *Applied Physics Letters*, vol. 77, pp. 139-41, 2000.

[25] B. Sun, L. Liu, N. Xu, B. Gao, Y. Wang, D. Han, X. Liu, R. Han, and J. Kang, "The effect of the current compliance on the resistive switching behaviors in TiN/ZrO_2/Pt memory device," *Japanese Journal of Applied Physics*, vol. 48, pp. 04C061, 2009.

[26] K. C. Park and S. Basavaiah, "Bistable switching in Zr-ZrO_2-Au junctions," *Journal of Non-Crystalline Solids*, vol. 2, pp. 284-91, 1970.

[27] D. Lee, H. Choi, H. Sim, D. Choi, H. Hwang, M. J. Lee, S. A. Seo, and I. K. Yoo, "Resistance switching of the nonstoichiometric zirconium oxide for nonvolatile memory applications," *IEEE Electron Device Letters*, vol. 26, pp. 719-21, 2005.

[28] C. Y. Lin, C. Y. Wu, C. Y. Wu, T. C. Lee, F. L. Yang, C. Hu, and T. Y. Tseng, "Effect of top electrode material on resistive switching properties of ZrO_2 film memory devices," *IEEE Electron Device Letters*, vol. 28, pp. 366-8, 2007.

[29] X. Wu, P. Zhou, J. Li, L. Y. Chen, H. B. L. Y. Y. Lin, and T. A. Tang, "Reproducible unipolar resistance switching in stoichiometric ZrO_2 films," *Applied Physics Letters*, vol. 90, pp. 183507/1-3, 2007.

[30] C. Y. Lin, C. Y. Wu, C. Y. Wu, T. Y. Tseng, and C. Hu, "Modified resistive switching behavior of ZrO_2 memory films based on the interface layer formed by using Ti top electrode," *Journal Applied Physics*, vol. 102, pp. 94101/1-5, 2007.

[31] C. Y. Lin, C. Y. Wu, C. Y. Wu, C. C. Lin, and T. Y. Tseng, "Memory effect of RF sputtered ZrO_2 thin films," *Thin Solid Films*, vol. 516, pp. 444-8, 2007.

[32] C.-Y. Lin, S.-Y. Wang, D.-Y. Lee, and T.-Y. Tseng, "Electrical properties and fatigue behaviors of ZrO_2 resistive switching thin film," *Journal of Electrochemical Society*, vol. 155, pp. H615-H619, 2008.

[33] D. Y. Lee, S. Y. Wang, and T. Y. Tseng, "Ti-Induced Recovery Phenomenon of Resistive Switching in ZrO_2 Thin Films," *Journal of Electrochemical Society*, vol. 157, pp. G166-G169, 2010.

[34] P. Zhou, H. Shen, J. Li, L. Y. Chen, C. Gao, Y. Lin, and T. A. Tang, "Resistance switching study of stoichiometric ZrO_2 films for non-volatile memory application," *Thin Solid Films*, vol. 518, pp. 5652-5655, 2010.

[35] G. Y. Zhang, D. Y. Lee, I. C. Yao, C. J. Hung, S. Y. Wang, T. Y. Huang, J. W. Wu, and T. Y. Tseng, "Unipolar Resistive Switching in ZrO_2 Thin Films," *Japanese Journal of Applied Physics*, vol. 52, pp. 41101/1-6, 2013.

[36] A. Salauen, H. Grampeix, J. Buckley, C. Mannequin, C. Vallee, P. Gonon, S. Jeannot, C. Gaumer, M. Gros-Jean, and V. Jousseaume, "Investigation of HfO_2 and ZrO_2 for Resistive Random Access Memory applications," *Thin Solid Films*, vol. 525, pp. 20-27, 2012.

[37] J.Kim, K. Lee, Y. Kim, H. Na, D.-H. Ko, and H.Sohn, "Effect of thermal annealing on resistance switching characteristics of $Pt/ZrO_2/TiN$ stacks," *Materials Chemistry and Physics*, vol. 142, pp. 608-613, 2013.

[38] Q. Liu, W. Guan, S. Long, M. Liu, S. Zhang, Q. Wang, and J. Chen, "Resistance switching of Au-implanted-ZrO_2 film for nonvolatile memory application," *Journal of Applied Physics*, vol. 104, pp. 114514/1-5, 2008.

[39] W. Guan, S. Long, R. Jia, and M. Liu, "Nonvolatile resistive switching memory utilizing gold nanocrystals embedded in zirconium oxide," *Applied Physics Letters*, vol. 91, pp. 62111/1-3, 2007.

[40] S. Y. Wang, D. Y. Lee, T. Y. Huang, J. W. Wu, and T. Y. Tseng, "Controllable oxygen vacancies to enhance resistive switching performance in a ZrO_2-based RRAM with embedded Mo layer," *Nanotechnology*, vol. 21, pp. 495201/1-6, 2010.

[41] M. Liu, Z. Abid, W. Wang, X. He, Q. Liu, and W. Guan, "Multilevel resistive switching with ionic and metallic filaments," *Applied Physics Letters*, vol. 94, pp. 233106/ 1-3, 2009.

[42] M. C. Wu, T. H. Wu, and T. Y. Tseng, "Robust unipolar resistive switching of Co nano-dots embedded ZrO_2 thin film memories and their switching mechanism," *Journal of Applied Physics*, vol. 111, pp. 14505/1-6, 2012.

[43] S. Bing, L. L. Feng, H. D. Dong, W. Yi, L. X. Yan, H. R. Qi, and K. J. Feng, "Improved resistive switching characteristics of Ag-doped ZrO_2 films fabricated by sol-gel process," *Chinese Physics Letters*, vol. 25, pp. 2187-2189, 2008.

[44] S. H. Chang, S. B. Lee, D. Y. Jeon, S. J. Park, G. T. Kim, S. M. Yang, S. C. Chae, H. K. Yoo, B. S. Kang, M. Lee, and T. W. Noh, "Oxide Double-Layer Nanocrossbar for Ultrahigh-Density Bipolar Resistive Memory," *Advanced Materials*, vol. 23, pp. 4063-4067, 2011.

[45] J. Lee, J. Shin, D. Lee, W. Lee, S. Jung, M. Jo, J. Park, K. Biju, S. Kim, S. Park, and H. Hwang, "Diode-less nano-scale ZrO_x/HfO_x RRAM device with excellent switching uniformity and reliability for high-density cross-point memory applications," *IEDM Technical Digest*, DOI: 10.1109/IEDM.2010.5703393, pp. 451-453, 2010.

[46] D. Jeong, R. Thomas, R. Katiyar, J. Scott, H. Kohlstedt, A. Petraru, and C. Hwang, "Emerging memories: Resistive switching mechanisms and current status," *Reports on Progress in Physics*, vol. 75, pp. 076502/1-32, 2012.

[47] R. Münstermann, T. Menke, R. Dittmann, and R. Waser, "Coexistence of Filamentary and Homogeneous Resistive Switching in Fe-doped $SrTiO_3$ Thin-Film Memristive Devices," *Advanced Materials*, vol. 22, pp. 4819, 2010.

[48] E. Linn, R. Rosezin, C. Kügeler, and R. Waser, "Complementary Resistive Switches for Passive Nanocrossbar Memories," *Nature Materials*, vol. 9, pp. 403-406, 2010.

[49] F. Nardi, S. Balatti, S. Larentis, and D. Ielmini, “Complementary switching in metal oxides: toward diode-less crossbar RRAM’s,” *2011 IEEE International Electron Devices Meeting - IEDM '11*, pp. 31.1.1 - 31.1.4, 2011.

[50] D. S. Jeong, H. Schroeder, and R. Waser, “Abnormal bipolar-like resistance change behavior induced by symmetric electroforming in Pt/TiO_2/Pt resistive switching cells,” *Nanotechnology*, vol. 20, pp. 375201, 2009.

[51] K. M. Kim, G. H. Kim, S. J. Song, J. Y. Seok, M. H. Lee, J. H. Yoon, and C. S. Hwang, “Electrically configurable electroforming and bipolar resistive switching in Pt/TiO_2/Pt structures,” *Nanotechnology*, vol. 21, pp. 305203, 2010.

[52] H.-S. P. Wong, H.-Y. Lee, S. Yu, Y.-S. Chen, Y. Wu, P.-S. Chen, B. Lee, F. T. Chen, and M.-J. Tsai, “Metal–Oxide RRAM,” *Proceedings of the IEEE*, vol. 100, pp. 1951-1970, 2012.

[53] K. Szot, M. Rogala, W. Speier, Z. Klusek, A. Besmehn, and R. Waser, “TiO_2 - a prototypical memristive material,” *Nanotechnology*, vol. 22, pp. 254001/1-21, 2011.

[54] R. Waser (Ed.), “Nanoelectronics and Information Technology (3rd edition),” *Wiley-VCH*, 2012.

[55] I. Valov, R. Waser, J. R. Jameson, and M. N. Kozicki, “Electrochemical metallization memories-fundamentals, applications, prospects,” *Nanotechnology*, vol. 22, pp. 254003/1-22, 2011.

[56] R. Rosezin, “Stacked device structures for resistive memory and logic,” *RWTH Aachen*, *Dissertation*, 2012.

[57] C. Hermes, R. Bruchhaus, and R. Waser, “Forming-free TiO_2 based resistive switching devices on CMOS compatible W-plugs,” *IEEE Electron Device Letters*, vol. 32, pp. 1588 - 1590, 2011.

[58] C. Volpato, L. Garbelotto, M. Fredel, and F. Bondioli, “Application of Zirconia in Dentistry: Biological, Mechanical and Optical Considerations Advances in Ceramics - Electric and Magnetic Ceramics”, *Bioceramics, Ceramics and Environment*, 2011.

[59] N. Minh, “Ceramic Fuel-Cells,” *Journal of American Ceramic Society*, vol. 76, pp. 563-588, 1993.

[60] The interactive Ellingham diagram http://www.doitpoms.ac.uk/tlplib/ellingham_diagrams/interactive.php, *University of Oxford*, 2013.

[61] E. H. Kisi, C. J. Howard, and R. J. Hill, “Crystal-Structure of Orthorhombic Zirconia in Partially Stabilized Zirconia,” *Journal of American Ceramic Society*, vol. 72, pp. 1757-1760, 1989.

[62] B. Kralik, E. Chang, and S. Louie, “Structural properties and quasiparticle band structure of zirconia,” *Physical Review B*, vol. 57, pp. 7027-7036, 1998.

[63] M. C. Munoz, S. Gallego, J. I. Beltran, and J. Cerda, “Adhesion at metal-ZrO_2 interfaces,” *Surface Science Reports*, vol. 61, pp. 303-344, 2006.

[64] J. H. Kim, V. A. Ignatova, J. Heitmann, and L. Oberbeck, “Deposition temperature effect on electrical properties and interface of high-k ZrO_2 capacitor,” *Journal of Physics, D Applied Physics*, vol. 41, pp. 172005/1-6, 2008.

[65] X. Zhao and D. Vanderbilt, “Phonons and lattice dielectric properties of zirconia,” *Physical Review, B: Condensed Matter*, vol. 65, pp. 75105/1-10, 2002.

[66] R. Hannink, P. Kelly, and B. Muddle, “Transformation toughening in zirconia-containing ceramics,” *Journal of American Ceramic Society*, vol. 83, pp. 461-487, 2000.

[67] P. Aldebert and J. Traverse, “Structure and Ionic Mobility of Zirconia at High-Temperature,” *Journal of American Ceramic Society*, vol. 68, pp. 34-40, 1985.

[68] F. Kern and R. Gadow, “Properties of Injection Moulded Alumina-Toughened Zirconia,” *Journal of Ceramic Science and Technology*, vol. 2, pp. 47-54, 2010.

[69] T. Sheu, T. Tien, and I. Chen, “Cubic-to-Tetragonal (T') Transformation in Zirconia-Containing Systems,” *Journal of American Ceramic Society*, vol. 75, pp. 1108-1116, 1992.

[70] S. K. Kim and C. S. Hwang, “Atomic layer deposition of ZrO_2 thin films with high dielectric constant on TiN substrates,” *Electrochemical and Solid State Letters*, vol. 11, pp. G9-G11, 2008.

[71] E. H. Kisi and C. J. Howard, “Crystal structures of zirconia phases and their inter-relation,” *Key Engineering Materials*, vol.153-154, pp. 1-36, 1998.

[72] M. Amberg and J. Gunter, “Metastable cubic and tetragonal zirconium dioxide, prepared by thermal oxidation of the dichalcogenides,” *Solid State Ionics*, vol. 84, pp. 313-321, 1996.

[73] I. Valov, V. Rührup, R. Klein, T. Rödel, A. Stork, S. Berendts, M. Dogan, H. Wiemhöfer, M. Lerch, and J. Janek, “Ionic and electronic conductivity of nitrogen-doped YSZ single crystals,” *Solid State Ionics*, vol. 180, pp. 1463-1470, 2009.

[74] G. Wang, G. Luo, Y. L. Soo, R. F. Sabirianov, H. J. Lin, W. N. Mei, F. Namavar, and C. L. Cheung, "Phase stabilization in nitrogen-implanted nanocrystalline cubic zirconia," *Physical Chemistry Chemical Physics*, vol. 13, pp. 19517-19525, 2011.

[75] R. C. Garvie, "Occurnece of Metastable Tetragonal Zirconia as a Crystallite Size Effect," *Journal of Physical Chemistry*, vol. 69, pp. 1238, 1965.

[76] S. Fabris, A. Paxton, and M. Finnis, "A stabilization mechanism of zirconia based on oxygen vacancies only," *Acta Materialia*, vol. 50, pp. 5171-5178, 2002.

[77] S. Shukla and S. Seal, "Mechanisms of room temperature metastable tetragonal phase stabilisation in zirconia," *International Materials Review*, vol. 50, pp. 45-64, 2005.

[78] F. Namavar, G. Wang, C. L. Cheung, R. F. Sabirianov, X. C. Zeng, W. N. Mei, J. Bai, J. R. Brewer, H. Haider, and K. L. Garvin, "Thermal stability of nanostructurally stabilized zirconium oxide," *Nanotechnology*, vol. 18, pp. 415702/1-6, 2007.

[79] M. Tsuchiya, A. M. Minor, and S. Ramanathan, "Size-dependent phase transformations in nanoscale pure and Y-doped zirconia thin films," *Philosophical Magazine*, vol. 87, pp. 5673-5684, 2007.

[80] J. Nowotny, M. Rekas, and T. Bak, "Defect Chemistry and Defect-Dependant Properties of Undoped and Stabilized Zirconia. Bulk vs Interface," *Key Engineering Materials*, vol. 153-154, pp. 211, 1998.

[81] X. Guo and R. Waser, "Electrical properties of the grain boundaries of oxygen ion conductors: Acceptor-doped zirconia and ceria," *Progress in Materials Science*, vol. 51, pp. 151-210, 2006.

[82] X. Guo, "Can we achieve significantly higher ionic conductivity in nanostructured zirconia?," *Scripta Materialia*, vol. 65, pp. 96-101, 2011.

[83] M. V. F. Schlupp, B. Scherrer, H. Ma, J. G. Grolig, J. Martynczuk, M. Prestat, and L. J. Gauckler, "Influence of microstructure on the cross-plane oxygen ion conductivity of yttria stabilized zirconia thin films," *Physica Status Solidi, A-Applied Materials*, vol. 209, pp. 1414-1422, 2012.

[84] M. Ritala and J. Niinistö, "Industrial Applications of Atomic Layer Deposition," *ECS Transactions*, vol. 25, pp. 641-652, 2009.

[85] T. Watanabe, S. Hoffmann-Eifert, C. S. Hwang, and R. Waser, "Growth behavior of atomic-layer-deposited $Pb(Zr,Ti)O_x$ thin films on planar substrate and three-

dimensional hole structures," *Journal of Electrochemical Society*, vol. 155, pp. D715-22, 2008.

[86] E. Farm, M. Kemell, E. Santala, M. Ritala, and M. Leskela, "Selective-Area Atomic Layer Deposition Using Poly(vinyl pyrrolidone) as a Passivation Layer," *Journal of Electrochemical Society*, vol. 157, pp. K10-K14, 2010.

[87] R. Puurunen, "Surface chemistry of atomic layer deposition: A case study for the trimethylaluminum/water process," *Journal of Applied Physics*, vol. 97, pp. 121301/1-52, 2005.

[88] T. Blanquart, "Atomic Layer Deposition of Groups 4 and 5 Transition Metal Oxide Thin Films: Focus on Heteroleptic Precursors", *Dissertation*, University of Helsinki, 2013.

[89] W. Weinreich, T. Tauchnitz, P. Polakowski, M. Drescher, S. Riedel, J. Sundqvist, K. Seidel, M. Shirazi, S. D. Elliott, S. Ohsiek, E. Erben, and B. Trui, "TEMAZ/O_3 atomic layer deposition process with doubled growth rate and optimized interface properties in metal-insulator-metal capacitors," *Journal of Vacuum Science and Technology A*, vol. 31, pp. 1A123, 2013.

[90] B. Lee, K. J. Choi, A. Hande, M. J. Kim, R. M. Wallace, J. Kim, Y. Senzaki, D. Shenai, H. Li, M. Rousseau, and J. Suydam, "A novel thermally-stable zirconium amidinate ALD precursor for ZrO_2 thin films," *Microelectronic Engineering*, 2009, pp. 272-276.

[91] J. Niinisto, K. Kukli, M. Heikkila, M. Ritala, and M. Leskela, "Atomic Layer Deposition of High-k Oxides of the Group 4 Metals for Memory Applications," *Advanced Engineering Materials*, vol. 11, pp. 223-234, 2009.

[92] J. Niinisto, K. Kukli, M. Kariniemi, M. Ritala, M. Leskela, N. Blasco, A. Pinchart, C. Lachaud, N. Laaroussi, Z. Wang, and C. Dussarrat, "Novel mixed alkylamido-cyclopentadienyl precursors for ALD of ZrO_2 thin films," *Journal of Materials Chemistry*, vol. 18, pp. 5243-5247, 2008.

[93] K. Kukli, M. Ritala, and M. Lesklelä, "Impact of atomic layer deposition chemistry to the quality of high-permittivity metal oxide thin solid films," *New Materials and Processes for Incoming Semiconductors Technologies*, pp. 1-40, 2006.

[94] S. K. Kim, S. Hoffmann-Eifert, M. Reiners, and R. Waser, "Relation Between Enhancement in Growth and Thickness-Dependent Crystallization in ALD TiO_2 Thin Films," *Journal of Electrochemical Society*, vol. 158, pp. D6-D9, 2011.

[95] R. P. Chaukulkar and S. Agarwal, “Atomic layer deposition of titanium dioxide using titanium tetrachloride and titanium tetraisopropoxide as precursors,” *Journal of Vacuum Science and Technology A*, vol. 31, pp. 31509/1-5, 2013.

[96] A. Lamperti, L. Lamagna, G. Congedo, and S. Spiga, “Cubic/Tetragonal Phase Stabilization in High-kappa ZrO_2 Thin Films Grown Using O_3 - Based Atomic Layer Deposition,” *Journal of Electrochemical Society*, vol. 158, pp. G221-G226, 2011.

[97] Katz G. “X-Ray Diffraction Powder Pattern of Metastable Cubic ZrO_2,” *Journal of American Ceramic Society*, vol. 54, pp. 531, 1971.

[98] B. Bondars, G.Heidemane, J.Grabis, K. Laschke, H. Boysen, J. Schneider, F. Frey “Powder diffraction investigations of plasma sprayed zirconia,” *Journal of Material Science*, vol. 30, pp. 1621-1625, 1995.

[99] T. Sheu, “Anisotropic Thermal-Expansion of Tetragonal Zirconia Polycrystals,” *Journal of American Ceramic Society*, vol. 76, pp. 1772-1776, 1993.

[100] J. Boem, “Über das Verglimmen einiger Metalloxyde,” *Zeitschrift für anorganische und allgemeine Chemie*, vol. 149, pp. 217-222, 1925.

[101] T. Blanquart, J. Niinistö, N. Aslam, M. Banerjee, Y. Tomczak, M. Gavagnin, V. Longo, E. Puukilainen, H.D. Wanzenboeck, W.M.M. Kessels, A. Devi, S. Hoffmann-Eifert, M. Ritala, and M. Leskelä, “$[Zr(NEtMe)_2(guan\text{-}NEtMe_2)_2]$ as a novel ALD precursor: ZrO_2 film growth and mechanistic studies,” *Chemical Materials*, vol. 25 (15), pp. 3088–3095, 2013.

[102] A. V. Naumkin, A. Kraut-Vass, S. W. Gaarenstroom, and C. J. Powell, “NIST X-ray Photoelectron Spectroscopy Database. NIST Standard Reference Database 20,” 2011.

[103] D. Majumdar and D. Chatterjee, “X-ray photoelectron spectroscopic studies on yttria, zirconia and yttria-stabilized zirconia,” *Journal of Applied Physics*, vol. 70, pp. 988-992, 1991.

[104] D. Ni, Y. Lou, P. Christofides, L. Sha, S. Lao, and J. Chang, “Real-time carbon content control for PECVD ZrO_2 thin-film growth,” *IEEE Transactions Semiconductor Manufacturing*, vol. 17, pp. 221-230, 2004.

[105] J. D. Baniecki, M. Ishii, K. Kurihara, K. Yamanaka, T. Yano, K. Shinozaki, T. Imada, K. Nozaki, and N. Kin, “Photoemission and quantum chemical study of $SrTiO_3$(001) surfaces and their interaction with CO_2,” *Physical Review B: Condensed Matter*, vol. 78, pp. 195415/1-12, 2008.

[106] J. Park, J. K. Heo, and Y. C. Kang, “The Properties of RF Sputtered Zirconium Oxide Thin Films at Different Plasma Gas Ratio,” *Bulletin Korean Chemical Society*, vol. 31, pp. 397-400, 2010.

[107] I. Valov, B. Luerssen, E. Mutoro, L. Gregoratti, R. A. De Souza, T. Bredow, S. Günther, A. Barinov, P. Dudin, M. Martin, and J. Janek, “Electrochemical activation of molecular nitrogen at the Ir/YSZ interface,” *Physical Chemistry Chemical Physics*, vol. 13, pp. 3394-3410, 2011.

[108] M. Lanza, G. Bersuker, M. Porti, E. Miranda, M. Nafria, and X. Aymerich, “Resistive switching in hafnium dioxide layers: Local phenomenon at grain boundaries,” *Applied Physics Letters*, vol. 101, pp. 193502 - 193502-5, 2012.

[109] G. D. Wilk, R. M. Wallace, and J. M. Anthony, “High-kappa gate dielectrics: Current status and materials properties considerations,” *Journal of Applied Physics*, vol. 89, pp. 5243-5275, 2001.

[110] R. B. Belser and W. H. Hicklin, “Temperature Coefficient of Resistance of Metallic Films in the Temperature Range 25-Degrees-C to 600-Degrees-C,” *Journal of Applied Physics*, vol. 30, pp. 313-322, 1959.

[111] J.K. Lee, S. Jung, J. Park, S. W. Chung, J. S. Roh, S. J. Hong, I. H. Cho, H. I. Kwon, C. H. Park, B. G. Park, and J. H. Lee, “Accurate analysis of conduction and resistive-switching mechanisms in double-layered resistive-switching memory devices,” *Applied Physics Letters*, vol. 101, pp. 103506-10350, 2012.

[112] Y. Zhu, M. Li, Z. Hu, H. Zhou, X. Liu, and X. Fang, “Fabrication and mechanism of high performance bipolar resistive switching device based on $SrTiO_3$/NiO stacked heterostructure,” *Microelectronic Engineering*, vol. 104, pp. 85-89, 2013.

[113] R. Waser, S. Menzel, and R. Bruchhaus, “Nanoelectronics and Information Technology (3rd edition)”, *Wiley-VCH*, 2012.

[114] J. Lee, E. M. Bourim, W. Lee, J. Park, M. Jo, S. Jung, J. Shin, and H. Hwang, “Effect of ZrO_x/HfO_x bilayer structure on switching uniformity and reliability in nonvolatile memory applications,” *Applied Physics Letters*, vol. 97, pp. 172105, 2010.

[115] T. Menke, P. Meuffels, R. Dittmann, K. Szot, and R. Waser, “Separation of bulk and interface contributions to electroforming and resistive switching behavior of epitaxial Fe-doped $SrTiO_3$,” *Journal of Applied Physics*, vol. 105, pp. 066104, 2009.

[116] X. L. Jiang, Y. G. Zhao, Y. S. Chen, D. Li, Y. X. Luo, D. Y. Zhao, Z. Sun, J. R. Sun, and H. W. Zhao, "Characteristics of different types of filaments in resistive switching memories investigated by complex impedance spectroscopy," *Applied Physics Letters*, vol. 102, pp. 253507/1-5, 2013.

[117] D. S. Jeong, H. Schroeder, and R. Waser, "Impedance spectroscopy of TiO_2 thin films showing resistive switching," *Applied Physics Letters*, vol. 89, pp. 2909/1-3, 2006.

[118] M. H. Lee, K. M. Kim, G. H. Kim, J. Y. Seok, S. J. Song, J. H. Yoon, and C. S. Hwang, "Study on the electrical conduction mechanism of bipolar resistive switching TiO_2 thin films using impedance spectroscopy," *Applied Physics Letters*, vol. 96, pp. 152909/1-3, 2010.

[119] Y. Xia, Z. Liu, Y. Wang, L. Shi, L. Chen, J.Yin, and X. Meng, "Conduction behavior change responsible for the resistive switching as investigated by complex impedance spectroscopy," *Applied Physics Letters*, vol. 91, pp. 102904/1-3, 2007.

[120] M. R. S. Abouzari, F. Berkemeier, G. Schmitz, and D. Wilmer, "On the physical interpretation of constant phase elements," *Solid State Ionics*, vol. 180, pp. 922-927, 2009.

[121] C. H. Hsu and F. Mansfeld, "Concerning the conversion of the constant phase element parameter Y0 into a capacitance," *Corossion*, vol. 57, pp. 747, 2001.

[122] M. Orazem and B. Tribollet, "Electrochemical impedance spectroscopy," *A. John Wiley & Sons, Inc. Publication*, 2008.

[123] V.F. Lvovich, "Impedance Spectroscopy," *A. John Wiley & Sons, Inc. Publication*, 2012.

[124] T. V. Kundozerova, A. M. Grishin, G. B. Stefanovich, and A. A. Velichko, "Anodic Nb_2O_5 Nonvolatile RRAM," *IEEE Transactions, Electron Devices*, vol. 59, pp. 1144-1148, 2012.

[125] G. Bersuker, J. Yum, L. Vandelli, A. Padovani, L. Larcher, V. Iglesias, M. Porti, M. Nafria, K. McKenna, A. Shluger, P. Kirsch, and R. Jammy, "Grain boundary-driven leakage path formation in HfO2 dielectrics," Solid-State Electronics, vol. 65-66, pp. 146-150, 2011.

[126] X. Guo and Y. Ding, "Grain Boundary Space Charge Effect in Zirconia Experimental Evidence," *Journal of Electrochemical Society*, vol. 151, pp. J1-J7, 2004.

[127] M. Fujimoto, H. Koyama, M. Konagai, Y. Hosoi, K. Ishihara, S. Ohnishi, and N. Awaya, "TiO_2 anatase nanolayer on TiN thin film exhibiting high-speed bipolar resistive switching," Applied Physics Letters, vol. 89, pp. 223509/1-3, 2006.

[128] K.-H. Xue, P. Blaise, L. R. Fonseca, and Y. Nishi, “Prediction of Semimetallic Tetragonal Hf_2O_2 and Zr_2O_3 from First Principles,” Physical Review Letters, vol. 110, pp. 065502 - 06550, 2013.

[129] J. J. Yang, N. P. Kobayashi, J. P. Strachan, M. Zhang, D. A. A. Ohlberg, M. D. Pickett, Z. Li, G. Medeiros-Ribeiro, and R. S. Williams, “Dopant Control by Atomic Layer Deposition in Oxide Films for Memristive Switches,” *Chemistry of Materials*, vol. 23, pp. 123-125, 2011.

[130] M. Kilo, M. Taylor, C. Argirusis, G. Borchardt, M. Lerch, O. Kaitasov, and B. Lesage, “Nitrogen diffusion in nitrogen-doped yttria stabilised zirconia,” *Physical Chemistry Chemical Physics*, vol. 6, pp. 3645-3649, 2004.

[131] S. Logothetidis and A. Barborica, “In-situ and real time room temperature oxidation studies of fcc TiN thin films,” *Microelectronic Engineering*, vol. 33, pp. 309-316, 1997.

[132] S. Menzel, M. Waters, A. Marchewka, U. Böttger, R. Dittmann, and R. Waser, “Origin of the Ultra-nonlinear Switching Kinetics in Oxide-Based Resistive Switches,” *Advanced Functional Materials*, vol. 21, pp. 4487-4492, 2011.

[133] F. Nardi, S. Balatti, S. Larentis, D. C. Gilmer, and D. Ielmini, “Complementary Switching in Oxide-Based Bipolar Resistive-Switching Random Memory,” IEEE Transitions on Electron Devices, vol. 60, pp. 70-77, 2013.

[134] C. Nauenheim, C. Kuegeler, A. Ruediger, and R. Waser, “Investigation of the electroforming process in resistively switching TiO2 nanocrosspoint junctions,” Applied Physics Letters, vol. 96, pp. 122902, 2010.

[135] P. LI, I. Chen, and J. Pennerhahn, “X-ray-absorption studies of zirconia polymorphs. 1. Characteristic local structures,” Physical Review B, vol. 48, pp. 10063-10073, 1993.

Band / Volume 23
Thermal Diffusion in binary Surfactant Systems and Microemulsions
B. Arlt (2012), 159, xlvi pp
ISBN: 978-3-89336-819-8

Band / Volume 24
Ultrathin Gold Nanowires - Chemistry, Electrical Characterization and Application to Sense Cellular Biology
A. Kisner (2012), 176 pp
ISBN: 978-3-89336-824-2

Band / Volume 25
Interaction between Redox-Based Resistive Switching Mechanisms
C. R. Hermes (2012), iii, 134 pp
ISBN: 978-3-89336-838-9

Band / Volume 26
Supported lipid bilayer as a biomimetic platform for neuronal cell culture
D. Afanasenkau (2013), xiv, 132 pp
ISBN: 978-3-89336-863-1

Band / Volume 27
15th European Workshop on Metalorganic Vapour Phase Epitaxy (EWMOVPE XV) June 2-5, 2013, Aachen, Germany
A. Winden (Chair) (2013)
ISBN: 978-3-89336-870-9

Band / Volume 28
Characterization, integration and reliability of HfO_2 and $LaLuO_3$ high-κ/metal gate stacks for CMOS applications
A. Nichau (2013), xi, 177 pp
ISBN: 978-3-89336-898-3

Band / Volume 29
The role of defects at functional interfaces between polar and non-polar perovskite oxides
F. Gunkel (2013), X, 162 pp
ISBN: 978-3-89336-902-7

Band / Volume 30
Parallelisation potential of image segmentation in hierarchical island structures on hardware-accelerated platforms in real-time applications
S. Suslov (2013), xiv, 211 pp
ISBN: 978-3-89336-914-0

Schriften des Forschungszentrums Jülich
Reihe Information

Band / Volume 31
Carrier mobility in advanced channel materials using alternative gate dielectrics
E. Durğun Özben (2014), 111 pp
ISBN: 978-3-89336-941-6

Band / Volume 32
Electrical characterization of manganite and titanate heterostructures
A. Herpers (2014), ix, 165 pp
ISBN: 978-3-89336-948-5

Band / Volume 33
Oxygen transport in thin oxide films at high field strength
D. Weber (2014), XII, 115 pp
ISBN: 978-3-89336-950-8

Band / Volume 34
Structure, electronic properties, and interactions of defects in epitaxial GaN layers
P. H. Weidlich (2014), 139 pp
ISBN: 978-3-89336-951-5

Band / Volume 35
Defect Engineering of $SrTiO_3$ thin films for resistive switching applications
S. Wicklein (2014), xi, 144 pp
ISBN: 978-3-89336-963-8

Band / Volume 36
Integration and Characterization of Atomic Layer Deposited TiO_2 Thin Films for Resistive Switching Applications
M. Reiners (2014), xiv, 166 pp
ISBN: 978-3-89336-970-6

Band / Volume 37
Resistive switching in ZrO_2 based metal-oxide-metal structures
I. Kärkkänen (2014), xviii, 125 pp
ISBN: 978-3-89336-971-3

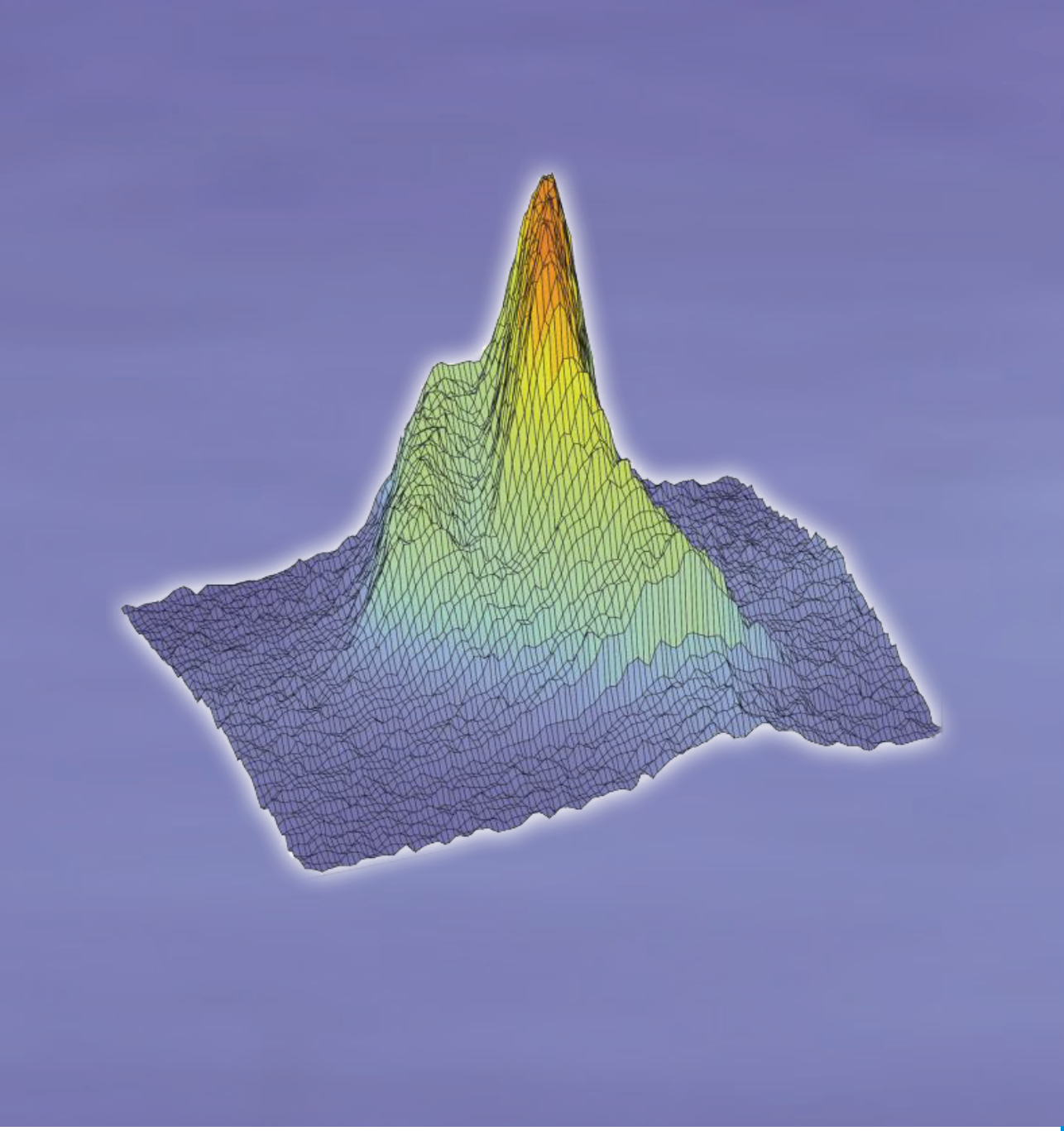

Information / Information
Band / Volume 37
ISBN 978-3-89336-971-3

JÜLICH
FORSCHUNGSZENTRUM